Charles University in Prague

Faculty of Mathematics and Physics

DOCTORAL THESIS

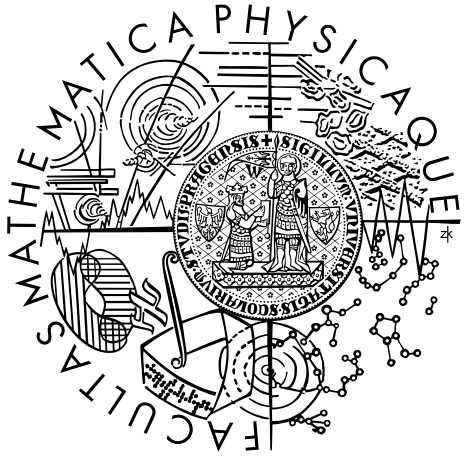

Mykola Telychko

Studying possibilities of graphene functionalization using AFM and STM techniques

Department of Surface and Plasma Science

Supervisor of the doctoral thesis: Ing. Pavel Jelínek, Ph.D.

Study programme: Physics

Specialization: Surface and Interface Physics

Prague 2016

Acknowledgements

First of all, I would like to thank my supervisor Dr. Pavel Jelínek for giving me an opportunity to work in "Nanosurf Lab" and his guidance during my PhD study. I really appreciate his support, friendly attitude and willingness to help me in all issues related to my work and beyond.

Also I want express a great gratitude to my dear friend and colleague Dr. Martin Švec for teaching me all basics of the experimental surface science. A lot of complications and problems I encountered during my PhD study were solved only thanks to his wise advices.

I'm grateful to all my colleagues from the "Nanosurf Lab" Jesus Lopez Roso, Oleksandr Stetsovych, Jan Berger, Bruno de la Torre, Taras Chutora for their help with experiments. It was a great pleasure for me to work with all of them. I'm also grateful to theoreticians Dr. Pingo Mutombo, Mgr. Prokop Hapala, Dr. Martin Ondráček, Mgr. Ondřej Krejčí who performed the theoretical calculations presented in this thesis. Without their contribution the correct interpretation of the experimental data would be hardly possible.

I declare that I carried out this doctoral thesis independently, and only with the cited sources, literature and other professional sources.

I understand that my work relates to the rights and obligations under the Act No. 121/2000 Sb., the Copyright Act, as amended, in particular the fact that the Charles University in Prague has the right to conclude a license agreement on the use of this work as a school work pursuant to Section 60 subsection 1 of the Copyright Act.

In ..... date ..... Mgr. Mykola Telychko

Název práce: Studium možností funkcionalizace grafénu pomocí metod AFM a STM

Autor: Mykola Telychko

Katedra: Katedra fyziky povrchů a plazmatu

Vedoucí disertační práce: Ing. Pavel Jelínek, Ph.D., Fyzikální ústav AVČR, v.v.i.

Abstrakt: Tato práce studuje metodou STM všechny fáze růstu, které se vyskytují v průběhu postupného žíhání substrátu SiC(0001), a které vedou ke vzniku hraniční vrstvy a jednovrstevného grafénu. Je zde prokázáno, že růst hraniční vrstvy je způsoben slučováním grafénových nanobublinek, které vznikaji v důsledku odpařování Si ze substrátu a že tento proces účinně soutěží s tvorbou málo probádané fáze $5\sqrt{3} \times 5\sqrt{3}$, pro kterou jsme našli atomární model.

Studovali jsme grafén zároveň nc-AFM a STM. Touto technikou se nám podařilo zvlášť určit topografické a elektronické vlastnosti povrchu grafénu na SiC(0001). Analýza odhalila, že drsnost grafénu získaná z map atomární síly je velmi nízká, v souladu s teoretickými předpověďmi.

Dále jsme vyvinuli metodu přípravy vysoce kvalitního grafénu na SiC(0001) dopovaného příměsemi B a N. Kombinace experimentálních (STM, nc-AFM, XPS, NEXAFS) a teoretických (DFT a simulace STM) metod umožnila zjistit strukturální, chemické a elektronické vlastnosti jednotlivých substitučních příměsí v grafénu. Ukazujeme, že i pouhým STM lze dosáhnout chemického rozlišení příměsí B a N díky kvantově interferenčnímu jevu, který nastává v důsledku specifické elektronové struktury příměsi N. Chemická reaktivita příměsí B a N byla zkoumána spektroskopií sil pomocí nc-AFM.

Klíčová slova: grafén, SiC, dopovani, STM, nc-AFM

Title: Studying possibilities of graphene functionalization using AFM and STM techniques

Author: Mykola Telychko

Department: Department of Surface and Plasma Science

Supervisor: Ing. Pavel Jelínek, Ph.D., Institute of Physics ASCR, v.v.i.

Abstract: In this thesis, by means of STM we study all the stages that occur during stepwise annealing of the SiC(0001) substrate, and lead to the formation of buffer layer and to the single layer graphene. It is demonstrated that the buffer layer growth is initiated by merging of graphene nanobubbles arising due to Si depletion and that this process competes with formation of a largely neglected phase, the $5\sqrt{3} \times 5\sqrt{3}$, for which we develop an atomistic model.

We studied the single-layer graphene using a simultaneous nc-AFM/STM. By this technique we are able to separate the topographic and electronic contributions from the overall landscape. The analysis reveal that graphene roughness evaluated from the atomic force maps is very low, in accord with theoretical simulations.

Furthermore, we report a method for preparation of high-quality B- and N-doped graphene on SiC(0001). We combine experimental (nc-AFM, STM, XPS, NEXAFS) and theoretical (total energy DFT simulated STM) studies to analyze the structural, chemical and electronic properties of the single-atom substitutional dopants in graphene. We show that chemical identification of B and N substitutional dopants can be achieved only with the STM due to the quantum interference effect, arising from the specific electronic structure of N dopant sites. Chemical reactivity of the single B and N dopants is analyzed using force-distance spectroscopy by means of nc-AFM.

Keywords: graphene, SiC, doping, STM, nc-AFM

Contents

Introduction

Graphene is a single sheet of carbon atoms arranged in the two-dimensional honeycomb lattice (see Figure 1a). A graphene unit cell consists of two atoms residing in two nonequivalent sublattices: A (blue) and B (yellow). As a consequence the Brillouin zone of the reciprocal lattice has two inequivalent corners K and K′.

In this configuration every C atom has three in-plane sp^2 orbitals and one out-of-plane p_z orbital. The hybridization of p_z orbitals gives rise to the π and π^* bands in the band structure of graphene (see Figure 1b), which are responsible for the extraordinary electronic properties of graphene. The π and π^* bands cross in the so-called Dirac points (K and K′ points of the Brillouin zone), which are located exactly at the Fermi level. Hence, graphene is assumed to be a zero bandgap semiconductor [1].

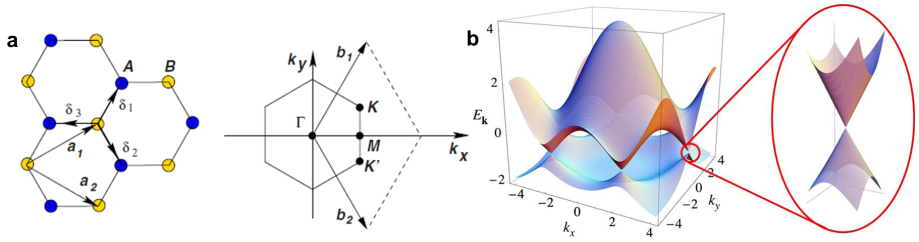

Figure 1: a) Graphene honeycomb lattice (comprised of two sublattices A and B and its Brillouin zone. b) Electronic dispersion of the honeycomb lattice calculated using the tight-binding approach. The images have been adapted from [1].

The π bands in the vicinity of Dirac point follow a linear dispersion relation:

$$E_{\pm} = \pm \hbar V_F K, \tag{1}$$

where $\hbar$ is a reduced Planck constant, V_F is the Fermi velocity (1×10^6 m/s), K is a wave vector and the $\pm$ is related to electrons and holes. Due to linear $E(k)$ dispersion of π bands the effective electron mass is zero and they behave as massless Dirac fermions [2].

The band structure of graphene was first studied theoretically in 1947 by P. Wallace with tight-binding approach [3]. However, the true breakthrough of graphene science, probably started more than 50 year after, when K. Novoselov and A. Geim reported their experiments on the exfoliation of a single layer graphite sheets [4, 5]. Since then, the attention of the scientific community towards this material increased drastically and a lot of graphene unique electronic properties were discovered, e.g. half-integer quantum Hall effect, high carrier mobility etc. [1, 6].

Despite the rich physics, graphene implementation into the real working de-

vices possess some obstacles which still have to be overcome. Firstly, technological process requires large high-quality graphene sheets. Ideally the following parameters should also be satisfied: low production cost, scalability, reproducibility and high quality of the graphene sheets. Secondly, the robust and reproducible methods allowing intentional tuning of the graphene electronic properties, are necessary.

Historically, the first method for the graphene production was micromechanical cleavage of the graphite ("scotch-tape" method) proposed by A. Geim [4]. This approach results in high-quality graphene sheets with size up to 1 mm. However, it is not suitable for large scale production of the graphene and it is mainly employed in the fundamental research. Alternatively, graphene can be produced by the reduction of the graphene oxide [7]. In this case at first graphite is deliberately oxidized to the graphite oxide to reduce coupling between the layers. Ultrasonic treatment in the presence of water allows exfoliation of the graphene oxide layers. Later, this graphene oxide can be chemically reduced [7]. This method is scalable and reproducible but results in low-quality graphene films.

At the current stage the two methods of graphene preparation are suitable for practical applications. The first is thermal decomposition of hydrocarbon precursors on the catalytic metal, so-called chemical vapor deposition (CVD) method [8]. Here, the synthesis of graphene on the copper foil is the most widely used. The graphene grown on the metal can be later transferred onto an arbitrary insulating substrate (e.g. SiO_2 or boron-nitride) [9]. The CVD method is scalable, controllable and suitable for the mass production of graphene sheets.

The alternative way to produce high-quality graphene is graphitization of silicon carbide (SiC) [10, 11, 12]. Due to high vapor pressure Si atoms sublime from the SiC substrate upon its annealing at high temperatures. The remaining C atoms form graphene layers. This approach was used in this thesis. Partially, this choice is dictated by the following reasons: possibility to grow high-quality graphene layers, wide availability and decreasing cost of the SiC. The SiC is well-known large-bandgap semiconductor with excellent thermal conductivity and high electron mobility, widely used in electronics [13, 14]. Therefore, in future, graphene/SiC device manufacturing could be relatively easily incorporated into the current technological process.

In fact, in 2004 C. Berger *et al.* demonstrated that epitaxial graphene on SiC(0001) exhibits a properties of the two-dimensional electron gas similarly to the exfoliated graphene, by means of magnetoresistance measurements [15]. Moreover, authors showed the possibility to control the density of charge carriers by electrostatic gating. Later studies have also proven that epitaxial graphene on SiC is a promising candidate for the applications, e.g. is suitable for fabrication of high-frequency transistors [16, 17]. Indeed, Lin *et al.* fabricated the top gated

field-effect transistor on the graphene on SiC(0001) with a top cutoff frequency of 100 GHz [18, 19]. On the other hand, the properties of epitaxial graphene are strongly affected by the underlying SiC substrate and the morphology of the interface [20]. Thus, understanding the interplay between the structural and electronic properties of the graphene/SiC, as well as a graphitization process is a crucial factor for future device construction.

Chemical doping is a promising route for tuning graphene charge carrier densities for the applications in nanoelectronics [21]. From this perspective, boron (B) and nitrogen (N) atoms are the most suitable candidates for direct incorporation into the graphene honeycomb lattice, because their atomic radii are very similar to that of carbon. Substitution of B and N in graphene lattice result in an effective p- and n-doping effects, respectively (see Figure 2) [12]. Moreover, recent experimental and theoretical investigations pointed out the possibility of band gap opening by low-concentration BN-doping of graphene [22, 23, 24]. This would overcome one of the major obstacles on the way towards applications in electronic switching devices. On the other hand, any experimental studies of the B-doping or BN-co-doping of graphene on SiC substrate have not been reported yet.

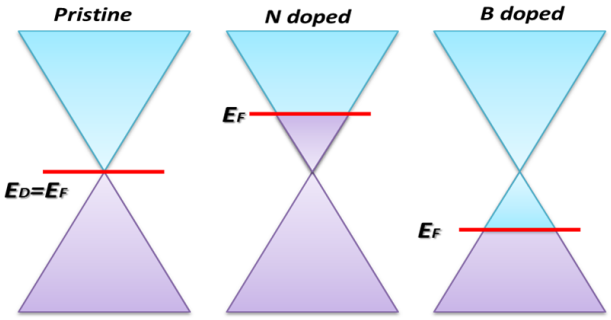

Figure 2: A schematic showing a relative shift of the Dirac point with respect to the Fermi level induced by incorporation of substitutional N and B dopants into the graphene lattice.

Due to reasons discussed above we studied the possibility of functionalization of graphene/SiC(0001) by the substitutional B and N doping. The thesis is organized as following. In the Chapter 1, all used experimental techniques are summarized. The Chapter 2 deals with growth mechanism and structural properties of epitaxial graphene on the SiC(0001) substrate. The Chapter 3 is devoted to a developed approach for the graphene/SiC(0001) substitutional doping by the B and N atoms. We present investigation of the doping process at the atomic scale. Our study is based on various surface science techniques (nc-AFM, STM, NEXAFS, XPS) and supported by total energy calculations.

1. Experimental techniques

1.1 Scanning tunneling microscopy

1.1.1 Basic principle of operation

The first scanning tunneling microscope (STM) was developed by Binning and Rohrer in 1981 in the IBM Research Laboratory [25, 26]. The STM is based on the effect of quantum tunneling of electrons through potential barrier between two electrodes. The first electrode is a sharp metallic tip attached to the piezo tube and the second electrode is a conducting or semiconducting surface. The distance between the tip and sample is only a few Å, so their wavefunctions are overlapping. Bias voltage is applied between the tip and the sample to induce the tunneling current flow. When the tip is biased positively (negatively) with respect to the sample occupied (empty) states of the surface are probed. As it will be shown in the next subsection the tunneling current depends exponentially on the tip-sample distance. For instance, it might vary in one order of magnitude when the tip-sample distance is changed for 1Å. This extreme sensitivity of the tunneling current on the tip-sample separation is a key for atomic resolution in the STM.

The piezo tube scanner allows raster moving of the tip over the surface with Å precision. By recording the tunneling current value in every point over the sample the current map is produced. The tunneling current map contains convoluted information about the topographical and electronic properties (e.g. local density of the electronic states) of the surface.

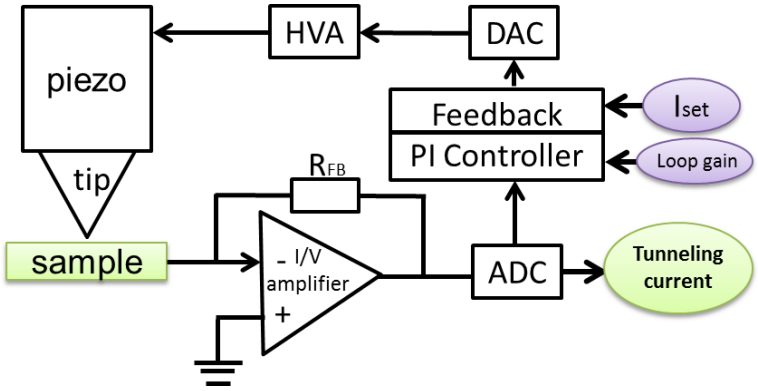

Figure 1.1: Schematic drawing of the STM setup

Basic components of the STM setup are schematically shown in the Figure 1.1. At first, the measured tunneling current is converted to the voltage by the I/V amplifier. Later the feedback loop determines the error signal as a difference between the instant value of the tunneling current and the reference value (cur-

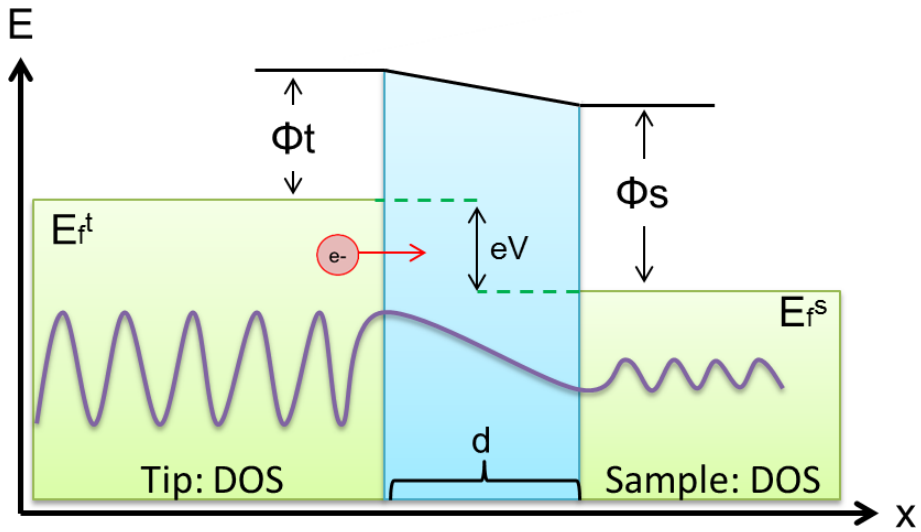

Figure 1.2: Energetic diagram of the tunneling junction between the two ideal metals (adapted from J. Chen [27]).

rent setpoint). The error signal is fed to proportional-integral controller (PIC). Through the high-voltage amplifiers (HVA) the PIC output controls the voltage applied to the z-piezo and, thus, the tip-sample separation. In the modern STM instruments the feedback loop is digital, it is realized using analog-to-digital (ADC) and digital-to-analog (DAC) converters and digital PIC. Depending on the settings of the feedback loop the two main operation modes are possible in the STM: constant current and constant height mode. In the constant current mode the closed feedback maintains the tunneling current setpoint by adjusting the tip-sample distance. In the constant height operation mode the feedback loop is open and the tip-sample separation is kept constant through the scan. In some cases this mode allows to achieve better resolution and signal-to-noise ratio, but due to possibility of the tip crash it is applicable only for flat areas of the surface.

For achieving of atomic resolution in the STM, the scanning head must be vibrational isolated from the surrounding environment. This is commonly obtained by applying suspension spring system and magnetic damping mechanisms. Advanced STM instruments allow cooling the STM head down to extremely low temperatures ensuring superior thermal stability of the system.

1.1.2 Theory of scanning tunneling microscopy

The tunneling process can be phenomenologically described within the one - dimensional tunneling junction model as shown in the Figure 1.2. The electron with energy E is impinging the rectangular tunneling barrier ($V(x)$) with a width (d). The barrier height can be approximated as an average of the tip and the sample work functions. The barrier width corresponds to the tip-sample separation. The time-independent Schrödinger equation for the one dimensional case is:

$$E\Psi(x) = -\frac{\hbar^2}{2m}\frac{\partial^2\Psi(x)}{\partial x^2} + V(x)\Psi(x), \tag{1.1}$$

where $\Psi(x)$ is electron wavefunction, $\hbar$ is reduced Planck constant, m is electron mass and $V(x)$ is a potential barrier. The one of the possible wave function solution of this Schrödinger equation is:

$$\Psi(x) = \Psi(0)\exp^{\pm ikx}, \tag{1.2}$$

with

$$k = \frac{\sqrt{2m(E-V)}}{\hbar}\ . \tag{1.3}$$

The transmission coefficient T defining possibility of electron penetration through the barrier will be:

$$T = \frac{1}{1 + \frac{V_0^2 sinh^2(kd)}{4E(V-E)}} = \frac{16E(V-E)}{V^2}\exp^{-2kd}. \tag{1.4}$$

The transmission coefficient T decays exponentially with barrier width (d). This exponential dependence is a key for atomic resolution in the STM, because the highest tunneling current passes through the outermost atom of the tip, which is closest to the surface.

The one-dimensional approach, however, is not applicable for the realistic systems since the electronic properties of tip and the sample are not taken into account. For the qualitative description of the tunneling process, densities of the electronic states (DOS) of the tip and the sample should be considered. Within the Bardeen theory [28] the expression for the tunneling current is following:

$$I(V,x) \propto \int_{E_F}^{E_F+eV} \rho_s(E)\rho_t(E+eV)|M(E,V)|^2 dE, \tag{1.5}$$

where I is a tunneling current density, E_F is a Fermi energy, ρ_s and ρ_t are densities of the electronic states of the sample and tip, respectively. *M(E,V)* is a transition matrix element defined by overlapping of the tip and sample wavefunctions [28]:

$$M(E,V) = \frac{\hbar^2}{2m}\int(\psi_S^*\nabla\psi_T - \psi_T\nabla\psi_S^*)dA, \tag{1.6}$$

where the integration is done over the surface A within the tunneling region. In the real experiment the wave function of the tip is unknown, therefore reliable calculation of *M(E,V)* is only possible for the simplified tip models. For example, Tersoff-Hamann theory tip assumes a tip with a spherical (s-shape) orbital [29]. Moreover, the following assumptions are made i) tip has flat DOS ($\rho_t(E)$=*const*)

ii) low bias voltage is applied ($M(E,V)$=*const*). Considering this assumptions the equation [1.5] can be further simplified:

$$I(V,x) \propto \int_{E_F}^{E_F+eV} \rho_s(E)dE. \tag{1.7}$$

From the equation [1.7] it is evident that within the Tersoff-Hamann approximation the tunneling current is simply proportional to the local density of electronic states (LDOS) near the Fermi level of the sample. Thus, this approach is suitable for the simulation of the STM images in cases when the electronic structure of the tip can be neglected.

In the case when tips with p or d-like orbital at the tip apex must be considered the more sophisticated Keldysh-Green's function formalism is used [30]. This approach also includes the effects of multiple electron scattering in the tunneling junction.

1.1.3 Scanning tunneling spectroscopy

From the equation [1.7] it is visible that tunneling current contains information about the LDOS of a surface. Differentiating this equation yields the dynamic conductance dI/dV, which reflects information about the sample LDOS as a function of energy:

$$\frac{dI}{dV} \propto \rho_s(E). \tag{1.8}$$

The technique exploiting the tunneling current differentiating with respect to the bias voltage is called Scanning Tunneling Spectroscopy (STS). Depending on the polarity of the bias voltage unoccupied and empty states of the sample can be accessed. Importantly, in the equation [1.8] we assume the tip with flat DOS ($\rho_t(E)$=*const*) which might be not the case in real experiment. This can result in additional features in the dI/dV spectra. Thus interpretation of the dI/dV spectra is not always straightforward and theoretical support is needed.

The are two basic approaches for the recording of the dI/dV spectra. One way is a simple numerical derivation of the $I-V$ curve with respect to the voltage. However, this method suffers from a low signal-to-noise ratio. Alternatively, the dI/dV spectra can be recorded using lock-in technique. Within this approach, the bias voltage is modulated by high frequency sinusoidal signal (V_{AC}):

$$V = V_{bias} + V_{AC}sin(\omega t), \tag{1.9}$$

where V_{AC} is a modulation voltage, ω is a modulation frequency. The modulation frequency must be higher than the cutoff frequency of the feedback loop. Later, the tunneling current signal is converted to voltage and fed to the lock-in

amplifier simultaneously with reference modulation signal. The output signal of the lock-in amplifier is directly proportional to the dI/dV. For the more detailed description of the lock-in technique and its implementation in the STS we would refer to [31].

1.2 Atomic force microscopy

1.2.1 Basic principle of operation

In the Atomic Force Microscope (AFM), imaging signal is a force acting between the tip and the sample. Therefore, unlike in the STM, insulating surfaces can be also studied with AFM. The key component of AFM is a cantilever which bends with respect to the-tip sample force. The cantilever type is defined by the three main parameters: spring constant (k), eigenfrequency (f_0) and quality factor (Q). Commonly optical deflection scheme is employed to define bending of the cantilever. In this setup the cantilever bending creates displacement of the laser beam reflected from the back side of the cantilever [32]. The beam displacements are further measured by a four-sector diode. Another alternative scheme employing the piezoelectric effect is used in the Q-plus [33] and needle sensors (e.g. Kolibri sensors manufactured by Specs) [34]. The sensors are made from quartz, therefore their bending induces piezoelectric voltage which is directly proportional to the deflection. In this thesis both Q-plus and Kolibri sensors were used. The schematic sketch of the home-build Q-plus sensor is shown in the Figure 1.3a.

The two main operation modes in the AFM are static and dynamic or non-contact (nc-AFM). In the static mode the total tip-sample force (F_{tot}) causes the static deflection (q) of the cantilever with stiffness k, so that ($q = F_{tot}/k$). However this mode has a significant limitation for the achieving of atomic resolution. The cantilever with insufficient stiffness experiences strong attractive force, consequently the scanning is destructive for both the tip and the sample. This drawback is solved in the dynamic mode, when the cantilever is deliberately oscillated around its resonance frequency. The changes in the cantilever oscillation frequency reflect the tip-sample interaction.

The two different types of operation modes exist in the dynamic AFM: amplitude modulated (AM-AFM) and frequency modulated (FM-AFM). In the AM-AFM cantilever is driven at the fixed drive frequency and excitation amplitude. The tip-sample interaction affects the oscillation amplitude. This amplitude changes are further employed as a feedback signal [35]. In the FM-AFM mode oscillation amplitude is kept constant by the feedback loop and changes in the cantilever oscillation frequency act as a feedback signal [36]. The application of

FM-AFM mode is more preferential in the UHV conditions since it allows much faster operation in comparison to AM-AFM [36].

All nc-AFM experiments presented in this thesis were carried in a constant height mode, i.e. without active z-feedback. The simplified scheme of nc-AFM setup is illustrated in the Figure 1.3b. The deflection signal from Q-plus or Kolibri sensor is measured and fed to the phase-locked loop (PLL). The PLL determines the frequency shift (Δf) as a difference between actual frequency (f) and the resonant frequency value (f_0). At the same time, the constant oscillation

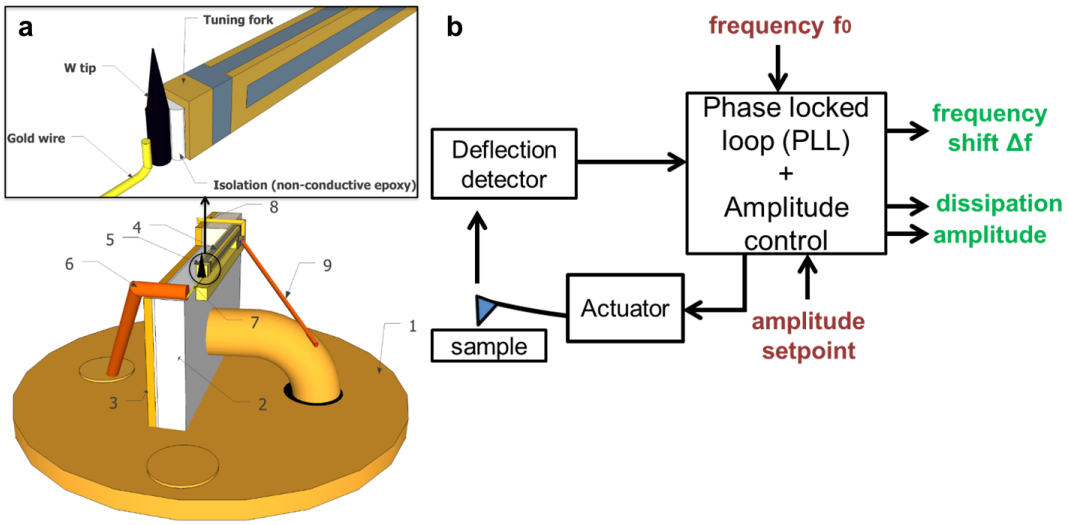

Figure 1.3: a) A sketch of the home-made Q-plus sensor adapted from [37]. b) Block diagram of the nc-AFM setup.

amplitude is maintained using the amplitude feedback controller. The output signal of amplitude controller is proportional to difference between instant (A) and setpoint amplitude (A_{set}) value. This signal is fed to actuator exciting a sensor.

1.2.2 Theory of atomic force microscopy

The movement of the oscillating cantilever can be treated as harmonic oscillator. Its motion equation is:

$$m\ddot{z} + k\dot{z} = kA_{drive}cos(2\pi f_0 t), \tag{1.10}$$

where m is effective mass of the cantilever, k is a spring constant, f_0 resonant frequency, A_{drive} is a driving amplitude. One solution of this equation is:

$$z(t) = Acos(2\pi f_0 t), \tag{1.11}$$

with the resonance frequency:

$$f_0 = \frac{1}{2\pi}\sqrt{\frac{k}{m}}. \tag{1.12}$$

When oscillator is exposed to an external force field with spring constant $k_{ts} = dF/dz$ its new resonance frequency will be:

$$f = \frac{1}{2\pi}\sqrt{\frac{k + k_{ts}}{m}}. \tag{1.13}$$

For the small oscillation amplitudes the force gradient remains constant through the oscillation cycle. In addition, if the force gradient is much smaller than stiffness of the cantilever $k \ll k_{ts}$, the frequency shift can be written as:

$$\Delta f = f - f_0 \approx \frac{k_{ts}}{2k} f_0, \tag{1.14}$$

which means that in FM-AFM the frequency shift is proportional to the tip-sample force gradient rather than force in assumption of small oscillation amplitudes.

For large oscillation amplitudes, a force gradient changes through the oscillation cycle. In this case, the relation between the frequency shift and force valid for the arbitrary oscillation amplitude was derived by F. Giessibl, who applied first-order perturbation theory in the Hamilton-Jacobi approach [38]:

$$\frac{\Delta f}{f_0} = -\frac{1}{\pi A k}\int_{-1}^{1}(F(z + A(1+u))\frac{u}{\sqrt{1-u^2}}du. \tag{1.15}$$

Later the interaction force can be determined from the $\Delta f(z)$ dependence using the approach proposed by J. Sader and S. Jarvis [39]:

$$F(z) = \frac{2k}{f_0}\int_{z}^{\infty}(1 + \frac{\sqrt{A}}{8\sqrt{\pi(t-z)}})\Delta f(t) - \frac{A^{3/2}}{\sqrt{2(t-z)}}\frac{d\Delta f(t)}{dt}dt. \tag{1.16}$$

This equation is applicable for any oscillation amplitude and is independent on the nature of force. Alternatively the $\Delta f(z)$ can be converted to the $F(z)$ using an inversion of a convolution matrix proposed by F. Giessibl [40].

As shown in the Figure 1.4a the total force acting between the tip and the sample is a sum of long and short range forces. The long range forces consist of macroscopic van der Waals (vdW) force and electrostatic force. The vdW force is caused by the fluctuations of the dipole moments and varies as r^{-6} with the distance (r) between the two atoms. It can be estimated using the so-called Hamaker approach:

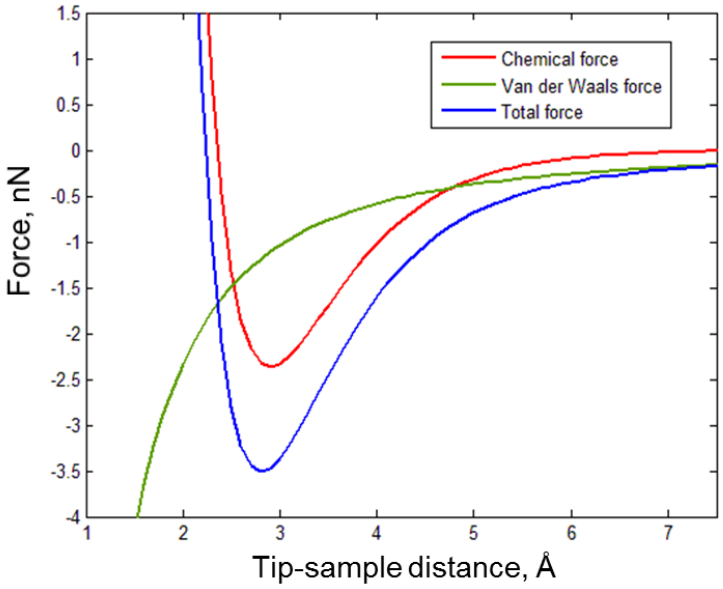

Figure 1.4: Forces acting-between the tip and the sample.

$$F_{vdW} = -\frac{A_H R}{6(z - z_0^2)}, \tag{1.17}$$

where A_H is a Hamaker constant, R is the radius of a tip apex and z is a tip-sample distance.

The electrostatic force is caused by the electrostatic potential difference between the tip and sample. The tip and sample can be treated as a capacitor with capacitance (C). In this case the electrostatic force can be approximated as:

$$F_{el} = -\frac{1}{2}\frac{dC}{dz}(V - V_{CPD})^2, \tag{1.18}$$

where C is a distance dependent tip-sample capacitance, V is a bias voltage and V_{CPD} is a contact potential difference between tip and sample. Thus, the contribution of the electrostatic force can be nullified by applying the bias voltage which is equal to V_{CPD}.

The short-range forces are the chemical forces related to chemical bond formation and repulsive forces arising due to Pauli exclusion principle. These forces become significant at distances when tip and sample wavefunctions start to overlap. The short-range forces vary at the atomic scale are key for atomic resolution in the AFM. Recently, the capability of AFM in the chemical identification and resolving the chemical structure of the molecules was achieved [41, 42].

1.3 Photoelectron spectroscopy

The Photoelectron spectroscopy (PES) was an additional technique used in this thesis. It is based on photoelectric effect which is a phenomenon of electrons emission from the sample as a result of its exposure to the monochromatic light. Every photoemission process consists of three steps: photon adsorption, creation of the photoelectron and electron transport to the surface. According to the Einstein equation the kinetic energy of the emitted electrons (E_{kin}) depends on their binding energy in the substrate (E_B), work function of the substrate (Φ) and the energy of incident light ($\hbar\omega$):

$$E_{kin} = \hbar\omega - E_B - \Phi. \tag{1.19}$$

If the photon energy is higher than sum of the binding energy (E_B) and the sample work function (Φ) the photoelectrons are able to reach vacuum level. The kinetic energy (E_{kin}) of the photoelectrons is subsequently detected by hemispheric analyser. In principle, the PES is a surface sensitive technique, due to low inelastic mean free path of the electron in the bulk (only a few Å). Therefore, only the electrons from the surface can be escaped to the vacuum.

Depending on the incident photon energy different electronic levels can be accessed, as schematically sketched in the Figure 1.5. The valence band electrons are excited by light in the ultraviolet range (UPS). On the other hand, the deeply lying core levels can be excited only by the X-rays (XPS).

The typical XPS spectrum consists of series of peaks appearing at specific binding energies. These peaks originate from the electron states (e.g. 1s, 2s, 2p). The intensity of the peaks is directly proportional to the amount of the corresponding element within the probed area of the surface and cross section.

The core level states must be orthogonal to the valence states. Thus, if valence electrons are involved in the chemical interactions, the core levels shift their energy accordingly. Therefore, the energy position of the peak (chemical shift) reflects information about the chemical environment and oxidation state of a given atom. The inelastic electrons from the electron-electron and electron-phonon scattering events typically produce so-called Shirley background in the XPS spectra, which can be subtracted.

The incident light beam can be produced by the laboratory sources (e.g. Mg K_α with energy 1253.6 eV) or using the synchrotron radiation which allows higher beam intensity, superior monochromasy, energy tunability and, as consequence, higher energy resolution.

Except for the kinetic energy, another quantity characterizing the emitted photoelectrons is their momentum. Within the semiclassical approach the electron momentum (K) consists of two components: parallel ($K_{||}$) and perpendicular

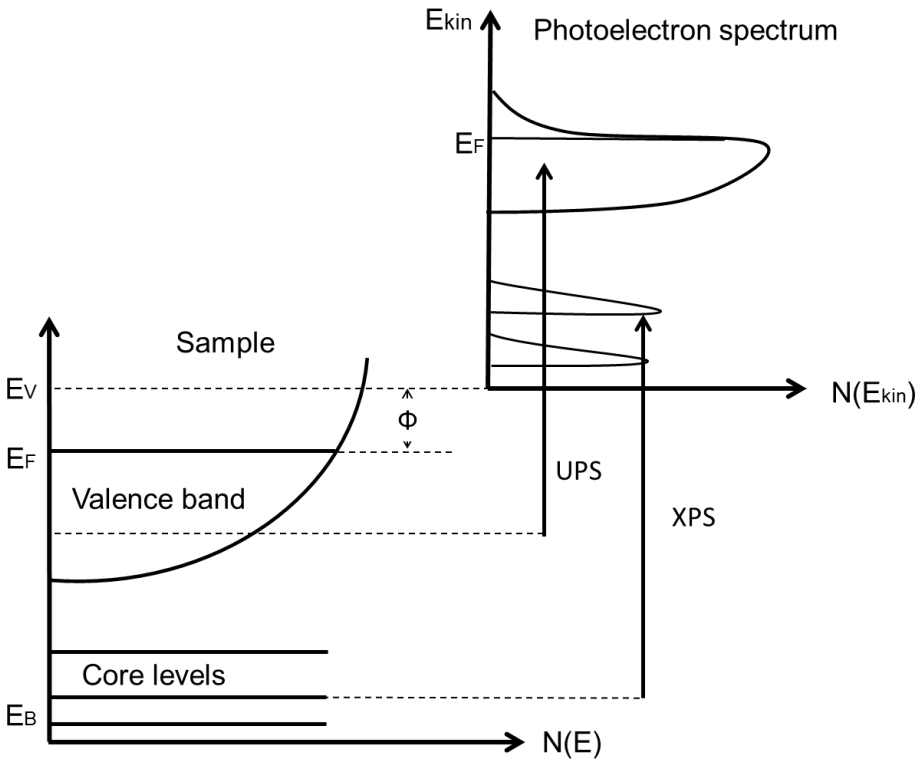

Figure 1.5: Schematic energy diagram of photoelectron emission process (from [43]).

($K_\perp$) to the surface. After the emission only the in-plane component ($K_{||}$) is preserved and can be determined from the emission angle (θ):

$$K_{||} = \sqrt{\frac{2mE_{kin}}{\hbar^2}} sin(\theta), \tag{1.20}$$

where m is electron mass, θ is emission angle, $\hbar$ is a reduced Planck constant.

The $K_{||}$ directly reflects information about electron momentum inside the sample. By using the angle-integrating photoelectron analysers angular distribution of the valence-band emitted photoelectrons can be measured. This technique is called Angle Resolved Photoelectron Spectroscopy (ARPES). It allows to study the dispersions of the electronic bands in the different directions and other electronic properties (e.g. the Fermi surfaces) of the sample.

1.4 Near edge X-ray adsorption spectroscopy

The Near Edge X-Ray Adsorption Spectroscopy (NEXAFS) provides information about the unoccupied electronic states [44]. The NEXAFS measurement is based on a two-step process as shown schematically in the Figure 1.6. At first, X-rays with energy near the ionization edge (K-edge) excite a core electrons into the unoccupied states, by this a photoelectron and a hole is created. The hole is subsequently filled by the electron from the outer shell by Auger decay or

fluorescence process.

The NEXAFS spectra are recorded in a following way. The energy of the incident photons is changed across the K-edge of a particular elements and probability of the photon absorbtion is measured. The three basic approaches for recording the photon absorption are i) the Auger electron yield when the Auger electrons are counted ii) the total electron yield when the sample photocurrent is measured and iii) fluorescent yield when the emitted photons are measured.

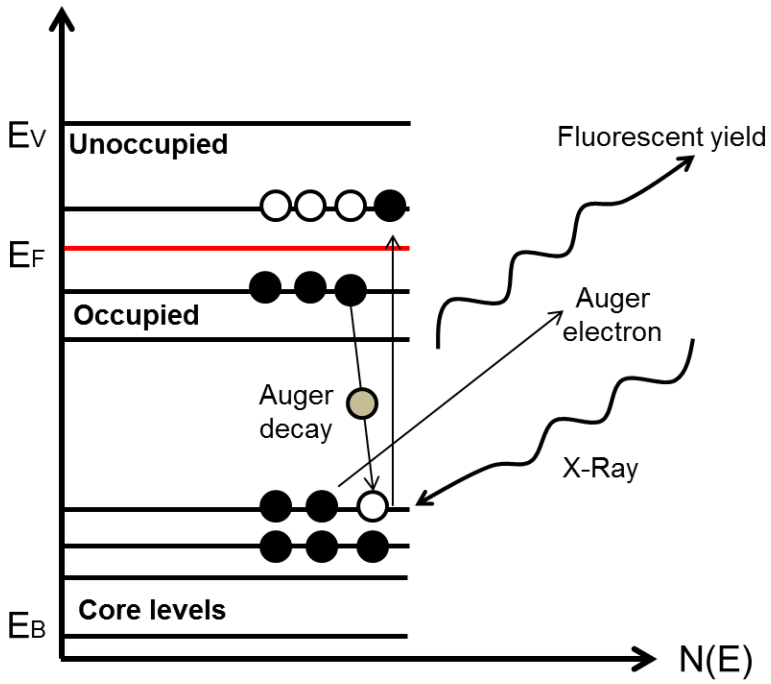

Figure 1.6: Schematic of the NEXAFS process. An incident photon with energy of NEXAFS resonance excites a core electron to the unoccupied states. The created hole is subsequently filled with emission of the fluorescent X-Ray or Auger electron.

The NEXAFS is element-specific technique since every chemical element has a unique adsorption edge. Another advantage of the NEXAFS is its high sensitivity towards bond angles and bond orientation. Due to dipole selection rules mainly the orbitals parallel to the E vector of the incident light are involved in the adsorption process. Thus, the contribution of the particular orbital in the adsorption process can be studied by changing the angle between the incident beam and the sample normal. This can by particularly useful for the graphene because its in-plane σ and out-of-plane π orbitals can be accessed in the normal and grazing beam-sample geometries, respectively.

1.5 Low energy electron diffraction

The Low Energy Electron Diffraction (LEED) is an integral technique for the surface analysis. It is based on the studying of the electron diffraction patterns arising due to crystallinity of the sample. As sketched in the Figure 1.7 the LEED setup consists of electron gun, fluorescent screen and array of grids.

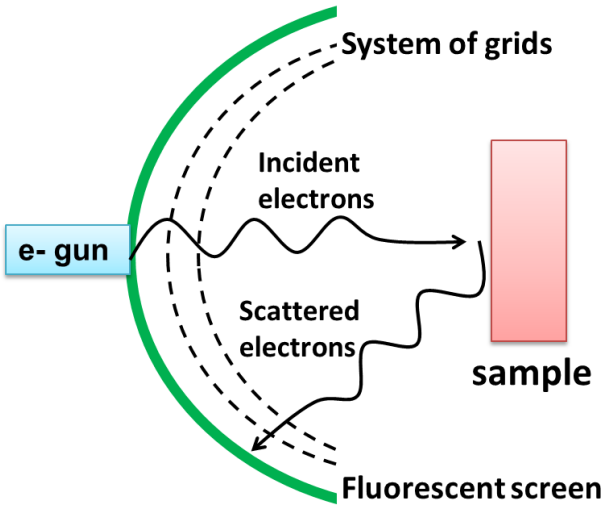

Figure 1.7: Schematics of the LEED setup. The electrons diffracted from the crystal sample form the diffraction pattern observed on the fluorescent screen.

The electron gun irradiates the sample by the beam of electrons. The energy of electrons is set in range of 100 eV, thus, their wavelength is comparable with the lattice constant of the studied crystal. After the interaction with the surface electrons form diffraction picture, which is observed on the fluorescent screen. The diffraction pattern is related to the surface crystallography and directly reflects a reciprocal lattice of the surface [45]. In our experiments, LEED was employed as complementary technique for the characterisation of the surface reconstructions during annealing process of the SiC(0001).

1.6 Theoretical support

All the experimental data in this thesis were supported by the extensive theoretical calculations. The calculations were performed in our group Nanosurf Lab by *Dr. Pavel Jelínek, Dr. Pingo Mutombo, Dr. Prokop Hapala and Dr. Martin Ondráček.*

In the Section 2.4 in order to estimate the corrugation of single layer graphene on the SiC(0001) substrate the large scale total energy density functional theory (DFT) calculations were used. The local-orbital FIREBALL code [46, 47] using an

optimized [48] spatially-confined pseudo-atomic numerical orbital basis set was applied. In our case, an ss^* basis set was used for the H atoms, an sp basis set for the Si and C atoms. Local density approximation was used for the exchange correlation functional. The atomic models of the SLG-SiC(0001) surface consisted of a slab of 1648 atoms, 10 atomic layers thick (including the buffer and SLG layer) with an additional passivating hydrogen layer on the underside. The lateral size of the supercell was $6\sqrt{3}\times6\sqrt{3}$. The calculations were restricted to the Γ point of the first surface Brillouin zone. The bottom Si atomic layer as well as the hydrogen layer were kept fixed during the geometry optimization while all other atoms were allowed to relax freely into their equilibrium positions. The criterion for terminating the relaxation was that maximal forces on free atoms had to be below 0.05 eV/Å and the change of total energy between subsequent iterations had to be smaller than 10^{-4} eV per unit cell.

In the Section 3 to simulate the B-, N- and BN doped graphene also the local orbital Fireball DFT code [47, 49] based on optimized pseudo-atomic *spd* orbital basis set [50] was applied. Very similar optimized structure was also reached with Vienna Ab Initio Simulation Package (VASP) [51], a plane-wave *ab initio* code using Vanderbilt ultrasoft pseudopotentials [52]. All the STM simulations of doped graphene presented in this thesis were performed using the STM module within the Fireball code using Green's function approach [53]. A preoptimized (111)-oriented C tip with diamond-like structure was used to generate constant-height maps of current for comparison with the STM experimental images.

1.7 Experimental setup and sample preparation

During work on this thesis we used UHV machines available in the Institute of Physics of the Czech Academy of Science. The results from the Section 2 were mainly obtained on the VT-STM Omicron and modified VT-AFM/STM Omicron using Q-plus setup (see Figure 1.8a). A homebuilt quartz-tuning fork sensor was used for the measurements. The contact to the tungsten tip was made of a thin golden wire in order to avoid crosstalk with the deflection signal from the tuning fork piezo [37, 54]. The results from the Section 3 were obtained using LT-AFM/STM Specs machine operating below 2K and allowing simultaneous force/current detection scheme using Kolibri sensor (see Figure 1.8b). All machines are equipped by LEED.

The tips for STM and AFM measurements were prepared by electrolytic etching technique. We used in 2 mol NaOH water solution and a 0.5 mm thick tungsten wire with purity 99.99 %. To minimize the cutoff time of the electrochemical reaction we used the electronic control circuit proposed by Ibe *et al.* [55]. After the insertion into the chamber, the tips were commonly treated by annealing to

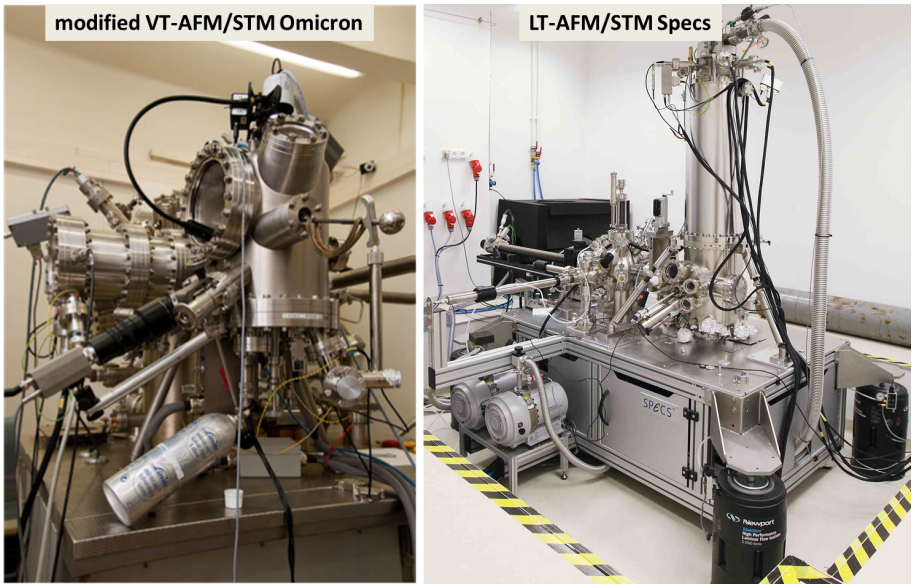

Figure 1.8: Pictures of a) modified VT-AFM/STM Omicron machine using Q-plus setup b) low temperature AFM/STM Specs machine.

1200°C in a contact with a hot tungsten filament or Ar^+ ions sputtering.

The XPS core levels and NEXAFS spectra were measured at the Materials Science Beamline at the Elettra synchrotron. The element specific K-edge absorption Auger electron yield was integrated at the valence band (from a binding energy of 60 eV to the Fermi level).

For the N^+ ions sputtering we used a standard ion source IQE 11/35 from Specs. During experiments on the B doped graphene as a source of boron we used a heavily B-doped Si wafer annealed by direct current to 1200°C. The high amount of B in the Si wafer allowed deposition of B atoms onto the SiC sample along with the flux of Si. For achieving higher B concentration pure B was deposited from an e-beam heated B-filled graphite crucible.

For the graphene growth we used N-doped Si-face 6H-SiC(0001) and 4H-SiC(0001) wafers, which were cut into 3 mm × 10 mm stripes and mounted into molybdenum sample holders constructed for a direct-current sample heating. During the annealing process the temperature of the sample was measured using an optical pyrometer with spectral emissivity set to 0.6, operating at 1.6 μm wavelength and focused onto a spot on the sample with diameter <2mm.

2. Graphene on SiC(0001)

2.1 Background

The graphitization of silicon-carbide (SiC) is a well known phenomenon and was first reported in 1965 by D. Badami [56]. At sufficiently high temperatures Si sublimes from the surface due to high vapor pressure and remaining C atoms form graphite. The first systematic study of the influence of annealing on SiC(0001) was performed a decade later by Van Bommel et al. [57]. Using Auger electron spectroscopy and LEED techniques the authors revealed basic crystallographic orientation between the graphite layer and the SiC. In 2004, C. Berger and coworkers reported the existence of Shubnikov–de Haas oscillations in the graphene/SiC(0001) - the distinct property of the two-dimensional electron gas system [15]. It was the first unambiguous proof that in spite of presence of SiC(0001) substrate the electrons in epitaxial graphene still have properties similar to the freestanding graphene.

In principle, the two polar surfaces Si-face SiC(0001) and C-face SiC(000$\bar{1}$) are suitable for the graphene growth. However, annealing of the C-face SiC(000$\bar{1}$) produces a multiple rotationally disordered graphene layers [58]. The growth of homogenous single layer graphene sheets at current moment cannot be achieved. On the other hand, the Si-terminated SiC(0001) substrate allows growth of single and bilayer graphene sheets in a well-controlled manner [59]. Therefore, in this thesis we used SiC(0001) substrates for the growth of graphene.

This Section is devoted to an atomic scale study of the SiC(0001) graphitization in the UHV conditions by means of the STM. Next, we investigate the structural properties of the epitaxial graphene on SiC(0001) using the simultaneous nc-AFM/STM technique. Finally, we will describe our apparatus to grow uniform layers of graphene under Ar atmosphere. The results presented in the Section 2.4 have been already published [60].

2.1.1 SiC polytypes

The bulk crystal structure of the SiC is produced by stacking of the basal plane bilayers of the Si and C. SiC has more than 200 different polytypes. The most popular polytypes are the 3C-SiC with cubic unit cell and 2H-SiC, 4H-SiC, 6H-SiC with hexagonal unit cell. The 2H-, 4H- and 6H- polytypes are distinguished by the number of bilayers per unit cell and contain 2, 4 and 6 bilayers, respectively (see Figure 2.1) [61]. The distance between bilayers is 2.52 Å [62]. The height of unit cell is 10.08 Å for the 4H-SiC polytype and 15.12 Å for the 6H-SiC polytype.

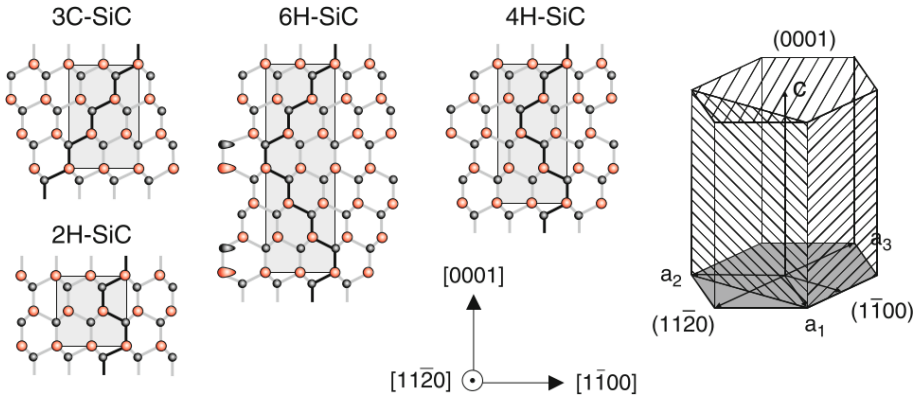

Figure 2.1: Side view projection onto the (11$\bar{2}$0) plane of the crystal structure of four different polytypes of SiC. The hexagonal unit cell indicating the orientation of the (0001), (11$\bar{2}$0) and the (1100) planes is also shown. The (0001) surface has only Si atoms in the topmost layer and the opposite (000$\bar{1}$) face only C atoms. From [62].

The SiC surface can be terminated whether by the Si (Si face) or by C (C face). Crystallographically the Si-face corresponds to the (0001) hexagonal orientation while the C-face is related to the (000$\bar{1}$) direction. In this thesis, we used exclusively 6H-SiC(0001) and 4H-SiC(0001) wafers.

2.1.2 Metastable reconstructions on SiC(0001)

The characteristic structures on the SiC(0001) arise due to a system inclination to minimize the number of free dangling bonds. This results in a formation of different adatom reconstructions with distinct periodicity. These reconstructions appear on the surface as a result of the annealing process. When the annealing temperature exceeds 750°C the Si sublimation from the surface is initiated. The annealing at higher temperatures decreases fraction of the Si-rich phases and favors formation of the C-rich phases.

All the major experimental findings about the SiC(0001) reconstructions and their mutual transformations are summarized in the reviews by P. Martensson *et al.* [63] and U. Starke [59]. In the Figure 2.2, we present a set of the LEED and STM images showing the SiC(0001) surface transformation depending on the annealing temperature. The bare substrate exhibits 1×1 reconstruction (not shown). This reconstruction corresponds to the oxidized surface and was observed only in the LEED studies [64]. After introducing into the UHV conditions the SiC surface must be cleaned from the oxide layer. This is commonly achieved by annealing at 750-800°C in a presence of Si flux. Under the Si flux the surface oxide desorbs as SiO, while the Si is simultaneously supplemented. This method was applied by R. Kaplan [64] for the first time and now it has become widely used in the scientific community. Noteworthy, the sample annealing can be performed

also without the Si flux. However, in this case the average size of the atomic terraces is significantly smaller and resulting surface is too rough for performing STM studies.

After annealing in the presence of Si flux, the surface exhibits an Si-rich 3×3 reconstruction (see Figure 2.2). This reconstruction is formed by the Si adlayer consisting of Si trimer and Si adatom on top (see Figure 2.3a) [65, 66]. Further annealing at 950°C leads to gradual desorption of excessive Si and formation of a Si-rich $\sqrt{3} \times \sqrt{3}R30°$ phase [67, 68, 69, 70]. The $\sqrt{3} \times \sqrt{3}R30°$ reconstruction is formed by one Si adatom which has three Si neighbors from the underlaying SiC bilayer (so-called T4 position) (see Figure 2.3b)[71, 67, 72, 68].

The sample annealing at temperatures above 1050°C causes further depletion of Si from the surface and formation of the C-rich reconstruction with $6\sqrt{3} \times 6\sqrt{3}R30°$ quasiperiodicity (q-$6\sqrt{3}$ later in the text). This transition is well known and has been reported by means of many STM, XPS and LEED studies [63, 59, 12]. However, the transformation from the $\sqrt{3} \times \sqrt{3}R30°$ to the q-$6\sqrt{3}$ at the atomic scale is still not clarified. The nature of the q-$6\sqrt{3}$ will be discussed in detail in Section 2.1.3.

The quasi-periodic $5\sqrt{3} \times 5\sqrt{3}$ (q-$5\sqrt{3}$ later in the text) is an additional characteristic reconstruction which might exist on the SiC(0001). According to the LEED and STM studies this reconstruction also appears on the surface after the annealing at 1050°C [63]. Typically, the q-$5\sqrt{3}$ is observed on a very small fraction (<9%) of the surface [73]. At the current stage, it is still not completely clear what factors favor formation of the q-$5\sqrt{3}$ phase. The study of C. Riedl and coworkers suggests that amount of the q-$5\sqrt{3}$ strongly depends on the applied annealing protocol [74]. In particular, the highest fraction of the q-$5\sqrt{3}$ domains was observed on samples without any previous Si flux treatment.

In general, all the mentioned reconstructions on the SiC(0001) and their mutual transformations are well documented. However, the thermodynamic and kinetic factors driving the phase transformations on the SiC(0001) are not completely understood. For example, it was shown that transition temperatures can be tuned over a wide temperature range by establishing thermodynamic equilibrium between the SiC sample and the external Si vapor pressure [75]. Even the speed of the annealing-cooling process was found to play a crucial role in the morphology of the resulting sample [76].

2.1.3 $6\sqrt{3} \times 6\sqrt{3}R30°$ reconstruction

The exact atomic structure of the q-$6\sqrt{3}$ phase is still a matter of discussion. Already, seminal studies carried by van Bommel *et al.* showed that LEED pattern of the q-$6\sqrt{3}$ reveals spots at positions identical to ones observed on graphite [57]. K. Kim *et al.* proposed that the q-$6\sqrt{3}$ phase is formed by C atoms which

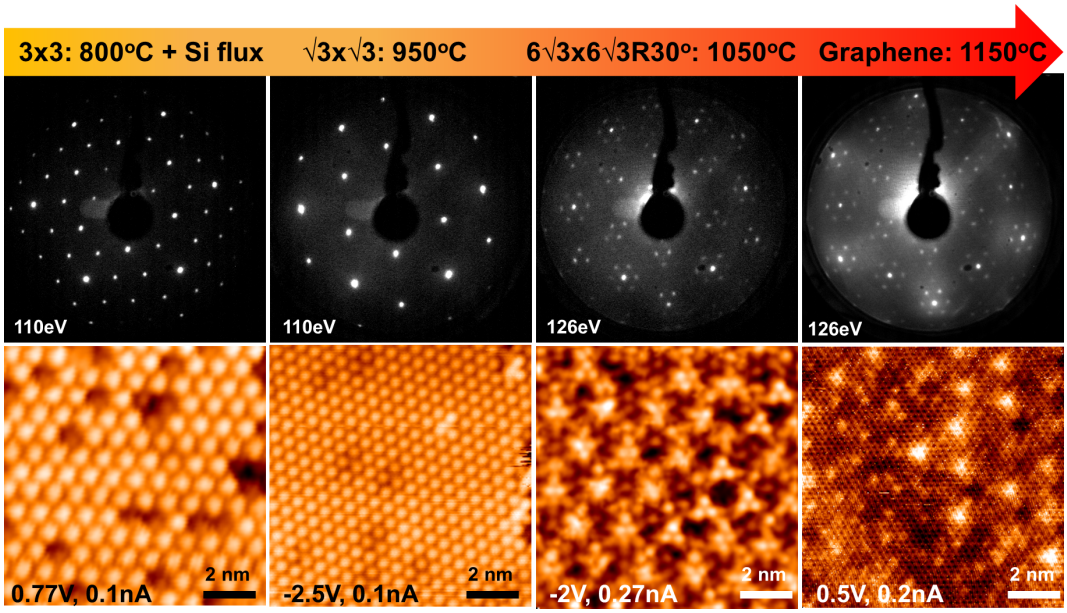

Figure 2.2: LEED patterns and corresponding STM images showing phase transformation on the SiC(0001) upon annealing.

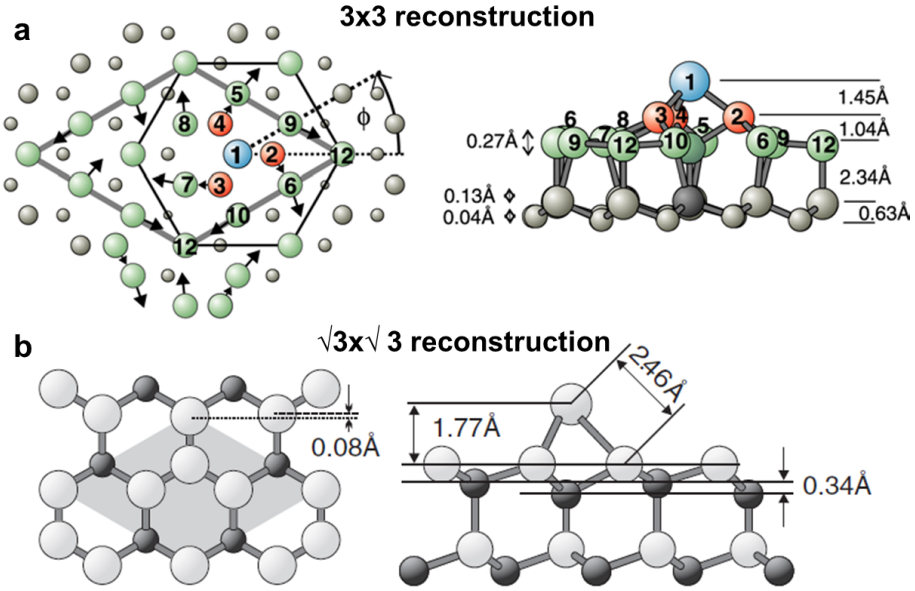

Figure 2.3: a) Top and side view model of the 3×3 reconstruction. b) Top and side model of the crystallographic structure of $\sqrt{3} \times \sqrt{3}R30°$ reconstruction. Taken from [66].

are already arranged in the graphene-like honeycomb layer, which is, however, strongly buckled due to covalent bonding with the SiC [77]. As a result of the buckling this layer does not have unique electronic properties of graphene [58]. In the scientific literature the q-$6\sqrt{3}$ phase is called "*buffer layer*" (BL) or the "*zero-layer graphene*".

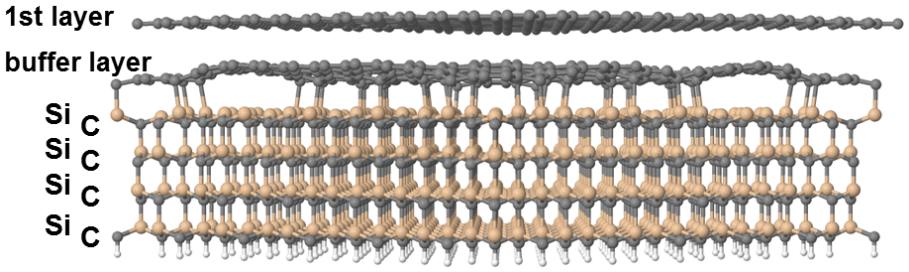

Figure 2.4: The fully relaxed DFT model of single layer graphene/BL/4H-SiC(0001) system. This image was taken from [78]

Recently, an extensive DFT calculations of the graphene/BL/SiC(0001) system were performed by P. Merino *et al.* [78]. The fully relaxed DFT model of the BL on top of the 4H-SiC(0001) substrate applied in their work is presented in Figure 2.4. Within this model the SiC slab is capped by a buckled graphene-like honeycomb carbon atom mesh. The peak-to-peak corrugation of BL was found to be 1.1 Å. Such a strong corrugation arises from the covalent bonding between some C atoms in BL and Si atoms in the outermost SiC layer. Since not all the substrate Si atoms are saturated by the C atoms in the BL, significant amount of the dangling bonds is present at the interface. Authors also find an excellent agreement between the simulated STM images of the single layer graphene and the experimental images. In particular, the typical localized features (i.e. subsurface dangling bonds) often observed experimentally are visible in their STM simulations.

The validity of the model described above is also supported by the ARPES studies of the BL carried by K. Emtsev and coworkers. It clearly document the existence of well developed graphene-like σ-bands [79]. This means that arrangement of atoms within BL is identical to those in graphene, i.e. BL consists of six-membered rings. Importantly, σ-bands are shifted towards a higher binding energies in comparison to graphite. This was explained by a significant charge transfer from the substrate. On the other hand, the π bands were found to be poorly developed. The BL exhibits nonmetallic character since it does not posses any states near the Fermi level. The ARPES data are evidence of a strong covalent coupling between at least part of the BL p_z orbitals and the underlying SiC substrate.

The influence of the substrate on the BL can be successfully removed by an in-

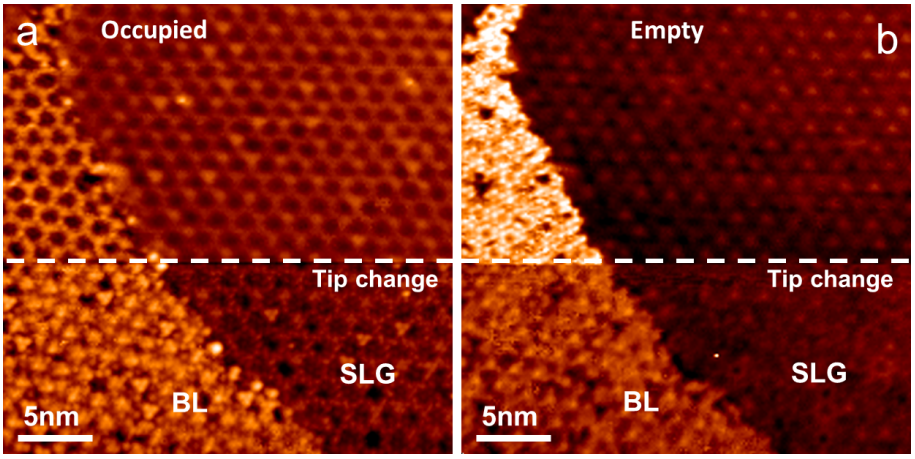

Figure 2.5: a) Occupied (-1.5 V, 0.23 nA) and b) Empty (+1.5 V, 0.23 nA) state STM image of the area containing the buffer layer (BL) and single-layer graphene (SLG). The white dashed line indicates the position of the accidental tip change and consequent changes in STM contrast over the BL and SLG.

tercalation of a suitable element, e.g hydrogen [80]. Such a hydrogen-intercalated BL is structurally and electronically identical to the truly freestanding graphene [81]. Recent studies also demonstrated that improved growth technique in Ar atmosphere allows preparation large scale BL areas with graphene-like Dirac cones separated by a small gap [82].

In contrast to the q-6$\sqrt{3}$ periodicity observed in the LEED studies, the STM and nc-AFM investigations of BL always reveal a corrugation pattern with quasi-periodic 6×6 reconstruction [83, 84]. The unit cell of this periodicity is indicated in the Figure 2.6a. The STM contrast observed over the q-6$\sqrt{3}$ is very complex and strongly depends on the scanning parameters and the tip structure. Thus, the exact determination of the BL structure only by means of STM is not feasible. In the Figure 2.5 we present an occupied (-1.5 V) and empty state (+1.5 V) constant current STM scans taken simultaneously in forward and backward channels, respectively over of the surface area containing the q-6$\sqrt{3}$ domain. The white dashed line marks a position of an unintentional change of the tip apex. Importantly, the bias voltages and current setpoint were kept constant through the scans. Prior to the tip change both occupied and empty state images share the same BL morphology and characteristic features. The tip change is accompanied by strong changes in the STM contrast. A well pronounced q-6 $\times$ 6 pattern appears in the occupied state image. At the same time, the empty state image reveals trimer-like pattern, which is related to the Si adatom dangling bonds [85].

Discrepancy in the different periodicities observed in LEED and STM experiments can be explained as following. The q-6$\sqrt{3}$ supercell is split into the areas where some C atoms or hexagon centers of BL are located directly above the substrate Si atoms as it is shown schematically on the Figure 2.6b. Such ar-

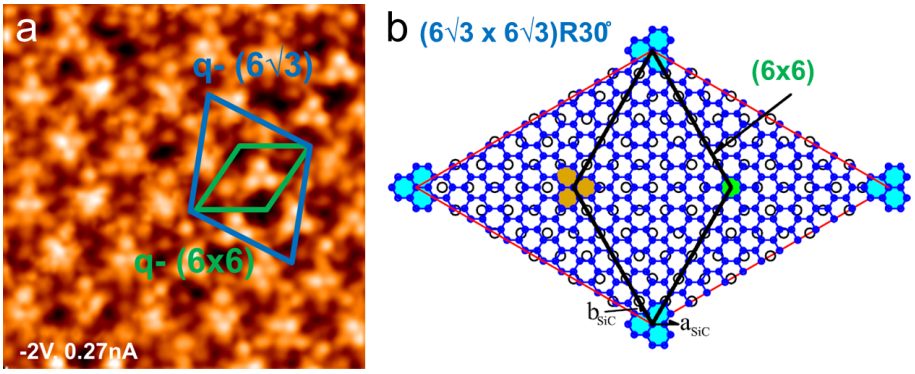

Figure 2.6: a) STM image of the BL area (10×10 nm^2). Green and blue rhombus marks a unit cell of the 6×6 and $6\sqrt{3}$ quasi-periodicity, respectively. b) Schematic image of the $6\sqrt{3}$ unit cell. Open circles are atoms in the SiC and filled circles are C atoms in the graphene layer. A q-6×6 unit cell connecting the high symmetry points is also shown. This image was taken from [10].

eas consequently appear as valleys of the q-6×6 modulation (see Figure 2.6a). Moreover, in the DFT model the q-$6\sqrt{3}$ periodicity arises spontaneously during relaxation [78]. Thus, the quasi-periodic 6×6 pattern seen in the STM arises from the larger commensurate q-$6\sqrt{3}$ periodic reconstruction.

2.1.4 Single and bilayer graphene

The BL serves as a precursor step towards formation of the single layer graphene (SLG). The annealing temperature over 1250°C is already sufficient enough to induce desorption of the Si from the BL/SiC(0001) interface and form the SLG [63]. During annealing the existing q-$6\sqrt{3}$ structure is transformed into the SLG and the outermost SiC bilayers are transformed into the BL. Thus, the interface BL remains always present between the SLG and SiC(0001).

The SiC(0001) annealing at the temperatures far above 1250°C leads to formation of the bilayer graphene (BLG). The BLG follows Bernal stacking (AB stacking) order similar for the graphite as was confirmed by the T. Ohta *et al.* [86]. Annealing at 1400°C results in the formation of multiple (over 3) graphene layers [87].

The structural properties of the graphene/SiC(0001) were extensively studied by means of nc-AFM [88, 89, 90] and STM [91, 92, 93]. The STM measurements of the SLG as well as BLG show a characteristic 6×6 quasi-periodic corrugation [94]. In the Figure 2.7, we present a set of STM images measured over an incomplete layer of graphene grown on the 6H-SiC(0001). The Figure 2.7a shows the main features of the surface morphology, terraces divided by steps of various heights, areas covered with SLG, BLG and areas of BL. The SLG and BLG areas might be distinguished by the lower apparent q-6×6 corrugation of the latter one. In the Figure 2.7b, we show an atomically resolved STM image of the

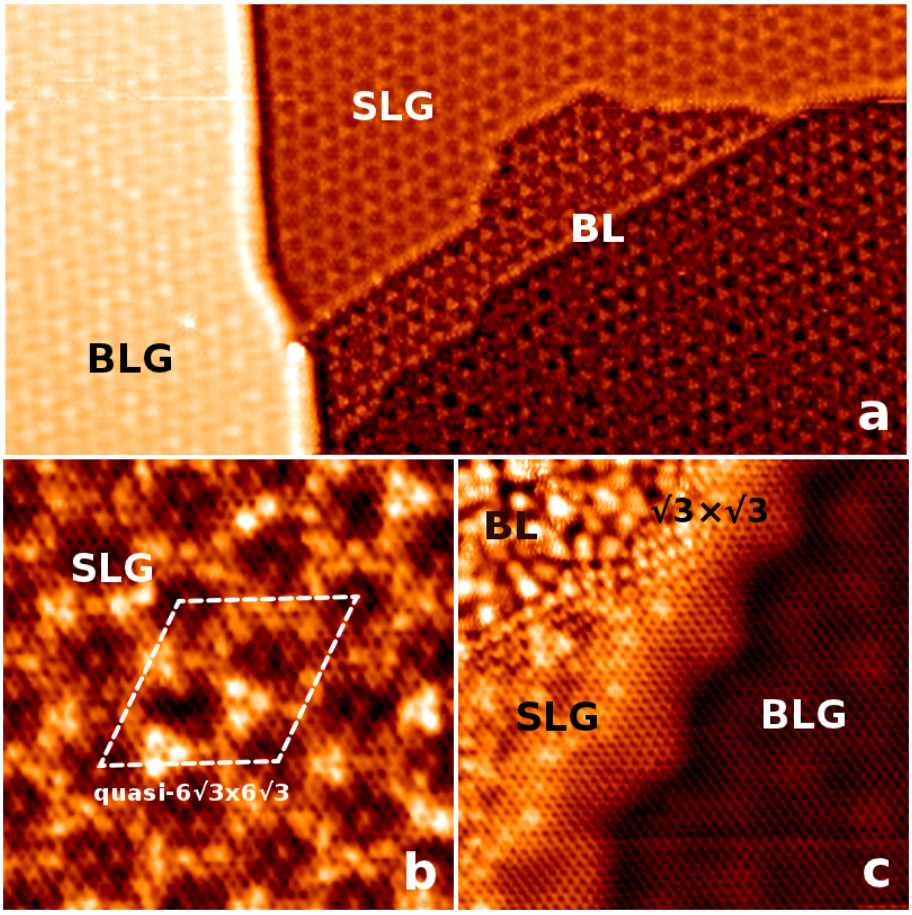

Figure 2.7: Constant-current STM images taken over an incomplete graphene layer grown on the 6H-SiC(0001). (a) 67×33 nm^2, V_{bias}=-1.5 V, I=0.15 nA; overview of an area containing the buffer layer (BL), single- and bilayer graphene (SLG and BLG). (b) 10 × 10 nm^2, V_{bias}=0.5 V, I=0.18nA; subsurface features bonds of the BL visible through a sheet of graphene, the characteristic q-6$\sqrt{3}$ quasi-periodicity is indicated. (c) 10 × 10 nm^2, V_{bias}=0.5 V, I=0.18 nA; example of a characteristic $\sqrt{3} \times \sqrt{3}$ rippling of SLG near to an armchair edge, step overgrown by graphene without any extra rippling. Published in [60].

single-layer graphene measured at the relatively low bias voltage (0.5 V). Here, a white rectangle indicates the unit cell of the characteristic q-6$\sqrt{3}$ quasiperiodicity. Additional round-shaped features observed here correspond to the substrate dangling bonds.

In spite of all the studies, it has not been clarified yet whether STM contrast, in particular the 6 × 6 modulation has electronic or topographic origin. The real physical corrugation of SLG and its contribution to the observed STM contrast is also not known. However, it is well known that the morphological modulations of the SLG and BLG arise from the interaction with the underlying BL [58, 77, 95].

2.1.5 Graphitization of SiC in UHV vs. Ar atmosphere

The representative STM image of the SiC(0001) graphitized in the UHV conditions is shown in the Figure 2.7a. The surface typically contains terraces of the BL, SLG and BLG. The BL fraction might be decreased by applying of the repeated annealing cycles. However, the average terrace width of SLG and BLG regions reaches typically only 50-100 nm.

Alternatively, the graphitization process can be performed in the atmosphere of Ar. This method was first proposed by Virojanadara *et al.* who annealed the SiC(0001) at 2000°C in a 1 bar of Ar environment. The authors observed formation of the homogenous large area single-layer graphene films ($> 1\mu$m) [96]. Later, K. Emtsev *et al.* obtained samples with average size of graphene domains of 2-3 μm using annealing temperatures 1500-2000°C and 900 mbar of Ar atmosphere [97].

The role of Ar in the annealing process can be understood as following. The Ar acts as a diffusion barrier and drastically decreases the sublimation rate of the Si. By this, increased Si vapor pressure is created close to the surface, hence much higher annealing temperature (over 1500°C) can be applied. This extremely high annealing temperature leads to the enhancements of surface diffusion. Consequently this leads to significantly higher sample homogeneity and much larger graphene domains in comparison to those obtained by the UHV annealing.

T. Ohta *et al.* studied the Si sublimation from the SiC(0001) sample covered by BL, which was prepared in the Ar atmosphere [98]. They proved that growth of high-quality SLG is initiated from etching the preexisting triple bilayer SiC steps. Thus, the preparation of the best quality graphene requires BL-covered sample with minimal number of single SiC bilayer steps on the BL surface.

2.1.6 Open questions and approaches to their solution

It is evident that many questions related to the characteristic reconstructions on SiC(0001) and its graphitization dynamics remain unresolved. We would like to address the following problems and our approaches for their solution:

- From the LEED, XPS and STM studies it is well known that upon annealing at 1050°C the Si-rich $\sqrt{3} \times \sqrt{3}$ is transformed into the C-rich BL with the q-$6\sqrt{3}$ reconstruction. On the other hand, the comprehensive atomically scale study of this transformation is still missing. To shed some light on this, we performed an atomically resolved STM investigation of the initial steps of the BL formation.

- During the annealing process, formation of the q-$5\sqrt{3}$ reconstruction competes with the growth of the BL phase, since both appear under the same

annealing conditions. This reconstruction has been poorly studied till now. Its origin as well as atomic arrangement still has to be understood. Here, by the analysis of the atomically resolved STM images and DFT calculations we develop an atomistic model of the q-$5\sqrt{3}$ phase.

- Due to the presence of the underlying BL, the SLG(BLG) layers exhibit the characteristic quasi-periodic 6×6 modulation when studied by STM. The understanding of this modulation is important due to its influence on the graphene electronic properties. The 6×6 pattern might have an electronic or topographic origin. So far, it has not been clarified because the separation of the electronic or topographic contributions in the STM contrast is not straightforward. To solve this, we performed nc-AFM/STM experiments with simultaneous access to tunneling current and frequency shift channel. By this we got access to the real physical corrugation of the SLG/SiC(0001).

- One of the significant limitations for the practical applications of the samples graphitized in the UHV conditions is a presence of the phase mixture (BL, SLG and BLG) on the surface. Moreover, the average size of graphene domains is typically only 50-100 nm. On the other hand, the SiC annealing in the Ar atmosphere is a promising route for the preparation samples with exclusive presence of the SLG. We present the experimental setup and protocol for the sample annealing in the Ar atmosphere developed in our group. Our approach allows preparation of a high-quality SLG/SiC(0001) sample with average size of terraces well over 1 μm.

2.2 Growth dynamics of buffer layer

In the following we focus on the formation and structure of the q-6$\sqrt{3}$ reconstruction. In particular, we study the transition from the Si-rich $\sqrt{3} \times \sqrt{3}R30°$ to the C-rich q-6$\sqrt{3}$ phase by means of the STM.

During our studies we used following scheme for the SiC(0001) annealing in the UHV:

1. Sample degassing at 650°C for 8 hours.

2. Sample annealing at 750-800°C under the Si flux for 15 min. As the source of the Si flux we used a Si wafer, which was annealed up to 1200°C by passing the direct current. The Si deposition rate approximately corresponded to 1ML per second. Typically we performed several Si evaporation and annealing cycles (15 min every) to obtain clean surface with large terraces.

3. A stepwise sample annealing up to 1200°C with 50°C temperature increments. The duration of one annealing step was 10 minutes.

In the Figure 2.8, we show a representative large-scale STM image of the surface after three Si sputtering cycles. The average terraces width is 50 nm and the surface is completely covered by the Si-rich 3 × 3 reconstruction.

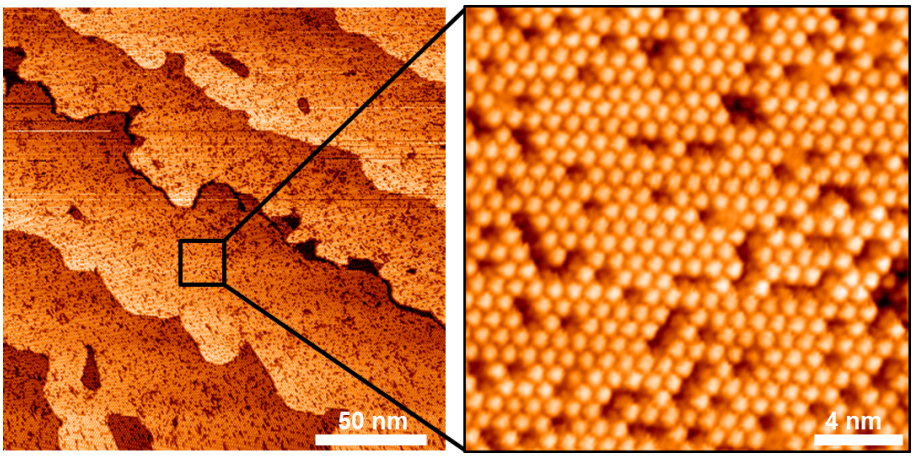

Figure 2.8: Large-scale STM image showing the overall morphology of the sample after the three 15 minute cycles of sample annealing at 750°C under the Si flux. The surface exhibits a 3 × 3 reconstruction.(V_{bias}=0.77 V, I=0.1 nA)

The stepwise sample annealing up to 1000°C typically results in a surface which contains a few different phases, as shown in Figure 2.9a. The three different coexisting reconstructions are: q-6$\sqrt{3}$, $\sqrt{3} \times \sqrt{3}R30°$ and q-5$\sqrt{3}$. Here the BL domains with the q-6$\sqrt{3}$ periodicity are coexisting with the Si-rich $\sqrt{3} \times \sqrt{3}R30°$ phase which is prevailing on the sample. Figure 2.10 represents an atomically resolved STM images obtained on the same surface. The images clearly reveal

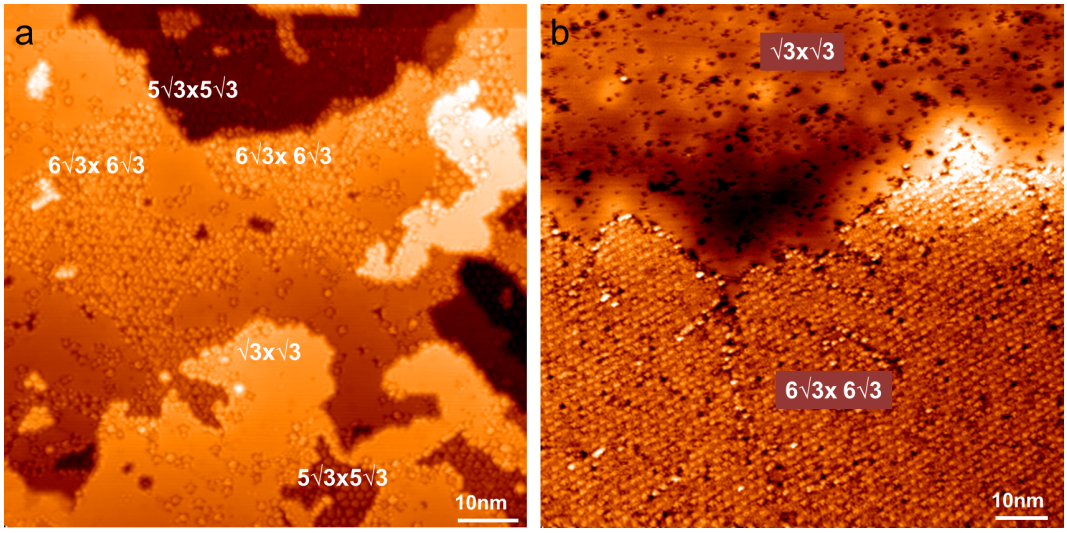

Figure 2.9: a) Large-scale constant current STM image showing the coexistence of the three different phases: q-$6\sqrt{3}$, $\sqrt{3} \times \sqrt{3}R30°$ and q-$5\sqrt{3}$ b) Large-scale constant current STM image showing coexistence of two domains of q-$6\sqrt{3}$ and $\sqrt{3} \times \sqrt{3}R30°$ reconstructions. The surface was obtained by stepwise sample annealing up to 1000°C. b) constant current STM image showing the presence of the developed areas of the BL, which were prepared by the stepwise sample annealing up to 1050°C.

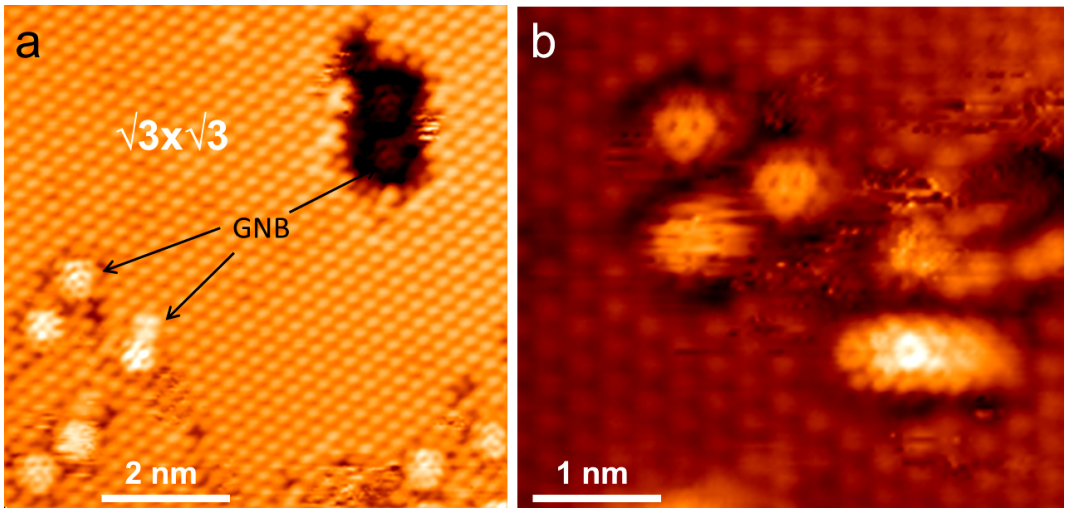

Figure 2.10: STM images showing the graphene nanobubbles (GNB) embedded into the $\sqrt{3} \times \sqrt{3}R30°$ reconstruction. Scanning parameters are: V_{bias}=-2.5 V, I=0.1 nA for both images.

the presence of the $\sqrt{3}\times\sqrt{3}R30°$ phase with inclusions of distinct features. Closer inspection shows round objects with the graphene-like STM pattern (see Figure 2.10b). Hence, we assign this formations to graphene nanobubbles (GNB).

The sample annealing at slightly higher temperatures 1050-1100°C results in significantly larger (up to 50nm) BL domains (see Figure 2.9b). A further annealing over 1150°C produces sample with almost full coverage of the BL phase. We infer that sample annealing at these temperature causes merging of separate GNB and consequent developing of the complete BL domains. To the best of our knowledge the formation of GNB has not been reported yet.

2.3 $5\sqrt{3} \times 5\sqrt{3}$ reconstruction

The growth of BL is always accompanied by the formation of the q-$5\sqrt{3}$ reconstruction. Moreover, our STM observations indicate that significant amount of the q-$5\sqrt{3}$ reconstruction is preserved on the surface even after high temperature annealing (over 1200°C). Often the q-$5\sqrt{3}$ coexists with the SLG, BLG areas and sometimes is also seen under the SLG.

When studied with STM, the domains of the q-$5\sqrt{3}$ are often found to be incorporated into the prevailing q-$6\sqrt{3}$ as we show in the Figure 2.11a. The atomically resolved STM image of the q-$5\sqrt{3}$ is presented in the Figure 2.11b. The reconstruction is comprised of the clusters having 2-7 protrusions, that most likely correspond to the dangling bonds of the Si adatoms.

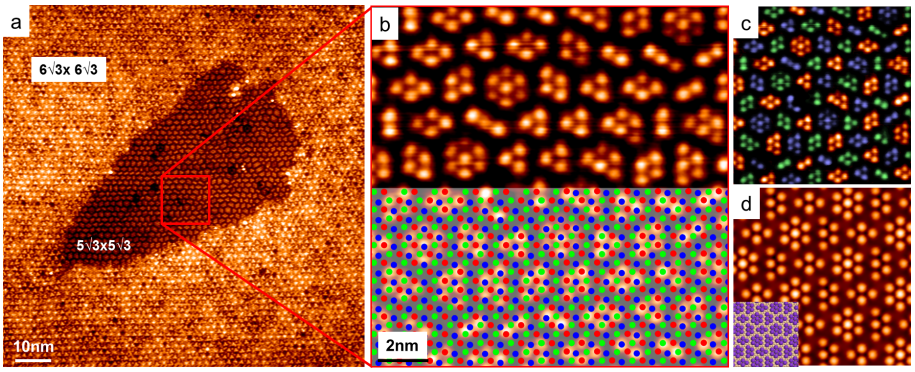

Figure 2.11: a) Large-scale constant current STM image showing the coexistence of the two different phases q-$6\sqrt{3}$ and q-$5\sqrt{3}$ (V_{bias}=-1.5 V, I=0.15 nA). b) Magnified region of q-$5\sqrt{3}$ phase only. The lower part of the image is overlayed by grid formed by three different $\sqrt{3} \times \sqrt{3}$ sublattices (blue, green and red). c) The image b) showing assignment of every surface adatom to one of three $\sqrt{3} \times \sqrt{3}$ sublattices. d) The simulated STM image of the q-$5\sqrt{3}$ reconstruction.

The bottom part of the image is overlayed by the 1×1 grid formed by the three different $\sqrt{3} \times \sqrt{3}$ sublattices (red, green, blue). It can be seen that every surface adatom of the q-$5\sqrt{3}$ structure can be unambiguously assigned to one

of these three sublattices as indicated in Figure 2.11c with corresponding colors. In addition, within every island all the adatoms belong to the same $\sqrt{3} \times \sqrt{3}$ sublattice. In the light of this, every cluster then represents a separate domain of the possible $\sqrt{3} \times \sqrt{3}$ sublattice.

We constructed a unit cell consisting of clusters of Si adatoms in T4 positions, each in different $\sqrt{3}$ domain. We then simulated STM images of the q-$5\sqrt{3}$ reconstruction, which are presented in the Figure 2.11d. We find excellent agreement between the experimental and theoretical STM images.

2.4 Structure of graphene/SiC(0001)

The materials of this Section were published in [60].

To shed light on the origin of the 6×6 modulations we performed combined nc-AFM/STM studies using a Q-plus sensor. Using the Q-plus setup we performed the measurements on the SLG/SiC(0001). The Q-plus allows simultaneous access to the current (I_t) and the frequency shift channels (Δf). Thus, we were able to separate electronic and topographic contribution to the nc-AFM/STM contrast.

The current and frequency shift channels were acquired simultaneously in the constant height mode over the same area of graphene. However, we had to apply very small tunneling current feedback. The reason to use the $< I_t >$ channel for the feedback is a possibility carry out measurements at very small tip-sample distances in the region of negative frequency shift gradient. In this region Δf feedback would be unstable.

The set of curves in Figure 2.13a represents local spectroscopy taken just before the imaging above the SLG with the Q-plus sensor, oscillating at amplitudes of 150 pm at room temperature. The Δf, time-averaged current ($\langle I_t \rangle$) are measured vs. the tip-sample relative distance (Z) during an approach and retraction of the tip. Voltage is kept at 100 mV. The $\langle I_t \rangle$ grows exponentially with Z and the Δf has a minimum near to -80 Hz. The value of $Z = 0$ corresponds to the tip-sample separation at $\langle I_t \rangle$ setpoint of 0.46 nA. In the region of the set point, the Δf is rising at a rate of (0.98$\pm$0.04) Hz/pm, as determined by the least-square fitting. Force (F) is calculated from the Δf signal, using the approach proposed by J. Sader *et al.* [39]. The maximum attractive force amounts roughly to -0.3 nN.

The both measured channels are shown in the Figure 2.12. The characteristic q-$6\sqrt{3}$ modulation of graphene is visible in both channels. From the Δf image we estimated the Z-height modulation of graphene and obtain a value of about 6 pm root-mean square (RMS) corresponding to 16 pm peak-to-peak corrugation. This value is significantly lower than the roughness obtained by the standard topographic mode of STM (21 pm RMS or 60 pm peak-to-peak). Therefore, elec-

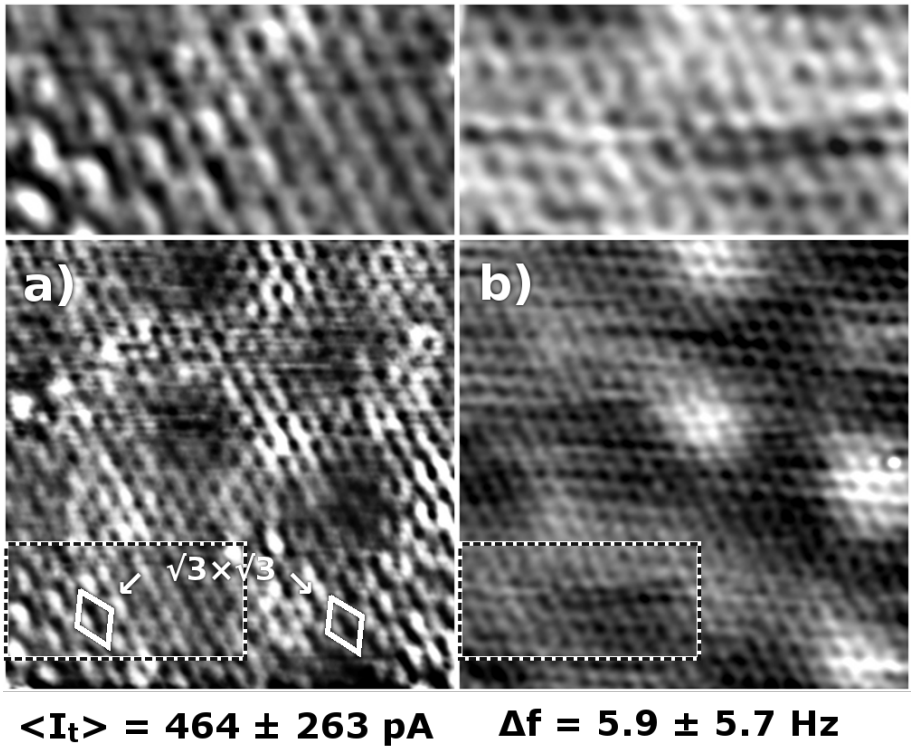

Figure 2.12: (a) The average tunneling current $\langle I_t \rangle$ maps (V_{bias}=100 mV, I=0.46nA, 5.5 nm×7.1 nm and (b) frequency shift Δf acquired on the same area of graphene/SiC(0001). The q-$6\sqrt{3}$ modulation is apparent in both channels, whereas the $\sqrt{3} \times \sqrt{3}$ modulation due to scattering on armchair boundary is detected only in the $\langle I_t \rangle$ map. The insets on the top show zoomed images of a region that has a $\sqrt{3} \times \sqrt{3}$ modulation in the $\langle I_t \rangle$ map. The mean value and a standard deviation (RMS) are given for each measured quantity beneath each of the images.

tronic contribution of the BL to the STM topography of SLG must be dominant.

To identify any charge transfer effects within the q-$6\sqrt{3}$ structure of graphene a Kelvin-probe measurement [99] has been performed on the bright and dark areas (highs and lows of the q-$6\sqrt{3}$ modulation) in the Δf image, at 0.5 nm from the setpoint, further from the sample. In the Figure 2.13b, the two corresponding parabolas show no difference neither in the shape nor in their maxima. The contact potential between the tip and the sample corresponds to maxima in the parabolas and is located at -0.32 eV.

Considering that the electronic contribution is the major factor that affects the $\langle I_t \rangle$ maps, we can also deduce that these maps taken at low bias reflect a variation of the local conductivity. Moreover, the Kelvin parabola measurements do not detect any significant contact potential difference between the dark and bright protrusions of the q-$6\sqrt{3}$ modulation. It can be understood as a negligible work function difference between these investigated areas.

To support our experimental observations we performed large scale total en-

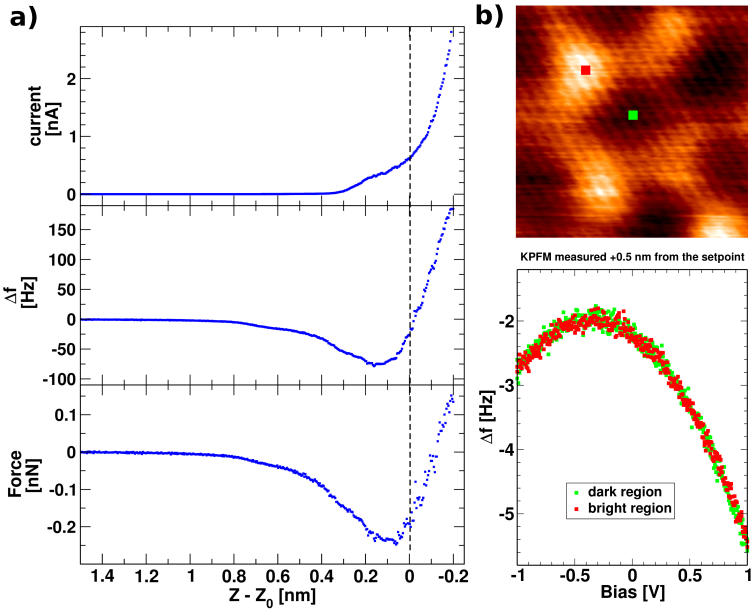

Figure 2.13: (Color online) (a) Spectroscopy curves of average tunneling current $\langle I_t \rangle$, Δf and force F vs. the tip-sample distance on graphene/SiC(0001), taken with a bias voltage of 100 mV, just before imaging. The value of $Z = 0$ corresponds to the tip-sample separation at $\langle I_t \rangle$ setpoint of 0.46 nA. (b) Example measurements of the local potential at bright and dark regions of the q-$(6\sqrt{3})$ modulation visible in the Δf map, indicating undetectable charge transfer.

ergy density functional theory (DFT) calculations. The fully relaxed theoretical model of SLG on the BL using the $6\sqrt{3}\times 6\sqrt{3}$R30° unit cell is shown in the Figure 2.14. The calculations show that standard deviation of the C atom z-positions in the SLG layer is 4.4 pm (12.4 pm peak-to-peak). This agrees well with the experimental estimation (16 pm peak-to-peak) from the Δf image. This value is also comparable to a similar DFT calculation in [81]. Noteworthy, this value is significantly smaller than the corrugation obtained for graphene/Ru(0001) and graphene/Ir(111). The corrugations of the both of these systems are claimed to be in the range of 100 pm (corresponding to 35 pm RMS) [100, 101, 102].

In the next, we focus on the boundaries residing in the left and right lower corners of the image Figure 2.12a. These boundaries produce the characteristic $\sqrt{3} \times \sqrt{3}$ modulation on graphene visible in the $< I_t >$ channel (see inset of Figure 2.12a). This modulation was explained in terms of the intervalley scattering mechanism of electrons in graphene [91]. Whereas, the Δf image shows only a flat honeycomb structure of graphene. We do not observe any out-of-plane relaxation of the carbon atoms in the honeycomb structure resolved by nc-AFM (see inset of Figure 2.12b). This is a clear evidence that the $\sqrt{3} \times \sqrt{3}$ modulation visible in the $< I_t >$ has purely electronic origin. It also demonstrates that the graphene layer in SLG is weakly bound to the BL through van der Waals interactions. This finding of no atomic relaxations can be extrapolated for the

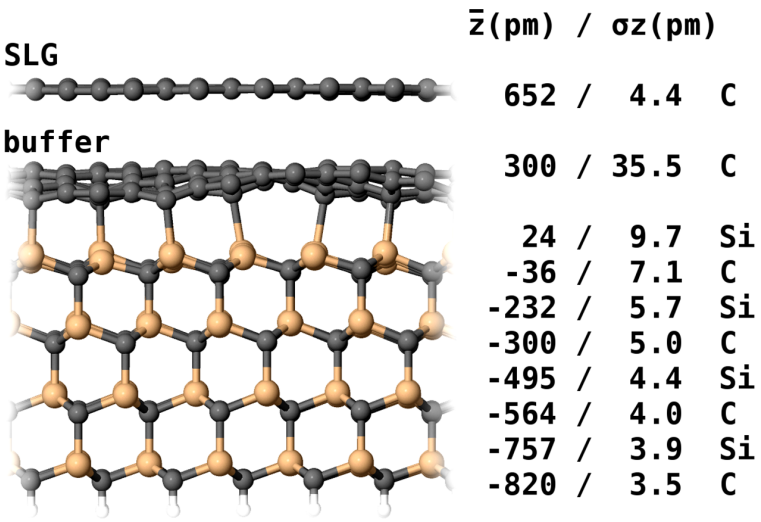

Figure 2.14: The fully relaxed theoretical model of SLG on the BL, that is using the $6\sqrt{3}\times6\sqrt{3}$R30° unit cell. The z values in the table correspond to z-positions of C and Si atomic layers in the model, σz is a standard deviation of atom positions. The standard deviation of the C atom z-positions in the SLG layer is 4.4 pm.

single-point defects and other graphene disruptions for graphene on SiC(0001), since they produce the same type of scattering and do not interact strongly with the substrate.

In conclusion, we performed an atomic scale study of the SLG/SiC(0001) system using the Q-plus setup. Simultaneous nc-AFM/STM measurements show that the 6×6 modulation observed in the STM has both the electronic and topographic contribution. However, the contribution of the electronic component is significantly higher than the topographic one. Moreover our experiments prove that the characteristic $\sqrt{3}$ rippling of graphene, which appears due to presence of the defects or boundaries is not accompanied by any relaxations of carbon atoms and has purely electronic origin.

2.5 Reactor for SiC graphitization in Ar

One of general issues during the SiC annealing in Ar is reaching the extremely high temperature ($\approx$ 1600°C). Typically, it is achieved in an inductively heated furnace [96] or quartz glass rectors [97]. In our group we developed an alternative type of reactor for the sample annealing in the Ar environment (see Figure 2.15). Basic idea is the following, the sample is heated by a direct contact with the supporting SiC wafer which is annealed by passing the DC current. Noteworthy, our setup allows to overcome a problem of Ar gas ionisation, which is common for the furnaces with RF heating.

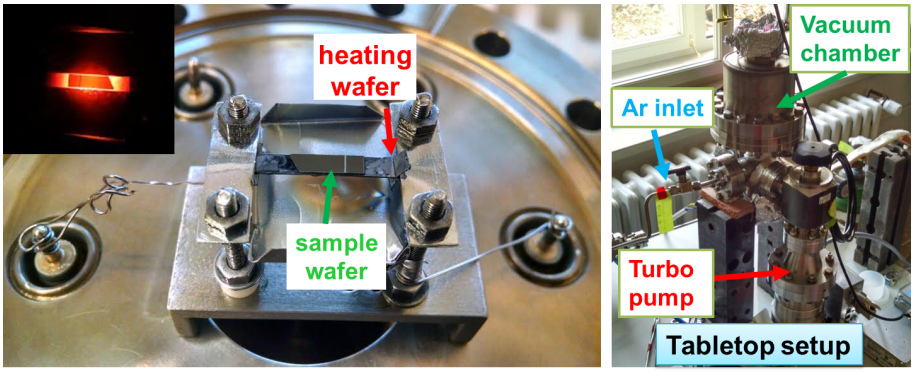

Figure 2.15: Picture of the experimental setup for the annealing of SiC wafers in the Ar atmosphere. The sample is heated by the direct contact with the other SiC wafer annealed by passing the direct current.

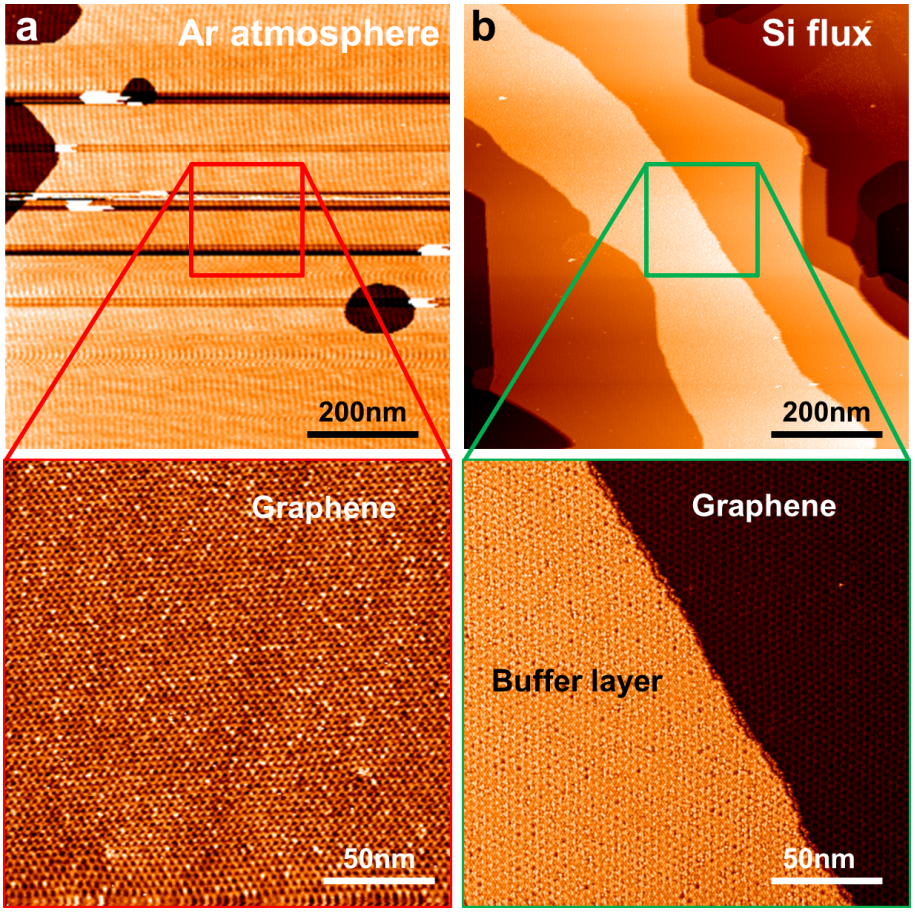

Figure 2.16: Large-scale STM images showing the overall morphology of graphene samples prepared a) in the UHV conditions using the Si flux b) in the 900 mbar Ar atmosphere and 1600°C annealing.

We used the following protocol for the graphene/SiC(0001) sample preparation:

1. The sample degassing in the UHV pressure better than 1×10^{-9} mbar for the 2 hours.

2. Two cycles of the sample annealing at 1400°C and 1500°C for 10 minutes each in a 0.9 bar of Ar atmosphere. The Ar was evacuated and reintroduced into the chamber after every annealing cycle.

3. The sample annealing at 1600°C in 0.9 bar of Ar for 3 minutes followed by a slow temperature decrease ($\approx$ 100°C per minute) to prevent the SiC cracking.

The large-scale STM image of the SLG/SiC(0001) which was grown using this annealing scheme is shown in the Figure 2.16a. The resulting surface is exclusively covered with high-quality SLG sheet. The average width of terraces is 1 μm in contrast to the graphene grown in UHV (see Figure 2.16b). Moreover, the STM image clearly reveals the characteristic q-6×6 modulation pointing out presence of BL in the interface of SLG/SiC(0001) similarly to the sample prepared in the UHV conditions.

2.6 Conclusions

We performed an STM study of the initial steps of the SiC(0001) graphitization process. For the first time, we follow the growth of the BL at the atomic level. We show that BL growth is initiated by the formation of the Si depleted regions - graphene nanobubbles incorporated into the $\sqrt{3} \times \sqrt{3}$ phase. The sample annealing at higher temperatures results in the merging of separate graphene nanobubbles and formation of the well-developed q-$6\sqrt{3}$ BL phase.

Next, we proposed an atomistic model of the q-$5\sqrt{3}$ reconstruction. Within this model every cluster of the q-$5\sqrt{3}$ represents separate domain of the one of three possible $\sqrt{3} \times \sqrt{3}$ sublattices.

In addition, we successfully probed the epitaxial graphene on SiC(0001) by a combined nc-AFM/STM technique, gathering extended information on its atomic structure near defects. By atomic force microscopy, we detected a topographical corrugation of the q-$6\sqrt{3}$ with an average value of 6 pm RMS (16 pm peak-to-peak). We can conclude that corrugation exceeding 40 pm detected by previous STM measurements was caused mainly by electronic contributions arising from the BL. In the case of the characteristic $\sqrt{3}$ rippling of graphene, which occurs due to presence of defects or boundaries, any relaxations of carbon atoms perpendicular to the surface can be excluded. These results are consistent with a

recent findings and show the SLG on SiC(0001) as a morphologically very flat substrate.

Finally, we developed the simple but very efficient experimental setup and the annealing protocol allowing preparation SLG/SiC samples in the Ar atmosphere. The average size of the SLG terraces exceeds 1 μm. Such graphene layers might be already suitable for the applications in the electronic devices.

3. Modifying of graphene electronic structure

Some materials of this Chapter were published in three papers [103, 104, 105].

3.1 Electronic properties of graphene/SiC

In the following we review the basic electronic properties of the SLG/SiC(0001) and main approaches for their engineering. The SLG epitaxially grown on the SiC(0001) is intrinsically n-doped due to the charge transfer from the substrate [58]. This results in a downward shift of the Dirac point with respect to the Fermi level. As seen from the Figure 3.1a an ARPES spectra measured over the SLG exhibits the Dirac point which is located 0.35 eV below the Fermi level. This corresponds to the charge excess of $1.1 \times 10^{13} cm^{-2}$ [12]. The doping effect does not depend on a preparation procedure and substrate polytype. According to the theoretical work of Kopylov *et al.* [106] the charge transfer in SLG might arise due to charge donation from the bulk donors or from the states in the SiC surface. The most probably it is related to high density of dangling bonds protruding from the SiC(0001) substrate.

In the Figure 3.1b we present typical STS spectrum measured over the SLG. The spectrum shows characteristic linear DOS with two characteristic depressions at zero bias and near −350 mV. The dip at −350 mV is associated to the Dirac point, which is shifted with respect to the Fermi level, similarly to the ARPES spectra. The second dip at the zero bias voltage has been explained in terms of the electron-phonon coupling and missing excitation of the phonon mode in graphene that can enhance the tunneling current [107].

As it was already mentioned, the graphene can be also grown on the C face SiC(000$\bar{1}$) substrate. The multiple graphene layers grown on this face are rotated with respect to each other [108]. This prevents a charge transfer from the substrate. Therefore, the outermost graphene layers are completely electronically decoupled from the SiC substrate [58]. On the other hand, the rotations between layers affect their electronic structure. For example, it produces the van Hove singularities in the LDOS spectra [109] or induces appearance of so-called moire bands [110].

One approach to remove the intrinsic doping of the SLG on SiC(0001) is a hydrogen (H) intercalation [111]. The intercalated H saturates the dangling bonds at the BL/SiC(0001) interface and thus produces SLG which is electronically decoupled from the substrate. In the literature, such a H intercalated

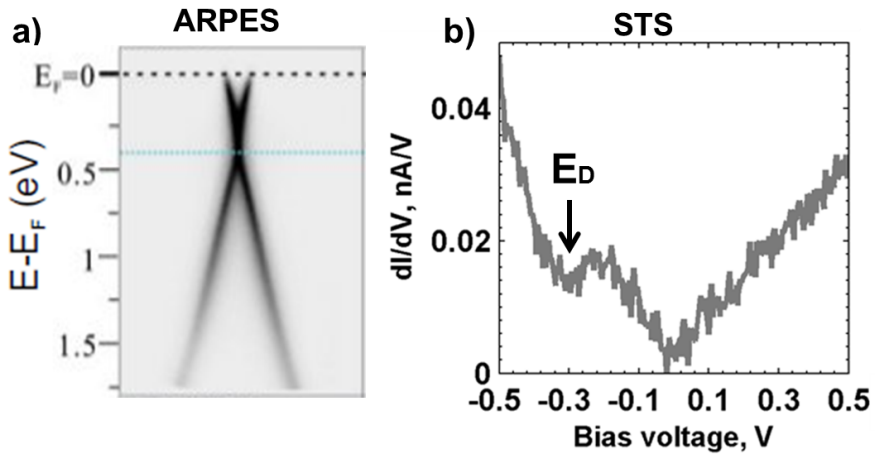

Figure 3.1: a) ARPES spectra at the K point measured over single layer graphene/SiC(0001). The Dirac point is located at -0.35eV below the Fermi level (from [12]). b) Experimental STS spectra taken over the graphene/SiC(0001).

graphene is often called a "*quasi-free-standing monolayer graphene*" (QFMLG). In the Section 3.3.4 we apply the H intercalation procedure to prepare the B doped QFMLG.

Graphene/SiC(0001) exhibits a high electronic mobility at the Fermi level $\sim$ 1200 $cm^2V^{-1}s^{-1}$ at low temperatures as it was reported by Berger and colleagues [15]. Indeed, this value is much lower than one reported for the free-standing graphene ($\sim$ 10000 $cm^2V^{-1}s^{-1}$) [2]. The QFMLG has a higher mobility ($\sim$ 3000 $cm^2V^{-1}s^{-1}$) in comparison to SLG. In this case, the main factor limiting the electron mobility is the incomplete H intercalation [112]. Recent magnetoresistance experiments have showed that complete H intercalation might result in significantly higher values of the electron mobilities $\approx$ 11000 $cm^2V^{-1}s^{-1}$ at 0.3 K [113].

Alternative way to tune the graphene electronic structure is a covalent functionalization by adsorption of the specific atoms or molecules. For example, studies of D. Elias *et al.* demonstrated the possibility of a bandgap opening by adsorption of the atomic H [114]. Similar results were achieved by graphene fluorination (adsorption of the single F adatoms) as was shown by R. Nair *et al.* [115]. The position of the Dirac point with respect to the Fermi level can be further tuned by the intercalation of the suitable species, e.g. O [116], Li [117, 118], Au [119, 120], F [121, 122], Ge [123] or adsorption of the metals Bi, Sb, Au [124, 120]. The sign of the Dirac point shift depends on the electronegativity of the intercalated elements.

The charge carriers density in graphene can be also controlled by adsorption of donor or acceptor molecules. For example, $C_{60}F_{48}$ and $F4-TCNQ$ molecules act as strong electron acceptors when adsorbed on SLG/SiC(0001) [125, 126]. Since these molecules tend to pull the electrons from graphene, the charge transfer from

the SiC substrate can be effectively compensated. Depending on the coverage of deposited molecules, the graphene doping can be changed from original n-type to the p-type.

The magnetic properties of graphene were mainly exploited by interaction with metals possessing the nonzero magnetic moment, e.g. adatoms of transition metals Fe, Ni, Co [127, 128] or the intercalated metals, e.g. Fe [129], Co [130].

Recent theoretical and experimental studies have demonstrated enhanced electron-phonon coupling and consequently the superconductive properties of SLG/SiC(0001) decorated by alkali atoms, e.g. Li [131, 132].

Substitutional B-, N doping is a promising path to engineer a graphene band gap. For graphene epitaxially grown on metallic substrates, doping is commonly achieved by a CVD method [8]. The dopant concentration can be controlled by adding gaseous precursors that contain the dopant during graphene growth [133, 134, 135, 136, 137]. This method was applied for the preparation of BN-co-doped graphene as well [22, 138]. Similar strategy has been also successful for N doping of graphene grown on SiC substrates, by exposing the substrate to N_2 gas during the growth procedure [139]. An alternative doping method by ion implantation, which allows a better concentration control and purity of N doping, was recently demonstrated [140, 141, 142, 143, 144, 145].

3.2 N doped graphene

3.2.1 N doping method

Figure 3.2 shows a scheme of the preparation method which we employed to achieve the N doping of graphene. According to our approach the SLG and BLG graphene on SiC(0001) is exposed to the flux of the 100 eV N^+ ions. In the next step, the surface is stabilized by the thermal annealing at 1200 °C.

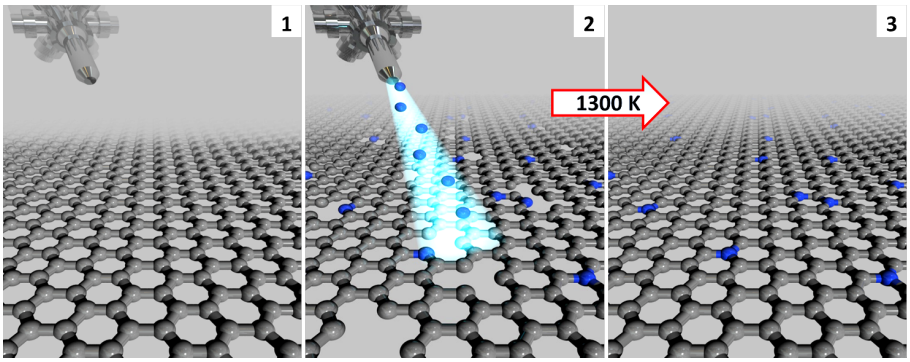

Figure 3.2: Scheme of the preparation procedure of N doped graphene on the SiC(0001) substrate. Gray and blue colors correspond to C and N atoms, respectively.

The unstabilized surface just after ion bombardment is typically damaged and contaminated, therefore it is not suitable for STM measurements. However, it gets completely recovered after the high-temperature annealing. Figure 3.3a shows a representative large-scale STM image of the graphene on 6H-SiC(0001) after the N^+ ion bombardment and the thermal stabilization. The graphene layer is decorated by randomly distributed triangle-shaped objects that are present in two basic orientations with respect to the graphene lattice. The two orientations of the triangular dopants are due to the locations of the substitutional N atoms in one of the two graphene sublattices (A or B) as depicted schematically in the Figure 3.4. The Figure 3.3b shows the STM image with higher concentration of the N dopants which can be achieved by tuning the duration of the bombardment time or the intensity of the N^+ ion flux.

We would like to note, that our doping method can be also applied to produce N doped QFMLG/SiC(0001) as it was demonstrated recently by J. Sforzini and coworkers [146].

3.2.2 STM on individual N dopants

Numerous sessions of atomically-resolved imaging in both constant-height and constant-current modes have demonstrated that the STM contrast on the N dopants usually results in one of two characteristic patterns. Figure 3.5 shows

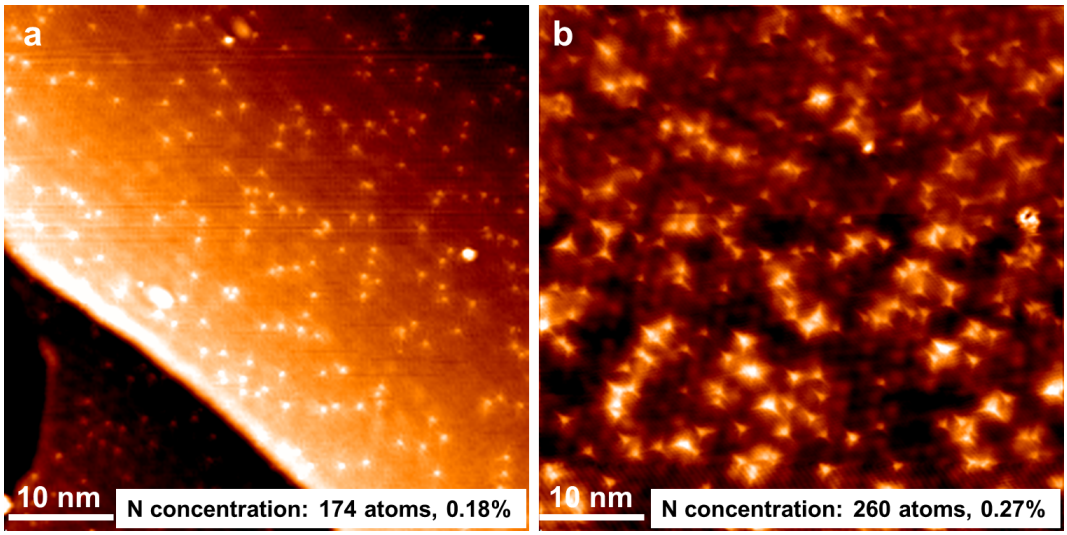

Figure 3.3: Large-scale constant current STM scans (50×50 nm^2) of the two samples with different concentrations a) 0.18% and b) 0.27%) of the N dopants in the graphene/SiC(0001). The sample with higher concentration was produced by increased time of the N^+ ion bombardment. Scanning parameters are: a) V_{bias}=0.7 V, I=0.1 nA and b) V_{bias}=-0.5 V, I=0.15 nA.

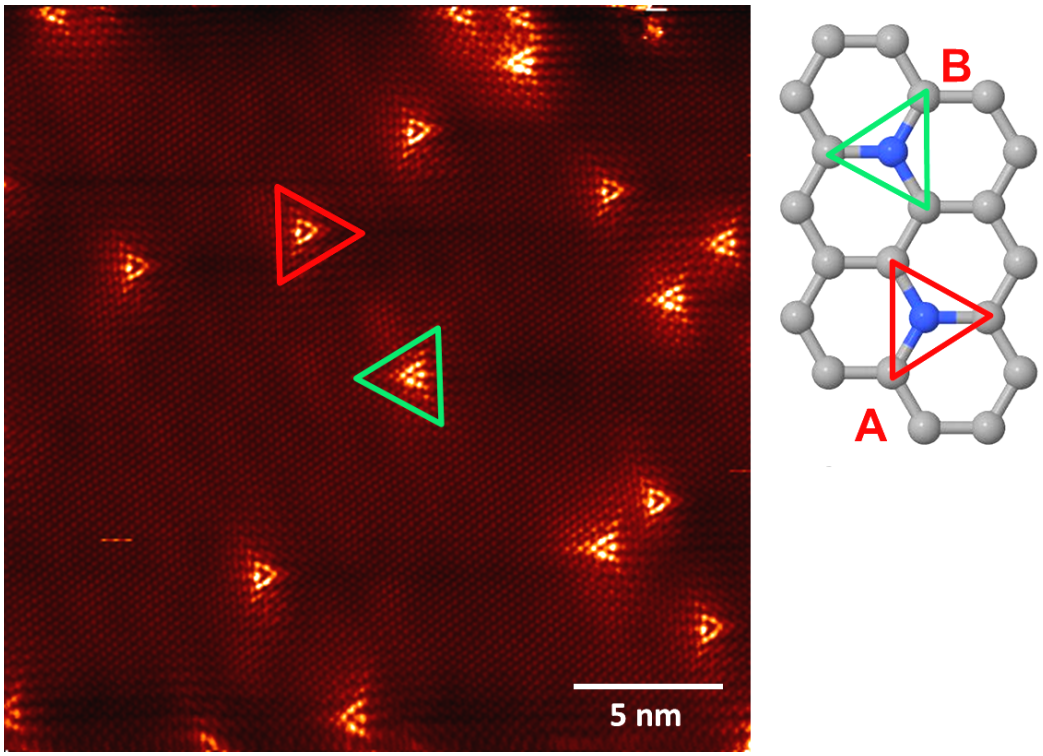

Figure 3.4: Constant height STM image of the N doped graphene/SiC(0001) (V_{bias}=0.3 V, I=0.18 nA, 25×25 nm^2). Red and green triangles mark the single N dopants located in the different graphene sublattices.

an equal-scale comparison of these two most frequently observed contrast types. Figure 3.5a displays N dopants that appear as hollow triangles. Each triangle is composed of six protrusions, which correspond to the six carbon neighbors surrounding the N dopant. This type of contrast is very similar to the one observed previously [140]. On the other hand, Figure 3.5b shows an equivalent type of single N dopants imaged as triangles composed of only three protrusions, which are packed closely together. These three protrusions coincide with the three nearest neighbor carbon atoms to the dopant. Since the graphene lattice is well discernible in the vicinity of the dopants, it is possible to overlay the honeycomb graphene lattice over both current maps of the two contrast types (insets of the Figure 3.5a,b). It helps to identify the atomic structure and correspondence of the tunneling current maxima around the dopants to the lattice positions. Both STM patterns were observed on SLG and BLG layers. Noteworthy, the dual STM contrast is not voltage dependent since both images were taken with the same bias voltage (-0.4 V).

In the Figure 3.6 we compare experimental images for the hollow-triangle contrast with STM simulations performed for the C(111) tip model and tip-surface distance 3.5 Å. We find an excellent agreement for both empty and filled states. The origin of the full-triangle STM contrast will be discussed in detail and explained in terms of the destructive interference effect in the Section 3.4.3.

As mentioned above, the N^+ ion implantation into the graphene lattice can be done progressively. Figure 3.7 shows atomically-resolved STM image of a sample doped with a higher amount of N dopants. This sample was produced by an extended ion irradiation followed by a high-temperature annealing of the sample. The concentration of the N dopants is $\approx 0.13\%$, and a new type of structure emerges. This new structure has only one axis of mirror symmetry. On the other hand, the single N dopant has three. Moreover, it is presented in six different orientations on the surface. An overlay of the graphene lattice (the inset of the Figure 3.7a) suggests a possible atomic structure for this feature, that is, a pair of substitutional N atoms in the second-nearest neighbor configuration within the graphene lattice (meta configuration).

We simulated the current maps using the C(111) tip for the two N dopants in ortho, meta and para configurations (see Figure 3.8) and compared our results to the experimental current maps. We find the best agreement between the experimental and simulated STM images for the meta structure (Figures 3.7b-c).

The meta dopants represent $\approx 10\%$ of the total amount of dopants. We find only negligible amount of dopants in ortho and para configuration. This result is surprising since DFT calculations clearly yield the para configuration as the most energetically favourable (see Table 3.1). Meta configuration has 0.345 eV higher formation energy than para configuration. Ortho configuration is even less

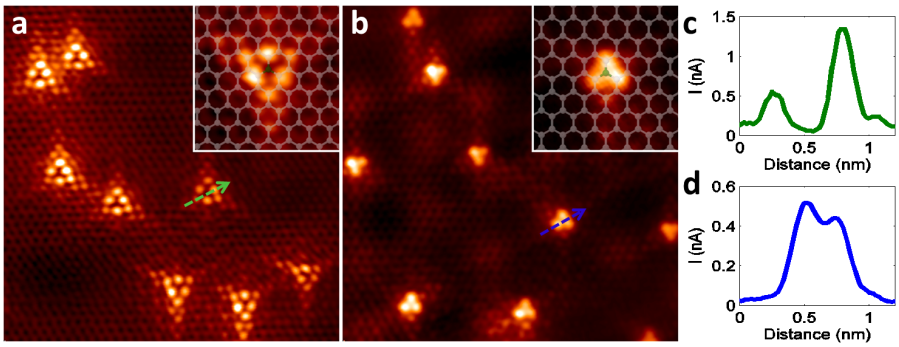

Figure 3.5: A pair of 9×9 nm^2 current maps of graphene with substitutional N dopants exhibiting the two most frequently observed atomically-resolved contrasts: (a) hollow-triangle contrast and (b) full-triangle contrast, bias -0.4 V. The insets show registration of the dopants with the graphene lattice. (c), (d) The line profiles of the tunneling current corresponding to the lines indicated in figures a) and b), respectively.

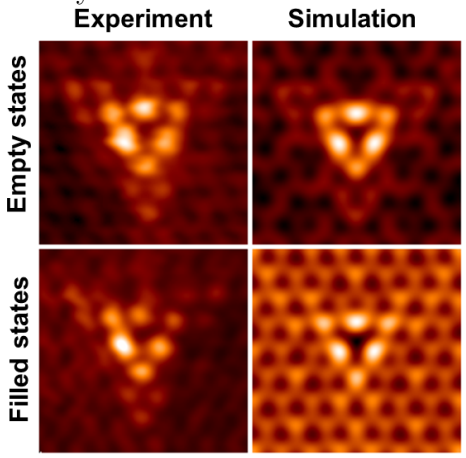

Figure 3.6: Filled and empty state comparison of the STM-simulations (+0.5 V and -0.5 V, surface-tip distance 3.5 Å) for C(111) tip model and the experimentally observed patterns (+0.4 V and -0.4 V) over the single N dopant. Size of all images is 1.7×1.7 nm^2.

favourable, since it has 0.715 eV higher formation energy than meta configuration. This contradiction between theory and experiment is still not clear. Most likely, there are some kinetic factors related to high temperature annealing favouring formation of the meta dopants.

In the Figure 3.9a we plot a histogram of the nearest neighbor distances between the N dopants. We treat the double dopants as two separate single dopants. Experimental histogram is consistent with a simulated random distribution at the same dopant concentration. The experimental mean nearest distance between all the N dopants without distinguishing the sublattices is 2.59 nm. The simulated value is in a very good agreement, with a value of 2.53 nm. However, if the histograms are evaluated separately for the nearest distances of the dopants in the same sublattices (see red plot in the Figure 3.9b) or in the opposite sublattice

Table 3.1: Total energy difference between the different possible configurations of the two N dopants in the graphene lattice: orto, meta and para which are depicted in the Figure 3.8.

Configuration	Total energy difference (eV)
Para	-
Meta	+0.345
Orto	+1.060

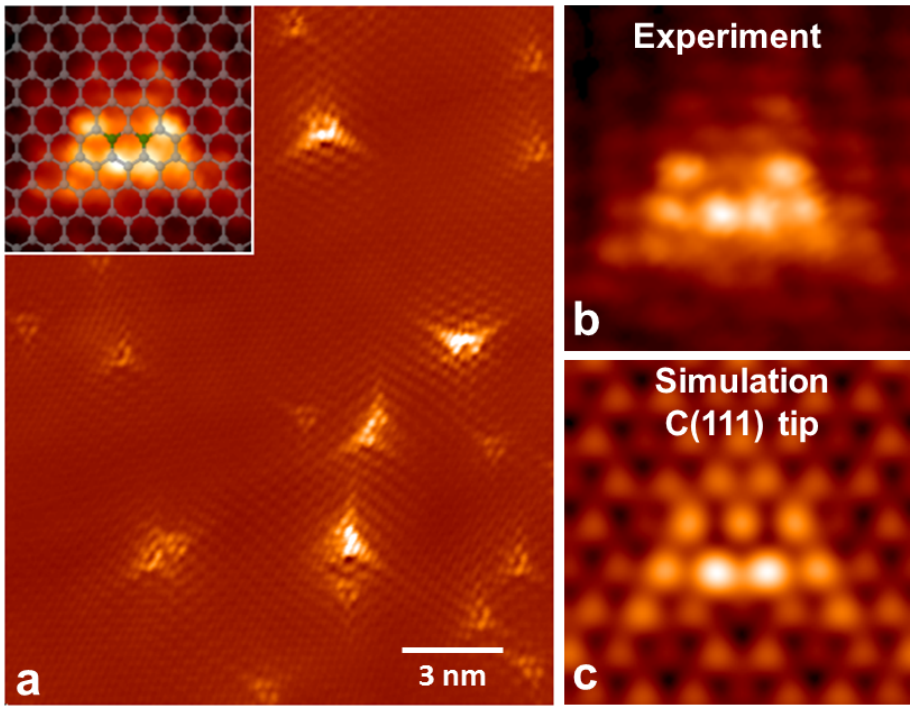

Figure 3.7: (a) Constant height STM image (0.4 V, 0.15 nA) of a sample doped with a higher amount of N dopants; the inset shows an overlay of the graphene lattice with two substitutional N-atoms on a zoomed meta-dopant. (b)-(c) Experiment to theory comparison of the two STM contrast observed over the meta-dopant.

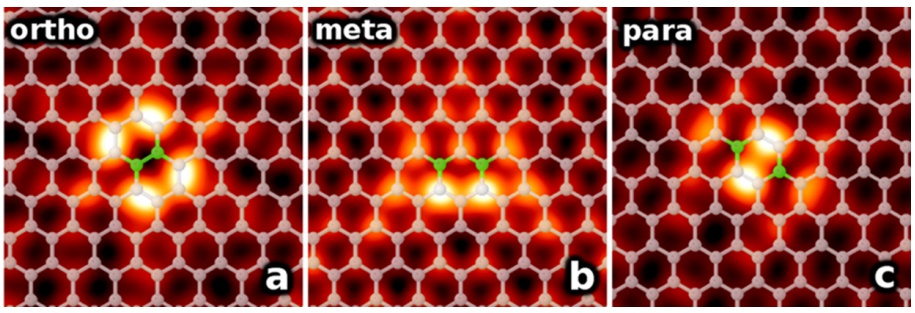

Figure 3.8: Calculated filled states, constant-height STM images, and a ball-and-stick model overlays of the three basic two-atom N dopants, obtained at -0.5 V, for C(111) tip and 3.5 Å tip-sample separation. The configurations are (a) ortho, (b) meta, and (c) para.

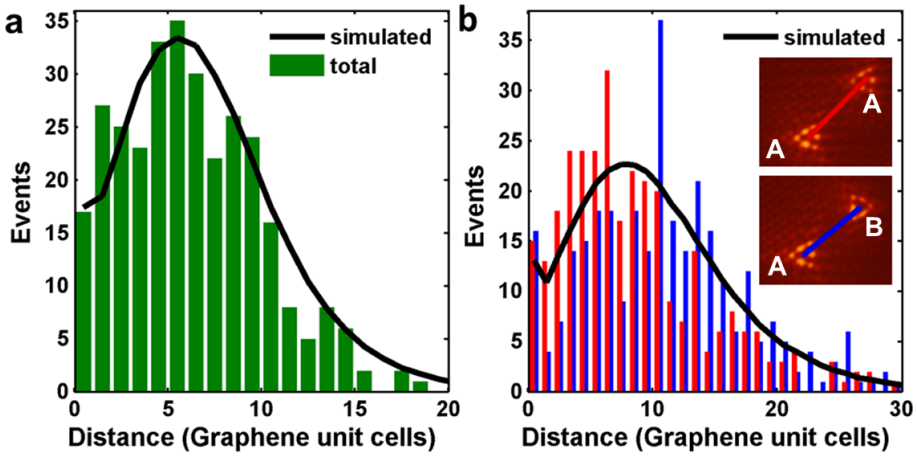

Figure 3.9: Histograms of the experimental nearest-neighbor distances for (a) all dopants independently of the sublattice and (b) depending on the sublattice, showing a preference for shorter distances for the dopants that reside in the same sublattice. The simulated histograms of the nearest neighbour distances are evaluated on a random spatial distribution of dopants without any preference.

(blue plot in the Figure 3.9b), there is a significant split of the mean values for these cases. The mean nearest distance for the dopants in the same sublattice is 3.63 nm; whereas the mean nearest distance for the dopants that are in the opposite sublattices is significantly larger: 3.99 nm. Both histograms are considerably different from the simulation of a random distribution, which has a mean value of 3.69 nm. Thus, N dopants distribution in graphene is not completely random. It can be interpreted as a following: at high concentrations when the mean nearest distance is relatively small, N dopants prefer to occupy the same sublattice. This again indicates that ion-bombardment implantation process is more kinetically driven, while CVD methods achieve thermal equilibrium [135]. We would like to note that much stronger preference of this type has been recently observed in the case of N doped graphene doped prepared using the CVD method [147].

To analyze the impact of the single N dopants on the electronic structure of graphene we performed site-dependent measurements of the differential conductance dI/dV (Figure 3.10). Our dI/dV spectra are similar to previously published data [135, 142]. Over the N atom, we observe two characteristic depressions: at zero bias and near -400 mV (green arrow in Figure 3.10). The latter is associated with the Dirac point, which is shifted toward lower energies with respect to the undoped graphene region on the same substrate (near -350 mV, marked by the blue arrow) due to the presence of N dopants. The shift of the Dirac point over bare graphene (350 mV below the Fermi level) is related to the charge transfer from the substrate as was discussed in the Section 3.1. The second dip at the zero bias voltage has been explained by Zhang *et al.* in terms of inelastic tunneling accompanied by excitation of an optical phonon mode in pristine graphene

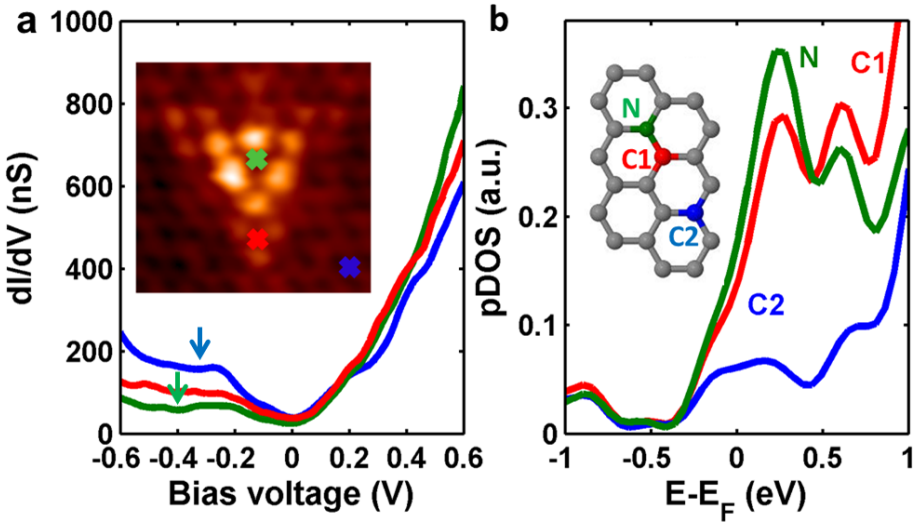

Figure 3.10: (a) Experimental dI/dV spectroscopy taken at different positions: above N dopant (green), in the surrounding of the dopant (red) and on the graphene region (blue). The spectra were taken at I_{set} = 1.0 nA. The arrows mark the dips in the spectra for the N atom and the surrounding graphene. (b) Plots of the calculated projected density of states for N dopant and two C atoms as indicated in the inset.

monolayer that enhances the tunneling current outside the gap [107].

The graphitic N acts as an electron donor in graphene and this gives rise to the n-type doping effect on graphene electronic structure. The observed shift of the Dirac point in STS towards lower energies is consistent with this prediction. The n-type doping on N doped graphene/SiC(0001) is strongly dependent on dopant concentration as it was demonstrated by ARPES measurements performed by F. Joucken *et al.* [148] and J. Sforzini *et al.* [146]. On the other hand, pyridinic N-defects in graphene result in p-type doping effect [149, 142, 150, 151]. From this point of view, our N doping method allows preparation of graphene with predefined electronic properties, since it results in exclusive presence of graphitic like N dopants in the graphene lattice.

3.2.3 XPS and NEXAFS on N doped graphene

To get more insight into the electronic properties and chemical environment of the N dopants in graphene, we performed the NEXAFS and a highly resolved XPS measurements of the N 1s photoemission peak. The N K-edge absorption spectra presented in Figure 3.11a exhibits π^* and σ^* resonances in the normal and grazing incidence geometries. This is a clear indication that the ion-implanted N atoms are sp^2 hybridized and are a part of the graphene π system.

The two main components of the photoemission N 1s structure in Figure 3.11b are located near 401.5 and 403 eV (binding energy). These are most likely associated with the majority of the N substitutional dopants on the single-layer

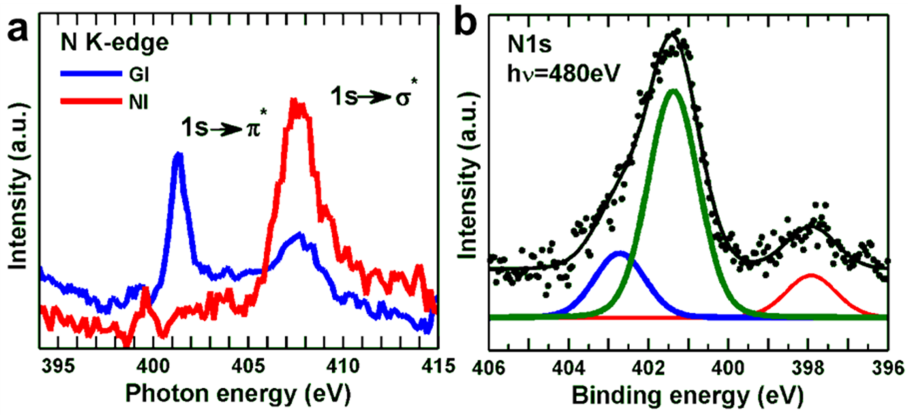

Figure 3.11: a) Absorption spectra near the N K-edge showing the π^* and σ^* resonances of the N incorporated in the graphene honeycomb lattice and b) photoemission peak of N 1s fitted with three components.

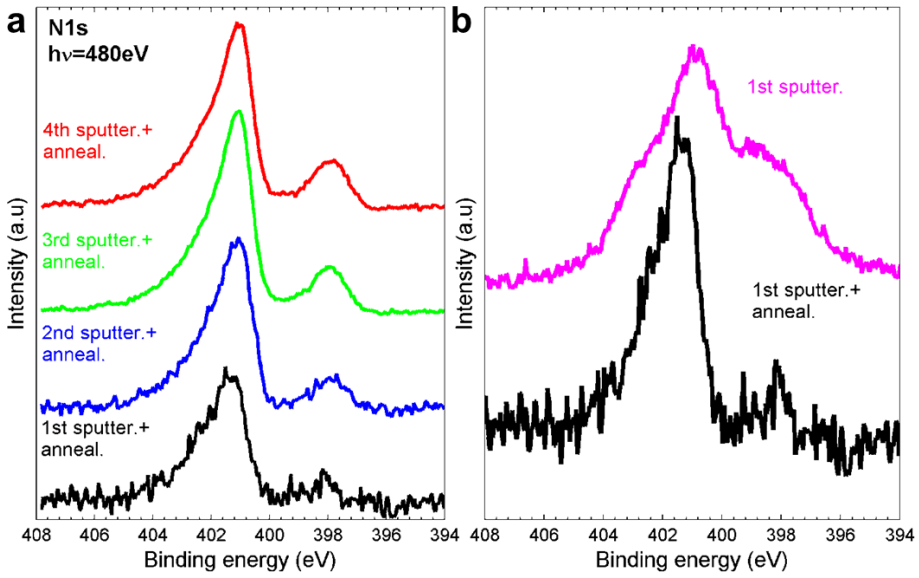

Figure 3.12: a) N 1s photoemission peak measured after every N^+ sputtering and annealing cycle. b) N1s photoemission peak measured just after exposing the sample to the flux 100 eV N^+ ions for 40 min (magenta curve) and followed by annealing (black curve).

(403 eV) and bilayer (401.5 eV) graphene, as seen in the STM images. The smallest component at 398 eV accounts for 11% of the total N 1s intensity, and it is usually associated with the pyridine-like N defects [152, 139]. On the other hand, in our STM images, we have never observed any features that could be related to such type of defects. Therefore, we assign this component either to N dopants incorporated in the buffer layer fraction on the substrate or to some type of N atom configuration in the subsurface area. Moreover, according to recent studies this peak might arise from the N atoms which diffused to the SiC bulk during the annealing process [146].

The N doped samples just after the ion implantation but before the high temperature stabilization have a very broad core-level lineshape in the photoemission spectroscopy, as shown in the Figure 3.12b. We interpret it by high contribution of pyridinic and pyrrolic-like defects on the surface created during the N-ion implantation process. However, after the annealing, the spectral components become significantly sharper. We explain this by a recovery and healing of this defects in graphene and reduction of the number of different features on the surface.

In our attempts to increase the concentration of the dopants, we have observed that repeating the procedure increases the dopant concentration and finally leads to saturation. In the Figure 3.12a we show the N1s photoemission peak measured after a few consequent similar N^+ sputtering-annealing cycles performed on the same surface. The peaks measured after third and fourth cycle have qualitatively similar shape suggesting the saturation of the dopant concentration. Moreover, all four spectra exhibit the three main peaks discussed above, suggesting complete recovery of the surface by annealing even at extremely high N concentrations. According to our STM studies the maximum achievable concentration of the N dopants is $\approx 1.6\%$.

We would like to note that the surface prepared using our doping approach has an extraordinary stability. Even after exposure to the ambient conditions, the N doped graphene layer did not change its physical properties. After reinsertion into the UHV and degassing at 1100 K, the sample exhibited the same properties as before.

3.3 B doped graphene

3.3.1 B doping method

Figure 3.13 shows a scheme of the growth method which we applied to achieve the B doping. First, the bare SiC(0001) substrate is cleaned *via* a Si flux and enriched with B atoms, which are deposited on the annealed sample. B atoms are introduced either by an e-beam evaporation of B from the graphite crucible or along with the Si flux from a heavily B doped Si evaporation source during the growing process. Subsequent annealing above 1050°C causes Si depletion and formation of the buffer layer with incorporated B atoms. Annealing of the sample further above 1150°C leads to Si sublimation from the upper surface layers, thus transforming the buffer layer into the B doped single- and bilayer graphene.

In our experiments, we successfully used both SiC(0001) polytypes 4H and 6H for the B doping. We did not use the carbon terminated side of the SiC($000\bar{1}$) substrate. However, we believe that our B doping approach can be also applied for C-face of SiC substrate.

The B concentration in graphene can be controlled by tuning the amount of B deposited on the bare SiC substrate prior to the high-temperature annealing. In the Figure 3.14, we show representative STM images of two samples with different concentrations of the B dopants 0.05% and 0.11%.

Similarly to the N dopants the substitutional B dopants are remarkably stable in the ambient conditions. We did not observe any variations in the concentration of the dopants or their structure after exposing the samples to air for long time periods (more than 10 days). Annealing of the sample up to 800°C under a 10^{-5} mbar CO and O_2 atmosphere also did not induce any changes to graphene nor to the B dopants. However, after the repeated annealing cycles at temperatures above 1000°C in the UHV (several hours in total) we observe a reduction of the dopant concentration, in both STM and XPS measurements. Such an effect is most likely caused by the diffusion of the B atoms into the SiC bulk.

3.3.2 STM on individual B dopants

In the Figure 3.15b, an STM overview image of the B doped graphene grown on 6H-SiC(0001) is presented. A $\approx$ 40 nm-wide stripe of SLG is located between two BLG domains. Both SLG and BLG regions appear decorated with atomic scale features. We show a zoom on the SLG region in Figure 3.15c, which reveals randomly distributed single dopants and the typical quasi-periodic 6×6 modulation characteristic for the SLG grown on SiC substrate [12]. The dopants are well-separated from each other and their prevalent locations are in the elevated areas of the modulation. The images in Figure 3.15d,e show the BLG region with

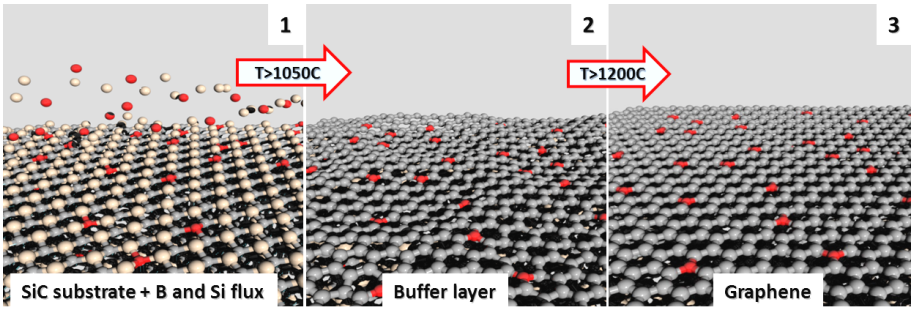

Figure 3.13: Scheme of the preparation procedure of B doped graphene on the SiC(0001) substrate. Gray, light brown, and red colors correspond to C, Si, and B atoms, respectively.

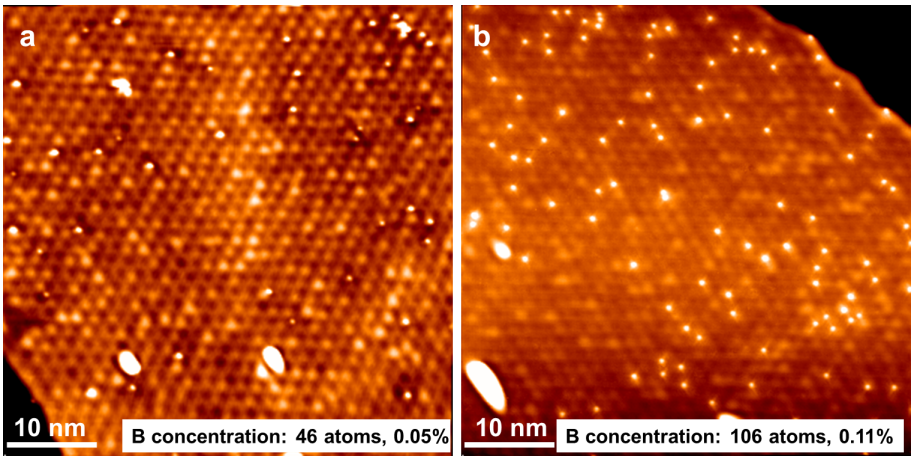

Figure 3.14: Large-scale constant current STM images of the two samples with different concentrations: a) 0.05% and b) 0.11%) of the B dopants. The sample with higher dopant concentration was produced by increasing the amount of deposited B on the bare SiC substrate prior to the high-temperature annealing. Scanning parameters are: a) V_{bias}=-1.5 V, I=0.33 nA and b) V_{bias}=-1.5 V, I=0.12 nA

a smaller corrugation due to a better decoupling from the substrate. This allows recognition of the dopants, present in the two different orientations. Similarly to the substitutional N dopants we observe the two types of B dopants corresponding to the A and B sublattices of the graphene honeycomb structure [1]. The ratio between dopants in both sublattices is roughly 1:1. Comparison of the BLG images taken with negative and positive voltages on the tip (filled and empty states, Figure 3.15d and e, respectively) reveals a dark halo around the dopants in the empty states image. Noteworthy the characteristic STM contrast of the dopants resembles the one reported recently on the B doped graphene grown by CVD method on the Cu substrate [136]. The overall dopant concentration on SLG and BLG in this particular experiment was below 0.1% of the atoms in the topmost graphene layer.

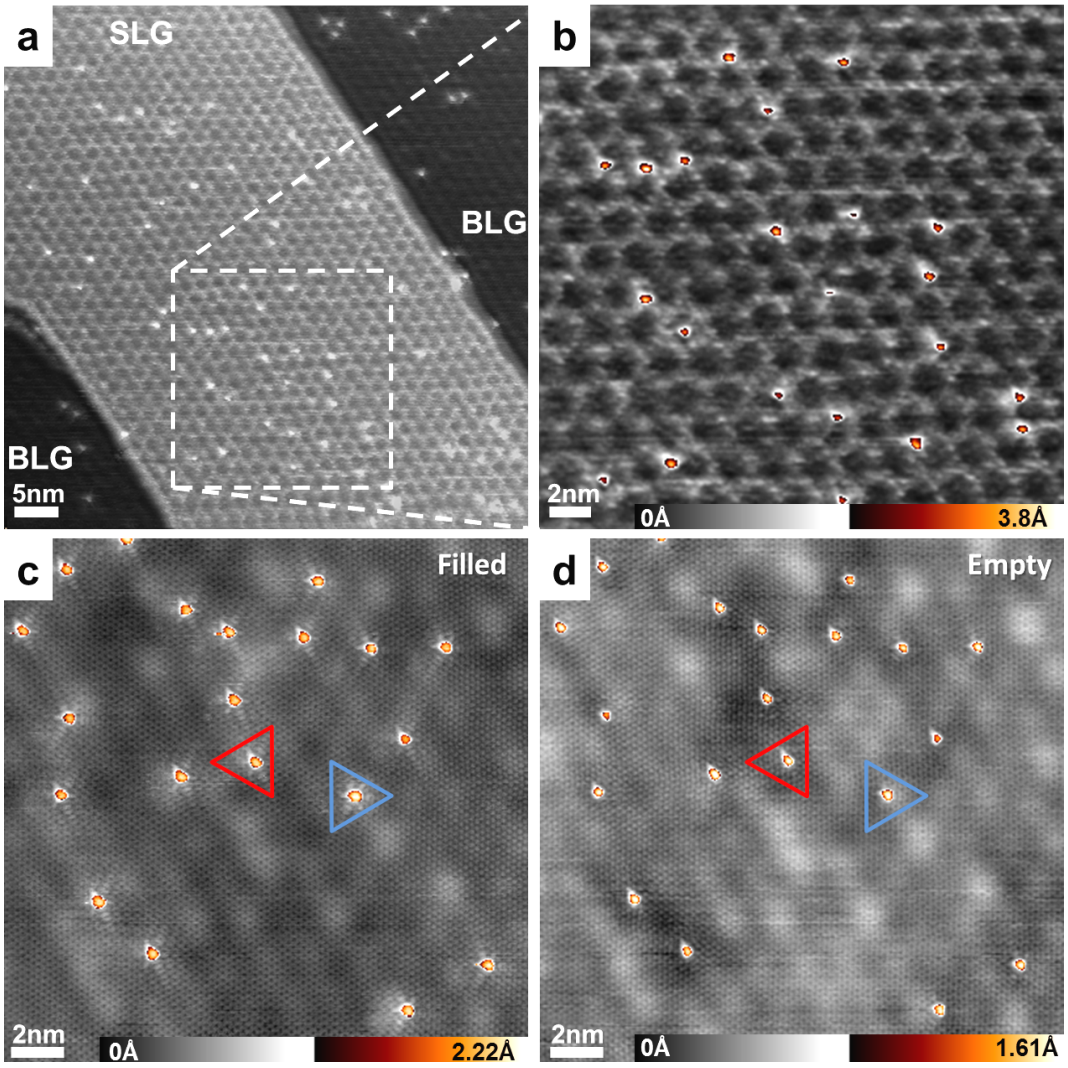

Figure 3.15: (a) Large-scale STM image (-0.98 V, 0.2 nA, 60 × 60 nm^2) showing the presence of dopants in single- (SLG) and bilayer graphene (BLG) prepared following the procedure described in Figure 3.13. (b) Magnified region of the B doped SLG (-1.0 V, 0.2 nA, 25 × 25 nm^2). (c) Occupied and (d) empty state STM images (-0.5 and 0.5 V, 0.15 nA, 20×20 nm^2) of the B doped BLG on 6H-SiC(0001). Red and blue triangles denote B dopants in the two inequivalent graphene sublattices.

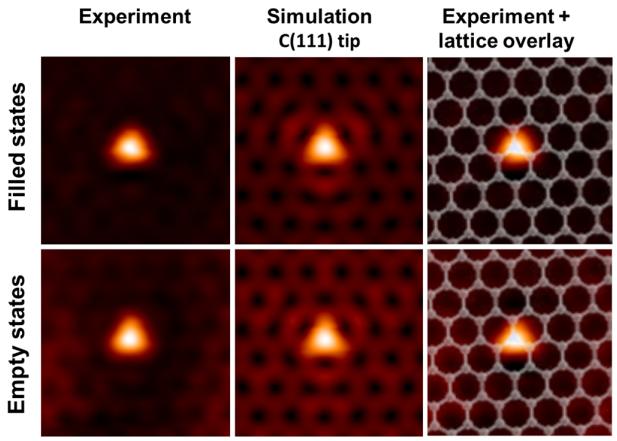

Figure 3.16: The simulated and experimental STM image of the single B dopant taken at bias voltages ±0.4 V. The simulations were performed for the C(111) tip for tip-sample distance 3.5 Å.

In the Figure 3.16, we compare the experimental atomically-resolved STM of single substitutional B dopant with a simulated one. We find an excellent agreement for both filled and empty states. We also overlay the experimental image with graphene lattice. Unlike for the N dopant, only one protrusion is observed over the B site. According to the theoretical calculations the B substitution is not accompanied by a significant out-of-plane relaxations of B dopant and its C neighbors. Therefore, we explain the observed tunneling current maxima by increased density of the electronic states over the B dopant. To analyze the influence of the

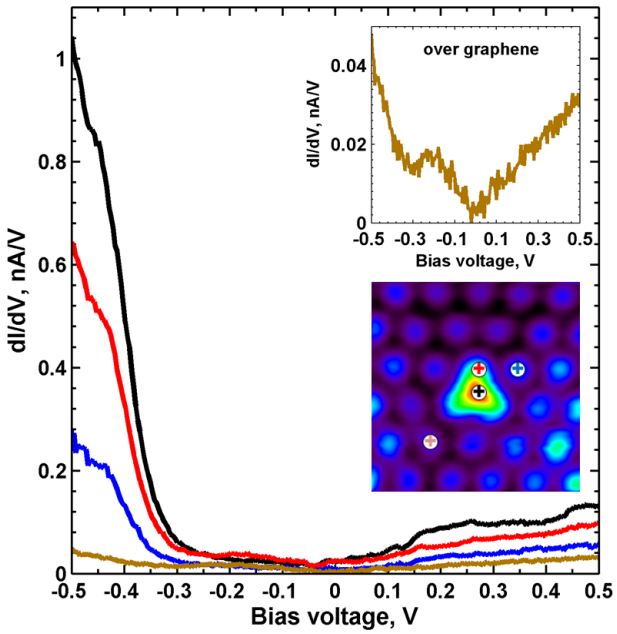

Figure 3.17: Experimental STS taken at different positions over the B dopant and its vicinity as shown at the inset image.

B dopants on the electronic structure of graphene we performed site-dependent measurements of the differential conductance dI/dV (Figure 3.17). Similarly to

the N case the dI/dV curves measured on the graphene area around the dopants exhibit two characteristic dips. Near the zero bias voltage and around the -0.3 eV [1]. Over the B dopant and its vicinity we observe a strong increase of the filled states differential conductance. This suggests presence of high density of electronic states at the energy -0.3 eV below the Fermi level.

3.3.3 XPS and NEXAFS on B doped graphene

We now focus on the growth mechanism of B doped SLG/SiC(0001). To study this we deposited the B on bare SiC substrate and an annealed sample with 50°C temperature increments. After every annealing step the surface was monitored by XPS, NEXAFS and LEED. Figure 3.18 summarises B1s and C1s spectra after each annealing step. The bare SiC substrate exhibits Si-rich 3×3 reconstruction and a single C1s peak at the binding energy 282.7 eV, arising from C in the bulk SiC. After the B deposition intense peak at energy 187.5 eV appears in the B1s photoemission line. It can be assigned to the metallic B on the surface [153]. This peak remains unchanged after annealing at 950°C.

Annealing the sample at 1000°C results in the formation of mixture of phases: $\sqrt{3} \times \sqrt{3}$ and BL. Therefore, C1s line exhibits two components at 283.2 eV and 285.3 eV. The latter corresponds to the C from buffer layer and appears also after further annealing steps. A few different peaks appear in the B1s spectrum, suggesting the change chemical state of B. We assign the central peak at 189.8 eV to the B intermediate state related to $\sqrt{3} \times \sqrt{3}$ phase. The two other peaks at 190.8 eV and 188.6 eV are detected even after the growth of SLG. The peak with lower binding energy (188.6 eV) was observed also for SiC-B composites [154]. This is an evidence of the B diffusion process into the SiC bulk. The peak at 190.8 most likely arises due to B incorporated into the BL.

After the annealing at 1150°C the B doped BL transforms to the B doped SLG. This results in a new peak at 284.7 eV corresponding to the sp^2 hybridized carbon in the C1s photoemission line. Importantly, the high-temperature annealing results is decreased intensity of the bulk B component (188.6 eV). This might be caused by further diffusion of B into the bulk or the influence carbon layers onto the signal. On the other hand, the intensity of the peak at 190.8 eV remains unchanged, suggesting high thermal stability of the sp^2 hybridized B dopants. The presence of the only one component evidences one bonding configuration of the B dopants. Moreover, the position of the peak (190.8 eV) is similar to BL and SLG. Therefore, we conclude that B dopants have the analogical chemical environment in BL and SLG.

To gain more insight on hybridisation type of the B dopants during the an-

[1] In this case the dopant concentration is low and therefore doping effect too.

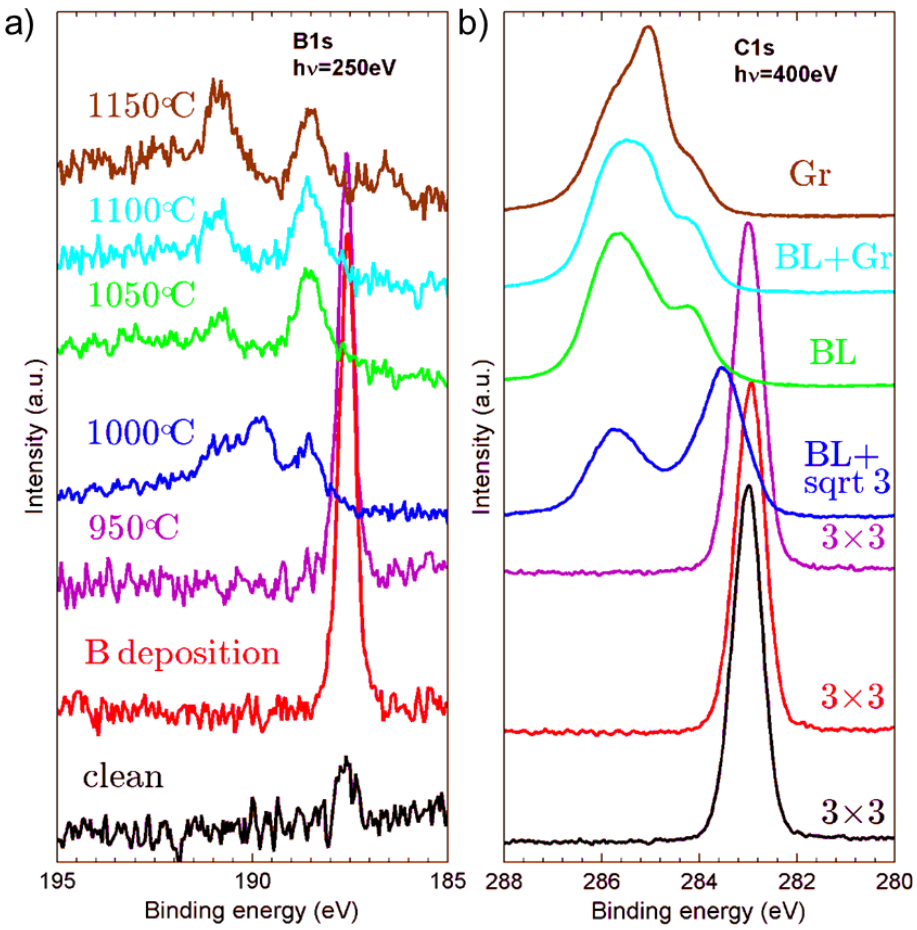

Figure 3.18: The XPS spectra of C1s (a) and of B1s (b) measured with a photon energy of 400 and 250 eV, respectively, are shown for each annealing temperature.

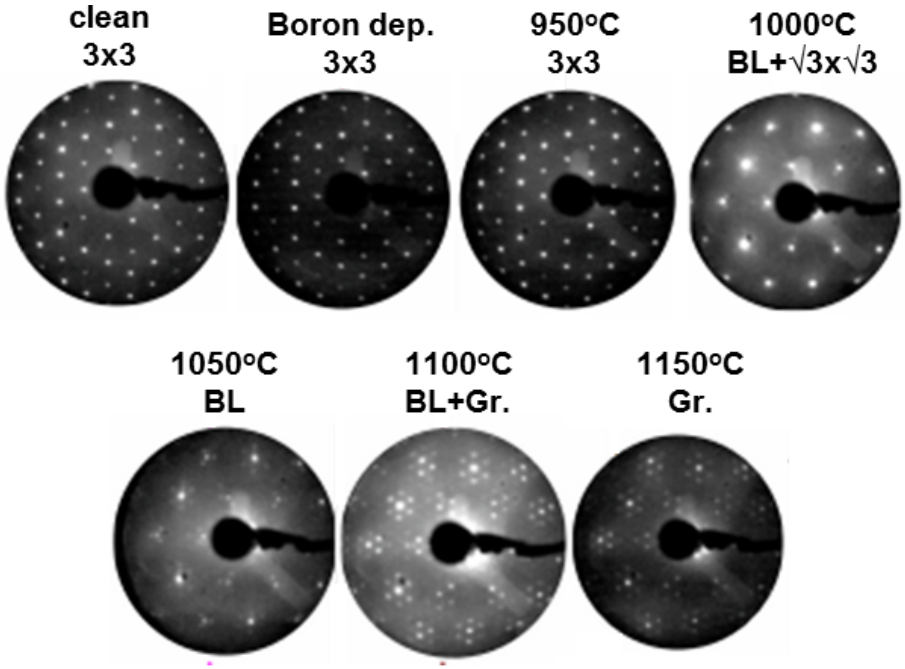

Figure 3.19: The LEED images of all annealing steps.

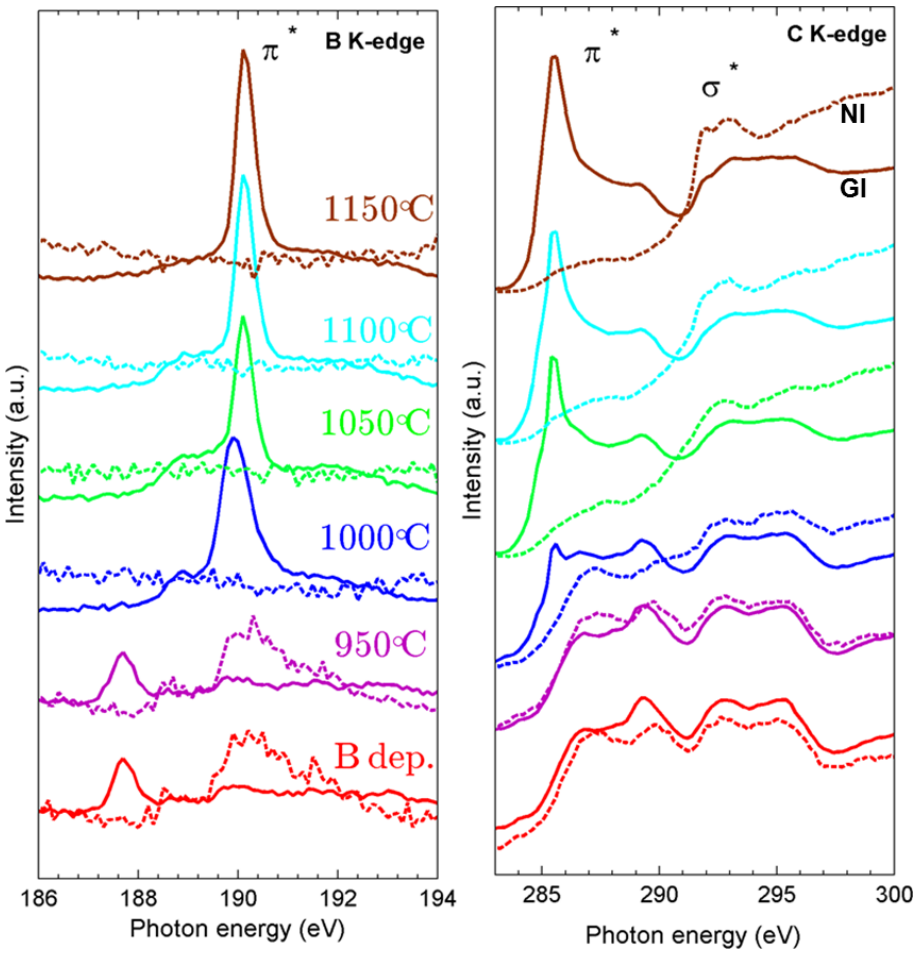

Figure 3.20: The C K-edge and B K-edge NEXAFS spectra measured in the grazing incidence (solid line) and normal incidence geometries (dashed line) for the every annealing step.

nealing process, we performed NEXAFS measurements of the B K-edge and C K-edge presented in the Figure 3.20. The measurements were carried for the grazing incidence (GI) and normal incidence (NI) geometries, indicated by the solid (GI) and dashed lines (NI), respectively. The B K-edge spectra just after the B deposition exhibits the two characteristic peaks at 187.7 eV and 190.1 eV in GI and NI geometries, respectively. The peaks are related to the metallic B and remain unchanged after annealing up to 950°C. Further sample annealing at 1000°C results in appearance of only one π resonance at 190.1 eV in B K-edge spectra for GI geometry. It remains without a major change after annealing at 1150°C and formation of graphene on the surface. The graphene formation is marked also by its π and σ signatures in the C K-edge spectra at GI and NI, respectively. Therefore, we conclude that formation of B doped BL occurs at 1000°C and B doped graphene at 1150°C.

3.3.4 B doped quasi-free-standing monolayer graphene

In the previous Section 3.3.3, during analysis of the XPS and NEXAFS spectra we confirmed that B deposition on the bare SiC(0001) substrate followed by annealing at 1000°C results in the formation of BL with incorporated B atoms. Recent studies have proven that BL can be decoupled from the SiC, both structurally and electronically, by the hydrogen intercalation [111]. The H atoms tend to saturate the dangling bonds of the substrate atoms. This results in reducing the BL buckling and its conversion to the quasi-free-standing monolayer graphene (QFMLG). In principle, the BL with incorporated B atoms can be particularly suitable for the preparation of B doped QFMLG.

To test this idea, we performed the following experiment. At first, we prepared the B doped BL by the controlled B deposition on the bare SiC(0001) substrate followed by annealing at 1000°C. The resulting surface is presented in the Figure 3.21a. The STM images do not reveal presence of any features which might be related to the B substitutions. We explain this by high apparent corrugation and complexity of the BL. Nevertheless, the presence of sp^2 hybridized B atoms in the BL is clearly evidenced by the NEXAFS and XPS experiments.

In the next, H intercalation procedure was performed. For this, the sample was annealed for 10 min at 750°C in the flux of atomic H. The pressure of atomic H was kept at 10^{-5} mbar and the H flux was produced using the hydrogen cracker.

In the Figure 3.21b, we show the representative STM image of surface after this treatment. Except for the BL with q-6 $\times$ 6 corrugation the surface contains significant amount ($\approx$ 50%) of relatively flat domains. Remarkably, the q-6 $\times$ 6 modulation disappears over the flat areas. This corrugation difference is visible on the cross-sectional profile (see Figure 3.21c) taken along the white arrow in Figure 3.21b.

The hydrogen penetrating the BL/SiC interface saturates the substrate dangling bonds and consequently removes the sp^3 hybridization between the BL and SiC. This results in drastic decrease of the BL corrugation and formation of very flat monolayer graphene as was demonstrated recently by J. Sforzini *et al.* [81]. The significantly lower corrugation of QFMLG in comparison to BLG was also reported by other STM studies [155].

In the Figure 3.21d, we present a surface which contains $\approx$ 90% of B doped QFMLG. This was achieved by increasing the duration of H intercalation process to 20 minutes. The atomically resolved STM image of this surface in the Figure 3.21e clearly demonstrates the presence of the triangular dopants on the QFMLG areas. Similarly to B doped BLG, two types of dopants corresponding to the different sublattices are observed. These dopants were not reported in the previous STM studies of QFMLG/SiC(0001). Moreover the STM contrast of these features is completely identical to the one characteristic for the B dopants

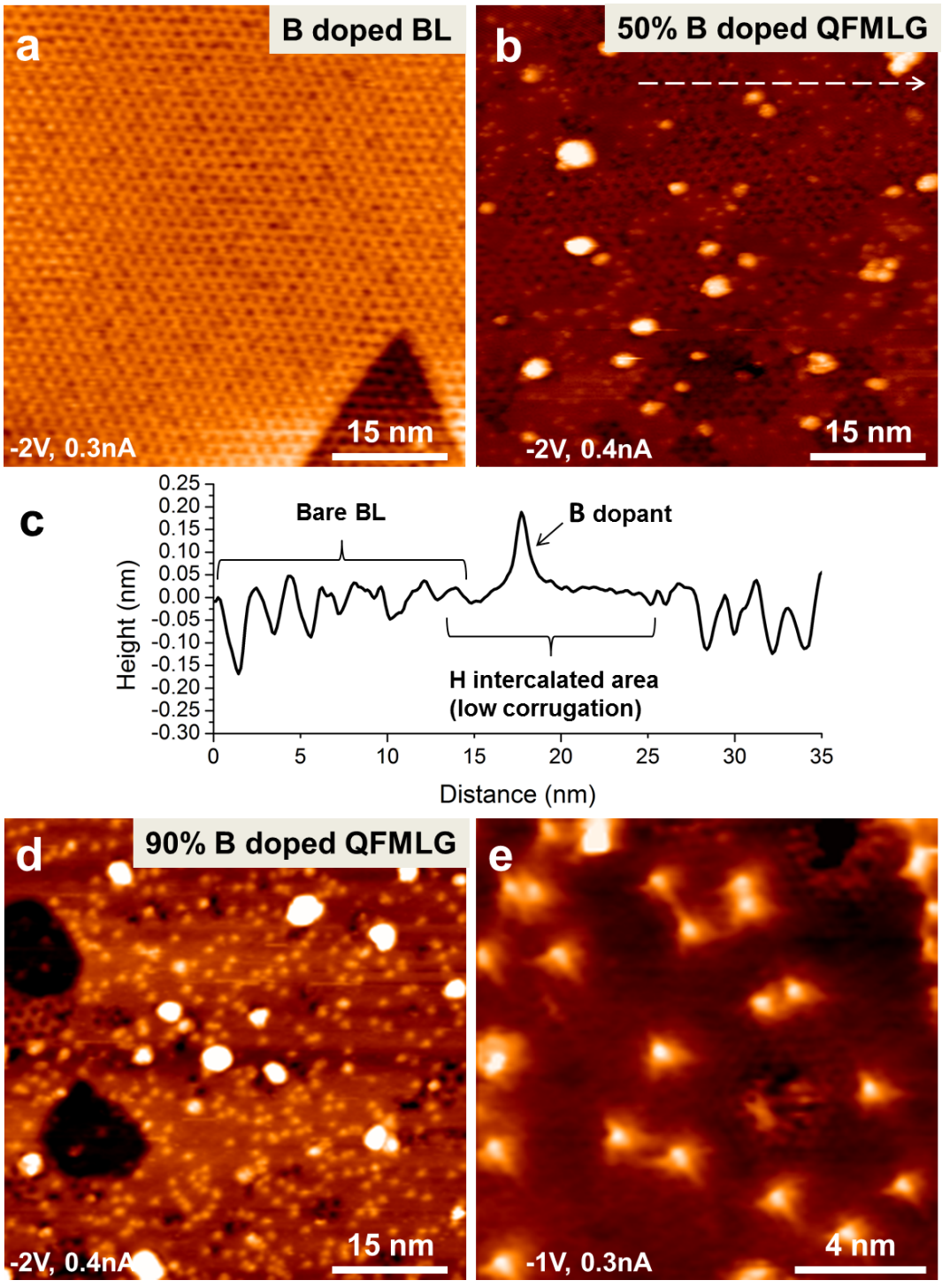

Figure 3.21: a) Large-scale STM image of the buffer layer with incorporated B dopants. b) The same surface after the 10 min of H intercalation procedure. The flat areas correspond to the B doped QFMLG. The fraction of QFMLG area is $\approx 50\%$ c) a line profile corresponding to the white arrow indicated in (b). d) The surface after the 20 min of H intercalation process. The fraction of QFMLG area is $\approx 90\%$. e) Atomically resolved STM image showing the presence of the single B dopants in the QFMLG.

in BLG. Therefore, we relate the observed dopants to the single substitutional B atoms in QFMLG. The B dopant concentration for this particular sample is $\approx 0.15\%$

Despite numerous studies of QFMLG/SiC(0001) system, our experiment, by the best of our knowledge, is a first effort of intentional QFMLG functionalization with substitutional dopants. The electronic properties of the B doped QFMLG are at the current stage unknown and require further experimental study. However, from our STM experiments we conclude that structural properties of B doped QFMLG are similar to the undoped one.

3.3.5 B doping through posterior treatment

In the previous Sections, we demonstrated the possibility to control the B concentration in graphene using our method (see the Figure 3.14). However, as it was concluded from the XPS study during the annealing process, significant amount of B diffuses to the bulk SiC. Therefore, the achieving of very high B concentrations (up to 0.5%) using our method remains challenging. To overcome this we propose an alternative approach for the as-grown graphene B doping through the posterior treatment.

Within our approach, we firstly deposited the desired amount of B onto the graphene at room temperature. In the next, the sample was annealed at 1100°C for 5 min. As it will be shown in the following, the annealing process leads to the B incorporation into the graphene lattice. Noteworthy, our B doping approach is very similar to the one applied by W. Wan *et al.* for the incorporation of isolated Mo atoms into the graphene/SiC(0001) [156]. In their research, the authors deposited MO_3 on graphene and later performed high-temperature annealing to produce the Mo-doped graphene.

In the Figure 3.22a, we show a representative STM image of the surface after the B deposition. Our STM measurements show formation of the differently-sized B clusters on the surface. This tendency for cluster formation can be explained by relatively low diffusion barriers on graphene and was observed for various metals, e.g. transition metals: Ni,Co [127], Fe [157] and rare earth metals Dy [158], Nd, Gd [159].

As shown in the Figure 3.23a,b the resulting surface exhibits significantly higher amount of the B dopants ($\approx 0.5\%$) than the one produced by the B predeposition on the bare SiC substrate. Empty state STM images (see Figure 3.23b,d) reveal the characteristic dark hallo around the single B dopants which is absent around the double dopants. Atomically resolved STM images also indicate high contribution of the double B dopants in graphene (see Figure 3.23c,d).

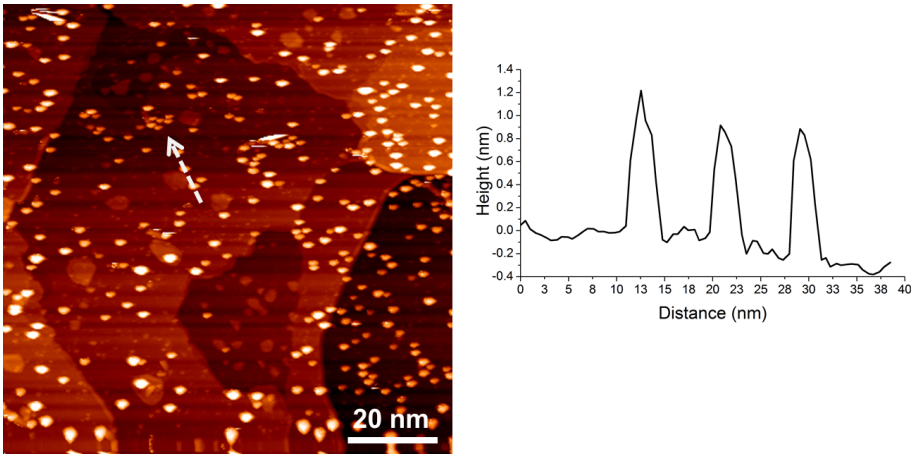

Figure 3.22: a) Large-scale STM image of the graphene/SiC(0001) after deposition of B. It shows presence of the B clusters on the surface (V=-1.5V, I=0.13nA). b) Profile taken through the three B clusters, as indicated by the white arrow in the image a).

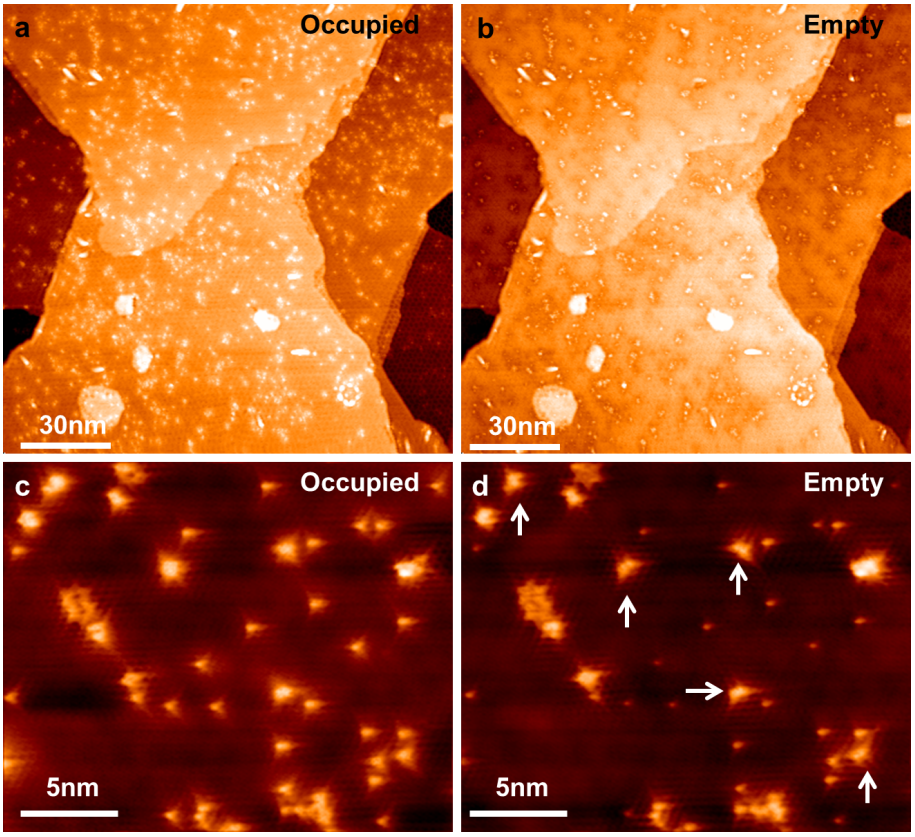

Figure 3.23: (a),b) Occupied and empty state large scale STM image of graphene after the deposition of B and annealing at 1100°C (V_{bias}=±1.5 V; I=0.19 nA). c),d) Occupied and empty state atomically resolved STM image of the same surface (V_{bias} =±0.8 V; I=0.19 nA). White arrows mark a positions of double B dopants.

3.4 B,N co-doped graphene

3.4.1 Preparation of B,N co-doped graphene

To explore the possibility of a B,N co-doping and to compare the electronic properties of individual single B and N dopants, we used a two-step approach. With this method, doping levels of both B and N atoms are adjustable. We prepared first the B doped graphene/SiC(0001) sample with a desired B dopant density by the method described in the Section 3.2.1. The sample was then exposed to N-ion flux and later stabilized by the high temperature annealing. The graphical scheme in Figure 3.24a summarizes the procedure. Precise control over the N doping concentration can be attained by changing the flux density and duration of the ion irradiation. For the B doping control, the crucial factor is the amount of B, deposited on the sample surface before the graphene growth.

In the Figure 3.24b, we show an atomically-resolved STM scan of the surface after such treatment. Single substitutional N dopants appear as triangular-shaped objects with pronounced depressions over the N site, whereas the B dopants possess a maximum tunneling current intensity over the B dopant. Thus, both types of the dopants (B and N) can be clearly distinguished.

The Figure 3.25 displays the STM image of graphene with higher concentrations of the N dopants. The doping levels reached 0.68% and 0.11% for the N and B, respectively. The majority of the observed features can be assigned to the single N or B dopants, and double N dopants in meta or ortho configurations (see the Figure 3.8). However, significant amount of new features appears on the surface. These objects might be related to the double BN dopants. The influence of such a defects on the electronic structure of graphene is still unclear and requires further studies.

3.4.2 STM/AFM on B,N co-doped graphene

To gain more knowledge about the local chemical and electronic properties of B and N substitutional dopants, we performed simultaneous nc-AFM/STM measurements at low temperature (1.2K) using the Kolibri sensor. Namely, we acquired 3D constant-height nc-AFM/STM maps over the single N and B dopants. The full sets consisted of images taken with 10 pm height increments, thus creating 3D maps of the tunneling current and the frequency shift. Note, the 3D scans for N and B dopants were taken during different experimental sessions, *i.e.* the tip apex was not the same.

Figures 3.26a,b display 3D representation of normalized site-dependent tunneling current $I(z)$ as a function of the tip position over the N and B dopant, respectively. Snapshots of the corresponding constant-height STM images taken

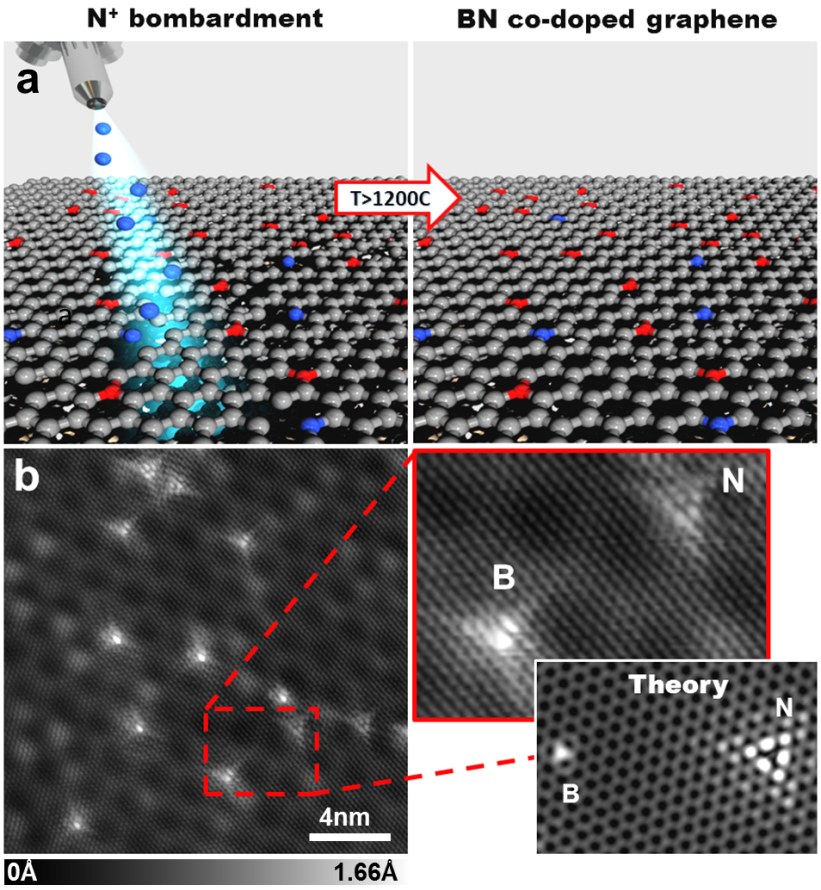

Figure 3.24: (a) Scheme of BN co-doping: N ion implantation into the previously B doped sample and thermal stabilization. (b) Constant-current STM image showing presence of N and B dopants in the graphene lattice (U = -0.7 V; I = 0.15 nA; 20 × 20 nm^2). The inset shows a zoomed area with a detail of N and B single-atom dopants and a simulated STM image for comparison.

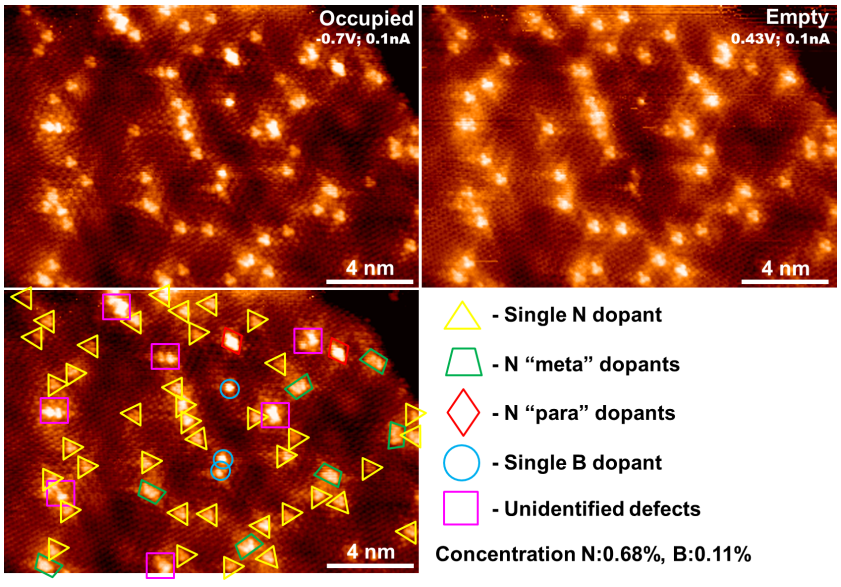

Figure 3.25: Filled and empty state STM scan of the B,N co-doped graphene with the individual features distinguished.

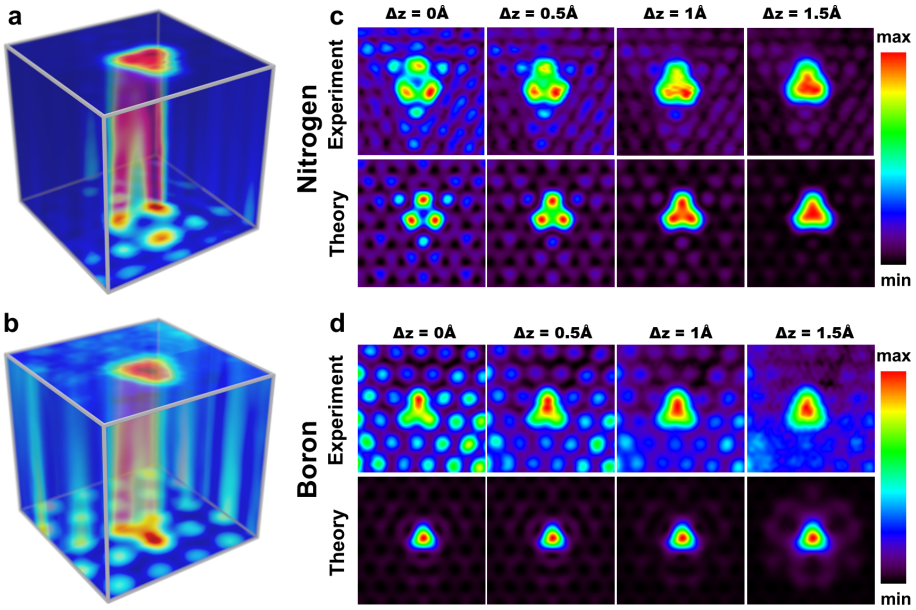

Figure 3.26: A representation of the 3D maps of tunneling current for (a) N dopant (-100 mV, 1.8×1.8×0.15 nm^3, I_{set} = 1 nA) and (b) B dopant (-150 mV, 1.8×1.8×0.15 nm^3, I_{set} = 1 nA). The 3D maps are normalized for each height step. (c) and (d) Selected slices from the 3D map, taken above the N and B dopant, respectively, compared with the STM-simulations generated using a carbon tip for the corresponding tip-sample distance range.

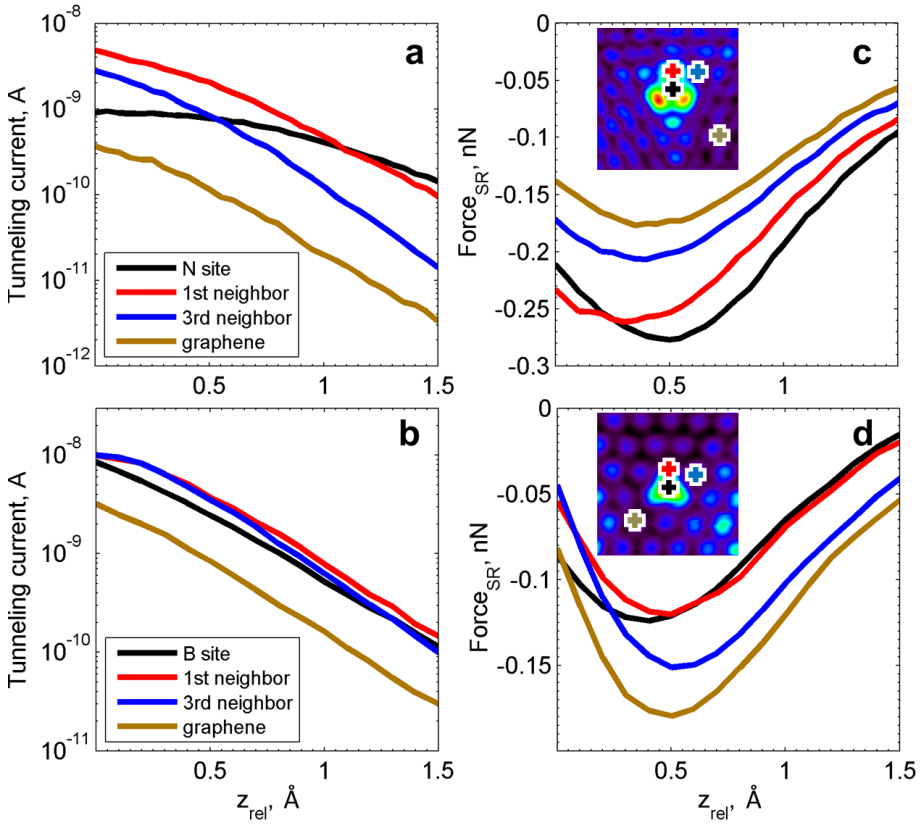

Figure 3.27: Experimental I(z) and F(z) spectroscopies taken at different positions over N dopant - (a), (c) and the B dopant - (b) and (d), with the insets denoting the measurement sites.

in selected tip-sample distances are shown in Figure 3.26c,d. We can clearly see the suppression of the tunneling current over N atom in the close tip-sample distance, while the maximum of the tunneling current signal is observed over the three nearest-neighbor C atoms. The depression over N atom is developed into the protrusion when the tip-sample distance is increased. In the case of B-site, the maximum of tunneling current is always detected over the B dopant independently on the tip-sample separation. Such characteristic behavior of the atomic contrasts observed above N and B dopants is robust and it was repeatedly observed during several experimental sessions with the different tip terminations.

For clarity, we also plot the tunneling current versus distance profiles $I(z)$ extracted from the 3D data over the several distinct atomic positions on and around the N dopant site as shown in the Figure 3.27a. The reference measurement on graphene, including first and third neighbor C-sites follows an almost ideal exponential decay, with the exception of the very close distances. In the close distance regime, the exponential growth is slightly suppressed, likely due to the onset of multiple-scattering effects [30].

The nc-AFM technique senses different kind of long and short-range forces simultaneously acting between tip and sample (see the Figure 1.4). The short-range forces appear only on the closest tip-sample z-distances of few Å. These forces are typically related to the local electrostatic or chemical interaction between tip apex and surface atoms. In other words, the short-range forces acquired over different sites provide information about the local chemical reactivity on different surface sites [160, 161]. Therefore 3D maps of the short-range force can provide further understanding of local chemical reactivity of N- and B doped graphene and potential of these dopants as a reactive sites for graphene functionalization with organic molecules [162, 163, 164].

Here we employ 3D set of nc-AFM measurements to analyze the local interaction over the B and N dopants. The measurements were done with two different tips with unknown chemical composition of the apex. Thus we cannot compare directly the local interaction between B and N sites. Instead, we can compare variation of the short-range interaction with respect to pristine graphene. The short-range atomic forces extracted from the 3D map of the nc-AFM signal, obtained simultaneously with the tunneling current, are plotted for the same sites as the current in the Figure 3.27d,e.

To convert the frequency shift curves (Δf) to the short range force ($F_{SR}(z)$) we used the Sader approach and subtracting the long-range contribution [39]. The long-range force was estimated for the individual dopant measurements by fitting the tails of curves taken above graphene with an inverse square dependence (see the Equation 1.17).

It is well-known that the pristine graphene shows a low chemical reactivity.

Indeed, we detected relatively small maximum attractive short-range forces, in range of few tenths of nN, over graphene during both measurements, see yellow lines in Figure 3.27c,d. This indicates that the interaction between the tip apex and surface carbon atoms is governed by a weak electrostatic interaction, rather than by formation of a true chemical bond. Similarly, we found relatively weak, but different maximum attractive short-range force over N and B sites. Since the previous findings corroborated that the dopants reside in the plane with graphene, the magnitudes of the maximum forces point towards their distinct local reactivity rather than topographic effect. In the case of N-site the maximum interaction is about 0.1 nN larger than over pristine graphene. In the case of B dopant, we detect smaller maximum attractive force (by 0.05) nN than on pristine graphene. In both cases, we observe that the maximum attractive force over the nearest neighbor C-atom is very similar to the dopant site in the vicinity. This indicates that the short-range interaction is mostly caused by the charge transfer between the dopant and surrounding C atoms. This is not unexpected, because the B and N atoms act as donor and acceptor centers in graphene. Nevertheless, the altered local electrostatic properties might play an important role in the interaction pathways of any polar molecules depending on their internal electrostatic charge distribution [162].

3.4.3 Destructive interference on N dopant sites

To get more insight into the characteristic STM contrast over N-site we carried out constant-height STM simulations of B and N dopants at selected distances using a carbon tip model, (see Figure 3.26c,d). The calculated STM images mimic very well not only the atomic contrast at given distance, but also its variation with gradual change of the tip-sample distance. In the case of B dopant STM images can be interpreted in terms of the surface local density of states. However, the atomic contrast observed for N dopant shows much more peculiar behavior, which cannot be explained only in terms of local density of states. In the next, we will demonstrate that such effect is driven by the quantum interference effect between different transport channels across the tunneling junction.

The excellent agreement between experimental evidence and calculated STM images together with the fact that the atomic contrast over B and N dopants is independent of tip apex indicates that the origin the different atomic contrast is related to surface electronic structure. Thus we analyzed the character of the electronic structure of B and N doped graphene relevant to the tunneling process near the Fermi level. The Figure 3.28a and Figure 3.28b represent the real space distribution of the electronic wave functions localized around the N and B dopants obtained from DFT simulations. We identify these two localized electronic states as significantly contributing to the tunneling current at low bias voltages. The

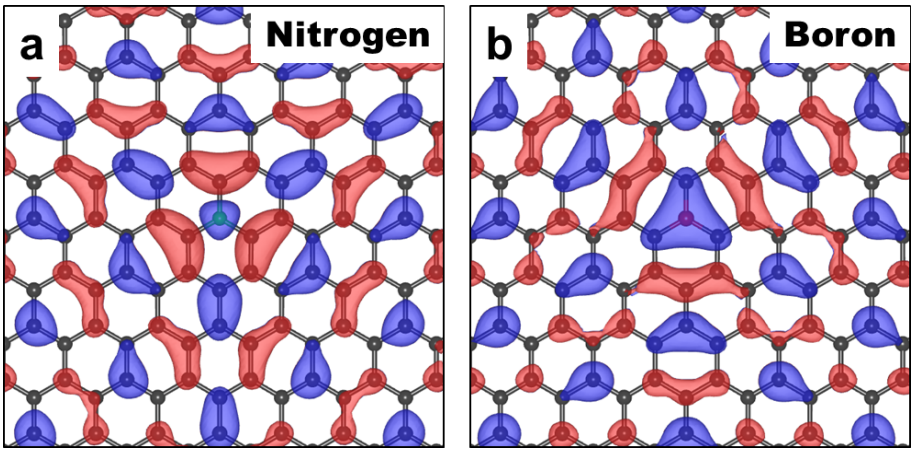

Figure 3.28: a) plot of the electronic state near the Fermi level for N dopant, showing the nodal structure in between N and the nearest C b) plot of the electronic state near the Fermi level for the B dopant.

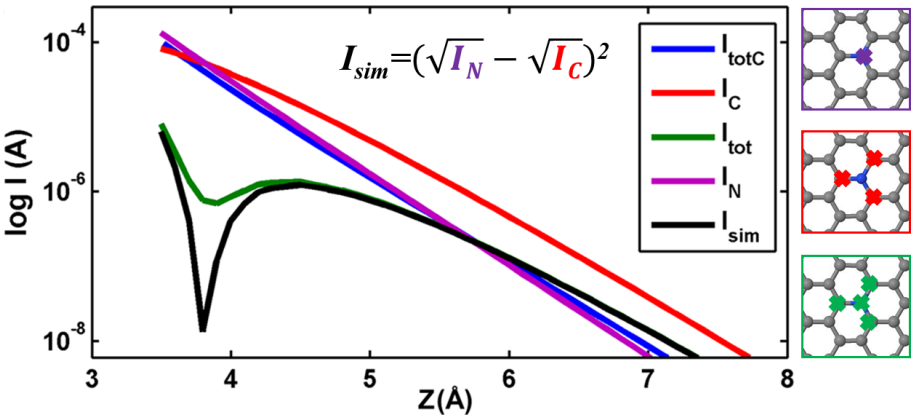

Figure 3.29: (c) The calculated tunneling current on the N dopant as a function of distance for N and C channels separately (I_N^N and I_C^N, respectively), the calculated total current (I_{tot}^N) including all channels, and a model using the formula $I_{sim} = (\sqrt{I_C^N} - \sqrt{I_N^N})^2$. The dip in I_{tot}^N marks the presence of a destructive interference in the electron tunneling. For a comparison with I_{tot}^N on the N dopant, the total tunneling current for the tip placed on one of the nearest-neighbor atoms C atoms (I_{tot}^C) is also shown. The upper index denotes position of the tip above N or the nearest-neighbor C atom.

most striking feature is that the wave function localized on N-site has anti-bonding character with a characteristic node inbetween the central N atom and its nearest neighbor C atoms. On the contrary, the B site has bonding character with the same sign as its nearest neighbor C atoms. The presence of the node is the crucial factor giving rise to the destructive interference effect on the tunneling current above the N dopant site [103]. In particular, it causes the opposite signs of amplitudes, corresponding to transport eigenchannels passing from tip apex to N atom or the nearest neighbor C atoms, respectively. Consequently, this results in the suppression of the tunneling current observed over the N dopant.

To demonstrate the phenomenon of the destructive interference directly, we calculated the tunneling current for the C(111) tip model above the N dopant using Green's function technique [103]. We selectively allow the tunneling process through: (i) the all surface atoms (I^N_{tot}), (ii) only the N atom (I^N_N) or (iii) only the three neighboring C atoms (I^N_C) as presented in the Figure 3.29. The $I^N_{tot}(z)$ curve shows a pronounced dip at close tip-sample distances when compared to the individual I^N_C and I^N_N current channels. The tunneling current is proportional to the square of a corresponding quantum-mechanical amplitude. Assuming an ideal destructive interference, we can approximate the amplitude for the resulting tunneling current I^N_{sim} by a difference between amplitudes for the partial flows through the N atom and through the C atoms: $I_{sim} = (\sqrt{I^N_C} - \sqrt{I^N_N})^2$. From the Figure 3.29, it is evident that the simulated tunneling current I_{sim} calculated using this formula has a remarkably similar character to I^C_{tot}, the total tunneling current calculated for the tip placed above one of the C neighbors, in the whole range of tip-sample distances. Therefore, we attribute the depression of the tunneling current near the N dopant to the destructive interference of the electron wave functions originating from the C and N atoms.

3.5 Conclusions

In this Chapter, we present robust method for preparation of N doped graphene on SiC(0001) in UHV conditions. For this, we exposed graphene/SiC(0001) to the flux the N^+ ions and latter stabilized it by the high-temperature annealing. The atomically-resolved STM and NEXAFS studies provide the evidence that the N dopants are present in the substitutional positions in graphene. At high concentrations, we observed the formation of double dopants which consist of two N atoms in meta configuration.

We developed and tested three different approaches to produce the B doped graphene on SiC(0001). One way is a controlled B deposition on the bare SiC(0001) substrate followed by sample annealing until graphene is formed. By means of STM, XPS and NEXAFS techniques we proved a graphitic-like incorporation of the B dopants into graphene lattice. Moreover XPS measurements also suggest a diffusion of the B atoms to the subsurface region. Alternatively, the B doped graphene might be prepared using the post-treatment technique. Within this method, the B is deposited on the as-grown graphene/SiC(0001) and later sample is annealed to induce incorporation of B into the graphene lattice. We showed that this approach yields significantly higher concentration of the substitutional B dopants. Finally, we demonstrated the possibility of growth of the QFMLG by the hydrogen intercalation of the B doped buffer layer.

We presented a method for the preparation of B,N co-doped graphene. We performed simultaneous nc-AFM/STM 3D mapping of the B and N dopants. Detailed analysis of the tunneling current variation over the two different dopants supported by the theoretical calculations allowed us to attribute the characteristic tunneling current dip over the N-site to the destructive interference effect. On the B-sites, this effect is completely missing. This striking difference in the atomic contrast allows reliable chemical identification of N and B dopants in the STM images. The origin of the quantum interference is related to an antibonding character of the wave function localized on the N dopant, which has a characteristic node between the central N atom and its nearest neighbor C atoms.

In addition, we analyzed local chemical properties of the B- and N-sites. We found distinct interaction of the probe and the N,B dopants and graphene, which is mainly caused by the local electrostatic interaction due to charge transfer from/to the dopant, respectively. The presence of the weak electrostatic force can play a significant role in graphene functionalization using polar molecules.

We believe that our methodology for B- or N doping and BN co-doping of the graphene introduced in this thesis might open new perspectives in electronics based on graphene/SiC. By using a suitable masking technique for the doping process, spatial control over the dopant distribution can be achieved. A nanoscopic p-n junction device consisting of only single B and N dopants in graphene could be

in principle manufactured. Also the substitutional dopants may play a role of reactive sites for the graphene/SiC(0001) functionalization with suitable molecules and even be exploited in catalytic applications.

Bibliography

[1] A. H. Castro Neto, F. Guinea, N. M. R. Peres, K. S. Novoselov, and A. K. Geim. The electronic properties of graphene. *Rev. Mod. Phys.*, 81:109–162, 2009.

[2] K. S. Novoselov, A. K. Geim, S. V. Morozov, D. Jiang, M. I. Katsnelson, I. V. Grigorieva, S. V. Dubonos, and A. A. Firsov. Two-dimensional gas of massless dirac fermions in graphene. *Nature*, 438(7065):197–200, 2005.

[3] P. R. Wallace. The band theory of graphite. *Phys. Rev.*, 71:622–634, 1947.

[4] A. K. Geim and K. S. Novoselov. The rise of graphene. *Nat. Mater.*, 6(3):183–191, 2007.

[5] K. S. Novoselov, A. K. Geim, S. V. Morozov, D. Jiang, Y. Zhang, S. V. Dubonos, I. V. Grigorieva, and A. A. Firsov. Electric field effect in atomically thin carbon films. *Science*, 306(5696):666–669, 2004.

[6] A. K. Geim. Graphene: Status and prospects. *Science*, 324(5934):1530–1534, 2009.

[7] Goki E., Giovanni F., and Manish C. Large-area ultrathin films of reduced graphene oxide as a transparent and flexible electronic material. *Nature Nanotechnology*, 3(5):270–274, May 2008.

[8] Y. Zhang, L. Zhang, and C. Zhou. Review of chemical vapor deposition of graphene and related applications. *Acc. Chem. Res.*, 46(10):2329–2339, 2013.

[9] X. Li, W. Cai, J. An, S. Kim, J. Nah, D. Yang, R. Piner, A. Velamakanni, I. Jung, E. Tutuc, S. K. Banerjee, L. Colombo, and R. S. Ruoff. Large-area synthesis of high-quality and uniform graphene films on copper foils. *Science*, 324(5932):1312–1314, 2009.

[10] J. Hass, W. A. de Heer, and E. H. Conrad. The growth and morphology of epitaxial multilayer graphene. *J. Phys.: Condens. Matter*, 20(32):323202, 2008.

[11] H. Huang, W. Chen, S. Chen, and A. T. S. Wee. Bottom-up growth of epitaxial graphene on 6H-SiC(0001). *ACS Nano*, 2(12):2513–2518, 2008.

[12] C. Riedl, C. Coletti, and U. Starke. Structural and electronic properties of epitaxial graphene on SiC(0001): a review of growth, characterization, transfer doping and hydrogen intercalation. *J. Phys. D: Appl. Phys.*, 43(37):374009, 2010.

[13] H. Matsunami. Technological breakthroughs in growth control of silicon carbide for high power electronic devices. *Japanese Journal of Applied Physics*, 43(10R):6835, 2004.

[14] E. A. Burgemeister, W. von Muench, and E. Pettenpaul. Thermal conductivity and electrical properties of 6H silicon carbide. *Journal of Applied Physics*, 50(9):5790–5794, 1979.

[15] C. Berger, Z. Song, T. Li, X. Li, A. Y. Ogbazghi, R. Feng, Z. Dai, A. N. Marchenkov, E. H. Conrad, P. N. First, and W. A. de Heer. Ultrathin epitaxial graphite: 2D electron gas properties and a route toward graphene-based nanoelectronics. *The Journal of Physical Chemistry B*, 108(52):19912–19916, 2004.

[16] C. Berger, Zh. S., X. Li, X. Wu, N. Brown, C. Naud, D. Mayou, T. Li, J. Hass, A. N. Marchenkov, E. H. Conrad, Ph. N. First, and W. A. de Heer. Electronic confinement and coherence in patterned epitaxial graphene. *Science*, 312:1191–1196, 2006.

[17] Y. Wu, K. A. Jenkins, A. Valdes-Garcia, D. B. Farmer, Y. Zhu, A. A. Bol, C. Dimitrakopoulos, W. Zhu, F. Xia, P. Avouris, and Y.-M. Lin. State-of-the-art graphene high-frequency electronics. *Nano Lett.*, 12(6):3062–3067, 2012.

[18] Y.-M. Lin, A. Valdes-Garcia, S.-J. Han, D. B. Farmer, I. Meric, Y. Sun, Y. Wu, Ch. Dimitrakopoulos, A. Grill, Ph. Avouris, and Keith A. Jenkins. Wafer-scale graphene integrated circuit. *Science*, 332:1294–1297, 2011.

[19] Y.-M. Lin, C. Dimitrakopoulos, K. A. Jenkins, D. B. Farmer, H.-Y. Chiu, A. Grill, and Ph. Avouris. 100-GHz transistors from wafer-scale epitaxial graphene. *Science*, 327(5966):662, 2010.

[20] J. Ristein, S. Mammadov, and Th. Seyller. Origin of doping in quasi-free-standing graphene on silicon carbide. *Phys. Rev. Lett.*, 108:246104–4, 2012.

[21] Hongtao Liu, Yunqi Liu, and Daoben Zhu. Chemical doping of graphene. *J. Mater. Chem.*, 21:3335–3345, 2011.

[22] C.-K. Chang, S. Kataria, C.-C. Kuo, A. Ganguly, B.-Y. Wang, J.-Y. Hwang, K.-J. Huang, W.-H. Yang, S.-B. Wang, C.-H. Chuang, M. Chen, C.-I. Huang, W.-F. Pong, K.-J. Song, S.-J. Chang, J.-H. Guo, Y. Tai, M. Tsujimoto, S. Isoda, C.-W. Chen, L.-C. Chen, and K.-H. Chen. Band gap engineering of chemical vapor deposited graphene by *in Situ* BN doping. *ACS Nano*, 7(2):1333–1341, 2013.

[23] P. P. Shinde and V. Kumar. Direct band gap opening in graphene by BN doping: *Ab Initio* calculations. *Phys. Rev. B*, 84:125401, 2011.

[24] B. Xu, Y. H. Lu, Y. P. Feng, and J. Y. Lin. Density functional theory study of BN-doped graphene superlattice: Role of geometrical shape and size. *J. Appl. Phys.*, 108(7), 2010.

[25] G. Binnig, H. Rohrer, Ch. Gerber, and E. Weibel. Surface studies by scanning tunneling microscopy. *Phys. Rev. Lett.*, 49:57–61, 1982.

[26] G. Binnig, H. Rohrer, Ch. Gerber, and E. Weibel. 7×7 reconstruction on Si(111) resolved in real space. *Phys. Rev. Lett.*, 50:120–123, 1983.

[27] C.J. Chen. *Introduction to Scanning Tunneling Microscopy*. Introduction to Scanning Tunneling Microscopy. OUP Oxford, 2008.

[28] J. Bardeen. Tunnelling from a many-particle point of view. *Phys. Rev. Lett.*, 6:57–59, 1961.

[29] J. Tersoff and D. R. Hamann. Theory and application for the scanning tunneling microscope. *Phys. Rev. Lett.*, 50:1998–2001, 1983.

[30] J. M. Blanco, C. González, P. Jelínek, J. Ortega, F. Flores, and R. Pérez. First-principles simulations of stm images: From tunneling to the contact regime. *Phys. Rev. B*, 70:085405, 2004.

[31] B. Voigtländer. Technical aspects of scanning probe microscopy. In *Scanning Probe Microscopy*, NanoScience and Technology, pages 31–63. Springer Berlin Heidelberg, 2015.

[32] G. Meyer and N. M. Amer. Novel optical approach to atomic force microscopy. *Appl. Phys. Lett*, 53(12):1045–1047, 1988.

[33] F. J. Giessibl. High-speed force sensor for force microscopy and profilometry utilizing a quartz tuning fork. *Appl. Phys. Lett*, 73(26):3956–3958, 1998.

[34] S. Torbrügge, O. Schaff, and J. Rychen. Application of the kolibrisensor® to combined atomic-resolution scanning tunneling microscopy and noncontact atomic-force microscopy imaging. *J. Vac. Sci. Technol B*, 28(3):12–20, 2010.

[35] Y. Martin, C. C. Williams, and H. K. Wickramasinghe. Atomic force microscope–force mapping and profiling on a sub 100 Å scale. *Journal of Applied Physics*, 61(10):4723–4729, 1987.

[36] T. R. Albrecht, P. Grütter, D. Horne, and D. Rugar. Frequency modulation detection using high q cantilevers for enhanced force microscope sensitivity. *Journal of Applied Physics*, 69(2):668–673, 1991.

[37] J. Berger, M. Švec, M. Muller, M. Ledinský, A. Fejfar, P. Jelínek, and Z. Majzik. Characterization of the mechanical properties of qPlus sensors. *Beilstein J. Nanotechnol.*, 4:1–9, 2013.

[38] F. J. Giessibl. Forces and frequency shifts in atomic-resolution dynamic-force microscopy. *Phys. Rev. B*, 56:16010–16015, 1997.

[39] J. E. Sader and S. P. Jarvis. Accurate formulas for interaction force and energy in frequency modulation force spectroscopy. *Appl. Phys. Lett.*, 84(10):1801–1803, 2004.

[40] F. J. Giessibl. A direct method to calculate tip–sample forces from frequency shifts in frequency-modulation atomic force microscopy. *Appl. Phys. Lett*, 78(1):123–125, 2001.

[41] Y. Sugimoto, P. Pou, M. Abe, P. Jelinek, R. Perez, S. Morita, and O. Custance. Chemical identification of individual surface atoms by atomic force microscopy. *Nature*, 446(7131):64–67, 2007.

[42] Leo Gross, Fabian Mohn, Nikolaj Moll, Peter Liljeroth, and Gerhard Meyer. The chemical structure of a molecule resolved by atomic force microscopy. *Science*, 325(5944):1110–1114, 2009.

[43] S. Hüfner. *Photoelectron Spectroscopy: Principles and Applications*. Advanced Texts in Physics. Springer, 2003.

[44] J. Stöhr. *NEXAFS Spectroscopy*. Springer Series in Surface Sciences. Springer, 1992.

[45] K. Heinz. LEED and DLEED as modern tools for quantitative surface structure determination. *Reports on Progress in Physics*, 58(6):637, 1995.

[46] J.P. Lewis, P. Jelínek, J. Ortega, A.A. Demkov, D.G. Trabada, B. Haycock, H. Wang, G. Adams, J.K. Tomfohr, E. Abad, H. Wang, and D.A. Drabold. Advances and applications in the fireball *Ab initio* tight-binding molecular-dynamics formalism. *Phys. Stat. Sol. B*, 248:1989–2007, 2011.

[47] P. Jelinek, H. Wang, J. Lewis, O. F. Sankey, and J. Ortega. Multicenter approach to the exchange-correlation interactions in *Ab Initio* tight-binding methods. *Phys. Rev. B*, 71:235101, 2005.

[48] M.A. Basanta, Y.J. Dappe, P. Jelínek, and J. Ortega. Optimized atomic-like orbitals for first-principles tight-binding molecular dynamics. *Computational Materials Science*, 39(4):759 – 766, 2007.

[49] J.P. Lewis, P. Jelinek, J. Ortega, A.A. Demkov, D.G. Trabada, B. Haycock, H. Wang, G. Adams, J.K. Tomfohr, E. Abad, H. Wang, and D.A. Drabold. Advances and applications in the fireball *Ab Initio* tight-binding molecular-dynamics formalism. *Phys. Stat. Sol. B*, 248:1989–2007, 2011.

[50] M. A. Basanta, Y. J. Dappe, P. Jelínek, and J. Ortega. Optimized atomic-like orbitals for first-principles tight-binding molecular dynamics. *Comput. Mater. Sci.*, 39(4):759–766, 2007.

[51] G. Kresse and J. Furthmüller. Efficient iterative schemes for *Ab Initio* total-energy calculations using a plane-wave basis set. *Phys. Rev. B*, 54:11169–11186, 1996.

[52] D. Vanderbilt. Soft self-consistent pseudopotentials in a generalized eigenvalue formalism. *Phys. Rev. B*, 41:7892–7895, 1990.

[53] J. M. Blanco, F. Flores, and R. Pérez. STM-theory: Image potential, chemistry and surface relaxation. *Progress in Surf. Sci.*, 81(10–12):403 – 443, 2006.

[54] Z. Majzik, M. Setvín, A. Bettac, A. Feltz, V. Cháb, and P. Jelínek. Simultaneous current, force and dissipation measurements on the Si(111) 7x7 surface with an optimized qplus AFM/STM technique. *Beilstein J. Nanotechnol.*, 3:249–259, 2012.

[55] J. P. Ibe, P. P. Bey, S. L. Brandow, R. A. Brizzolara, N. A. Burnham, D. P. DiLella, K. P. Lee, C. R. K. Marrian, and R. J. Colton. On the electrochemical etching of tips for scanning tunneling microscopy. *J. Vac. Sci. Technol. A*, 8(4):3570–3575, 1990.

[56] D.V. Badami. X-Ray studies of graphite formed by decomposing silicon carbide. *Carbon*, 3(1):53 – 57, 1965.

[57] A.J. Van Bommel, J.E. Crombeen, and A. Van Tooren. LEED and Auger electron observations of the SiC(0001) surface. *Surf. Sci.*, 48(2):463 – 472, 1975.

[58] F. Varchon, R. Feng, J. Hass, X. Li, B. Ngoc Nguyen, C. Naud, P. Mallet, J.-Y. Veuillen, C. Berger, E. H. Conrad, and L. Magaud. Electronic structure of epitaxial graphene layers on SiC: Effect of the substrate. *Phys. Rev. Lett.*, 99:126805, 2007.

[59] U. Starke. Atomic structure of hexagonal SiC surfaces. *physica status solidi (b)*, 202(1):475–499, 1997.

[60] M. Telychko, J. Berger, Z. Majzik, P. Jelínek, and M. Švec. Graphene on SiC(0001) inspected by dynamic atomic force microscopy at room temperature. *Beilstein J. Nanotechnol.*, 6:901–906, 2015.

[61] J. Schardt, J. Bernhardt, U. Starke, and K. Heinz. Atomic structure of hexagonal 6H– and 3C–SiC surfaces. *Surface Review and Letters*, 05(01):181–186, 1998.

[62] H. Raza. *Graphene nanoelectronics: Metrology, synthesis, properties and applications*. Springer Science & Business Media, 2012.

[63] P. Martensson, F. Owman, and L. I. Johansson. Morphology, atomic and electronic structure of 6H-SiC(0001) surfaces. *physica status solidi (b)*, 202(1):501–528, 1997.

[64] R. Kaplan. Surface structure and composition of β - and 6H-SiC. *Surf. Sci.*, 215(1):111 – 134, 1989.

[65] U. Starke, J. Schardt, J. Bernhardt, M. Franke, K. Reuter, H. Wedler, K. Heinz, J. Furthmüller, P. Käckell, and F. Bechstedt. Novel reconstruction mechanism for dangling-bond minimization: Combined method surface structure determination of SiC(111)- (3×3). *Phys. Rev. Lett.*, 80:758–761, 1998.

[66] K. Heinz, J. Bernhardt, J. Schardt, and U. Starke. Functional surface reconstructions of hexagonal SiC. *Journal of Physics: Condensed Matter*, 16(17):1705, 2004.

[67] L. Li and I.S.T. Tsong. Atomic structures of 6H-SiC (0001) and $(000\bar{1})$ surfaces. *Surf. Sci.*, 351(1–3):141 – 148, 1996.

[68] V. van Elsbergen, T.U. Kampen, and W. Mönch. Surface analysis of 6H-SiC. *Surf. Sci.*, 365(2):443 – 452, 1996.

[69] S. Nakanishi, H. Tokutaka, K. Nishimori, S. Kishida, and N. Ishihara. The difference between 6H-SiC (0001) and (0001) faces observed by aes, leed and esca. *Appl. Surf. Sci.*, 41:44 – 48, 1990.

[70] U. Starke, Ch. Bram, P.-R. Steiner, W. Hartner, L. Hammer, K. Heinz, and K. Müller. The (0001)-surface of 6H-SiC: morphology, composition and structure. *Appl. Surf. Sci.*, 89(2):175 – 185, 1995.

[71] U. Starke, J. Schardt, J. Bernhardt, M. Franke, and K. Heinz. Stacking transformation from hexagonal to cubic SiC induced by surface reconstruction: A seed for heterostructure growth. *Phys. Rev. Lett.*, 82:2107–2110, 1999.

[72] J. E. Northrup and J. Neugebauer. Theory of the adatom-induced reconstruction of the SiC(0001) $\sqrt{3} \times \sqrt{3}$. *Phys. Rev. B*, 52:17001–17004, 1995.

[73] F. Owman and P. Mårtensson. The SiC(0001) $6\sqrt{3} \times 6\sqrt{3}$ reconstruction studied with {STM} and {LEED}. *Surf. Sci.*, 369(1–3):126 – 136, 1996.

[74] C. Riedl, U. Starke, J. Bernhardt, M. Franke, and K. Heinz. Structural properties of the graphene-SiC(0001) interface as a key for the preparation of homogeneous large-terrace graphene surfaces. *Phys. Rev. B*, 76:245406, 2007.

[75] R. M. Tromp and J. B. Hannon. Thermodynamics and kinetics of graphene growth on SiC(0001). *Phys. Rev. Lett.*, 102:106104, 2009.

[76] J. B. Hannon and R. M. Tromp. Pit formation during graphene synthesis on SiC(0001): *In situ* electron microscopy. *Phys. Rev. B*, 77:241404, 2008.

[77] S. Kim, J. Ihm, H. J. Choi, and Y.-W. Son. Origin of anomalous electronic structures of epitaxial graphene on silicon carbide. *Phys. Rev. Lett.*, 100:176802–176804, 2008.

[78] P. Merino, M. Švec, J. I. Martínez, P. Mutombo, C. Gonzalez, J. A. Martín-Gago, P. L. de Andres, and P. Jelinek. Ortho and para hydrogen dimers on G/SiC(0001): Combined STM and DFT study. *Langmuir*, 31(1):233–239, 2015.

[79] K. V. Emtsev, F. Speck, Th. Seyller, L. Ley, and J. D. Riley. Interaction, growth, and ordering of epitaxial graphene on SiC(0001) surfaces: A comparative photoelectron spectroscopy study. *Phys. Rev. B*, 77:155303, 2008.

[80] C. Riedl, C. Coletti, T. Iwasaki, A. A. Zakharov, and U. Starke. Quasi-free-standing epitaxial graphene on SiC obtained by hydrogen intercalation. *Phys. Rev. Lett.*, 103:246804, 2009.

[81] J. Sforzini, L. Nemec, T. Denig, B. Stadtmüller, T.-L. Lee, C. Kumpf, S. Soubatch, U. Starke, P. Rinke, V. Blum, F. C. Bocquet, and F. S. Tautz. Approaching truly freestanding graphene: The structure of hydrogen-intercalated graphene on 6H-SiC(0001). *Phys. Rev. Lett.*, 114:106804, 2015.

[82] M. S. Nevius, M. Conrad, F. Wang, A. Celis, M. N. Nair, A. Taleb-Ibrahimi, A. Tejeda, and E. H. Conrad. Semiconducting graphene from highly ordered substrate interactions. *Phys. Rev. Lett.*, 115:136802, 2015.

[83] W. Chen, H. Xu, L. Liu, X. Gao, D. Qi, G. Peng, S. C. Tan, Y. Feng, K. P. L., and A. T. S. Wee. Atomic structure of the 6H–SiC(0001) nanomesh. *Surf. Sci.*, 596(1–3):176 – 186, 2005.

[84] U. Starke, J. Schardt, and M. Franke. Morphology, bond saturation and reconstruction of hexagonal SiC surfaces. *Applied Physics A*, 65(6):587–596, 1997.

[85] G. M. Rutter, N. P. Guisinger, J. N. Crain, E. A. A. Jarvis, M. D. Stiles, T. Li, P. N. First, and J. A. Stroscio. Imaging the interface of epitaxial graphene with silicon carbide *via* scanning tunneling microscopy. *Phys. Rev. B*, 76:235416, 2007.

[86] T. Ohta, A. Bostwick, J. L. McChesney, T. Seyller, K. Horn, and E. Rotenberg. Interlayer interaction and electronic screening in multilayer graphene investigated with angle-resolved photoemission spectroscopy. *Phys. Rev. Lett.*, 98:206802, 2007.

[87] Wataru Norimatsu and Michiko Kusunoki. Structural features of epitaxial graphene on SiC(0001) surfaces. *Journal of Physics D: Applied Physics*, 47(9):094017, 2014.

[88] C. Held, T. Seyller, and R. Bennewitz. Quantitative multichannel NC-AFM data analysis of graphene growth on SiC(0001). *Beilstein J. Nanotechnol.*, 3:179–185, 2012.

[89] T. Filleter and R. Bennewitz. Structural and frictional properties of graphene films on SiC(0001) studied by atomic force microscopy. *Phys. Rev. B*, 81:155412, 2010.

[90] D. S. Wastl, Alfred J. Weymouth, and Franz J. Giessibl. Atomically resolved graphitic surfaces in air by atomic force microscopy. *ACS Nano*, 8(5):5233–5239, 2014.

[91] G. M. Rutter, J. N. Crain, N. P. Guisinger, T. Li, P. N. First, and J. A. Stroscio. Scattering and interference in epitaxial graphene. *Science*, 317(5835):219–222, 2007.

[92] L. B. Biedermann, M. L. Bolen, M. A. Capano, D. Zemlyanov, and R. G. Reifenberger. Insights into few-layer epitaxial graphene growth on 4H-SiC(000$\bar{1}$) substrates from STM studies. *Phys. Rev. B*, 79:125411, 2009.

[93] P. Mallet, F. Varchon, C. Naud, L. Magaud, C. Berger, and J.-Y. Veuillen. Electron states of mono- and bilayer graphene on SiC probed by scanning-tunneling microscopy. *Phys. Rev. B*, 76:041403, 2007.

[94] P. Lauffer, K. V. Emtsev, R. Graupner, Th. Seyller, L. Ley, S. A. Reshanov, and H. B. Weber. Atomic and electronic structure of few-layer graphene on SiC(0001) studied with scanning tunneling microscopy and spectroscopy. *Phys. Rev. B*, 77:155426, 2008.

[95] L. Nemec, V. Blum, P. Rinke, and M. Scheffler. Thermodynamic equilibrium conditions of graphene films on SiC. *Phys. Rev. Lett.*, 111:065502, 2013.

[96] C. Virojanadara, M. Syväjarvi, R. Yakimova, L. I. Johansson, A. A. Zakharov, and T. Balasubramanian. Homogeneous large-area graphene layer growth on 6*H*-SiC(0001). *Phys. Rev. B*, 78:245403, 2008.

[97] K. V. Emtsev, A. Bostwick, K. Horn, J. Jobst, G. L. Kellogg, L. Ley, J. L. McChesney, T. Ohta, S. A. Reshanov, J. Röhrl, E. Rotenberg, A. K. Schmid, D. Waldmann, H. B. Weber, and T. Seyller. Towards wafer-size graphene layers by atmospheric pressure graphitization of silicon carbide. *Nature Materials*, 8:203–207, 2009.

[98] T. Ohta, N. C. Bartelt, S. Nie, K. Thürmer, and G. L. Kellogg. Role of carbon surface diffusion on the growth of epitaxial graphene on SiC. *Phys. Rev. B*, 81:121411, 2010.

[99] M. Nonnenmacher, M. P. O'Boyle, and H. K. Wickramasinghe. Kelvin probe force microscopy. *Appl. Phys. Lett.*, 58:2921–3, 1991.

[100] D. Stradi, S. Barja, C. Diaz, M. Garnica, B. Borca, J. J. Hinarejos, D. Sanchez-Portal, M. Alcami, A. Arnau, A. L. Vazquez de Parga, R. Miranda, and F. Martin. Role of dispersion forces in the structure of graphene monolayers on Ru surfaces. *Phys. Rev. Lett.*, 106:186102–4, 2011.

[101] W. Moritz, B. Wang, M.-L. Bocquet, T. Brugger, T. Greber, J. Wintterlin, and S. Gunther. Structure determination of the coincidence phase of graphene on Ru(0001). *Phys. Rev. Lett.*, 104:136102–4, 2010.

[102] E. N. Voloshina, E. Fertitta, A. Garhofer, F. Mittendorfer, M. Fonin, A. Thissen, and Yu. S. Dedkov. Electronic structure and imaging contrast of graphene moiré on metals. *Scientific Reports*, 3:1072, 2013.

[103] M. Telychko, P. Mutombo, M. Ondráček, P. Hapala, F. C. Bocquet, J. Kolorenč, M. Vondráček, P. Jelínek, and M. Švec. Achieving high-quality

single-atom nitrogen doping of graphene/SiC(0001) by ion implantation and subsequent thermal stabilization. *ACS Nano*, 8(7):7318–7324, 2014.

[104] M. Telychko, P. Mutombo, P. Merino, P. Hapala, M. Ondráček, F. C. Bocquet, J. Sforzini, O. Stetsovych, M. Vondráček, P. Jelínek, and M. Švec. Electronic and chemical properties of donor, acceptor centers in graphene. *ACS Nano*, 9(9):9180–9187, 2015.

[105] J. Sforzini, M. Telychko, O. Krejčí, M. Vondráček, M. Švec, F. C. Bocquet, and F. S. Tautz. Transformation of metallic boron into substitutional dopants in graphene on 6*H*-SiC(0001). *Phys. Rev. B*, 93:041302, 2016.

[106] S. Kopylov, A. Tzalenchuk, S. Kubatkin, and V. I. Fal'ko. Charge transfer between epitaxial graphene and silicon carbide. *Appl. Phys. Lett.*, 97(11):112109, 2010.

[107] Y. Zhang, V. W. Brar, F. Wang, C. Girit, Y. Yayon, M. Panlasigui, A. Zettl, and M. F. Crommie. Giant phonon-induced conductance in scanning tunnelling spectroscopy of gate-tunable graphene. *Nat. Phys.*, 4:627, 2008.

[108] F. Varchon, P. Mallet, L. Magaud, and J.-Y. Veuillen. Rotational disorder in few-layer graphene films on 6H-SiC(000$\bar{1}$): A scanning tunneling microscopy study. *Phys. Rev. B*, 77:165415, 2008.

[109] I. Brihuega, P. Mallet, H. González-Herrero, G. Trambly de Laissardière, M. M. Ugeda, L. Magaud, J. M. Gómez-Rodríguez, F. Ynduráin, and J.-Y. Veuillen. Unraveling the intrinsic and robust nature of van Hove singularities in twisted bilayer graphene by scanning tunneling microscopy and theoretical analysis. *Phys. Rev. Lett.*, 109:196802, 2012.

[110] D. Wong, Y. Wang, J. Jung, S. Pezzini, A. M. DaSilva, H.-Z. Tsai, H. S. Jung, R. Khajeh, Y. Kim, J. Lee, S. Kahn, S. Tollabimazraehno, H. Rasool, K. Watanabe, T. Taniguchi, A. Zettl, S. Adam, A. H. MacDonald, and M. F. Crommie. Local spectroscopy of moiré-induced electronic structure in gate-tunable twisted bilayer graphene. *Phys. Rev. B*, 92:155409, 2015.

[111] S. Forti, K. V. Emtsev, C. Coletti, A. A. Zakharov, C. Riedl, and U. Starke. Large-area homogeneous quasifree standing epitaxial graphene on SiC(0001): Electronic and structural characterization. *Phys. Rev. B*, 84:125449, 2011.

[112] Y. Murata, T. Mashoff, M. Takamura, S. Tanabe, H. Hibino, F. Beltram, and S. Heun. Correlation between morphology and transport properties of quasi-free-standing monolayer graphene. *Appl. Phys. Lett*, 105(22):221604, 2014.

[113] E. Pallecchi, F. Lafont, V. Cavaliere, F. Schopfer, D. Mailly, W. Poirier, and A. Ouerghi. High electron mobility in epitaxial graphene on 4H-SiC(0001) *via* post-growth annealing under hydrogen. *Scientific Reports*, 4:4558, 2014.

[114] D. C. Elias, R. R. Nair, T. M. G. Mohiuddin, S. V. , P. Blake, M. P. Halsall, A. C. Ferrari, D. W. Boukhvalov, M. I. Katsnelson, A. K. Geim, and K. S. Novoselov. Control of graphene's properties by reversible hydrogenation: Evidence for graphane. *Science*, 323(5914):610–613, 2009.

[115] R. R. Nair, W. Ren, R. Jalil, I. Riaz, V. G. Kravets, L. Britnell, P. Blake, F. Schedin, A. S. Mayorov, S. Yuan, M. I. Katsnelson, H.-M. Cheng, W. Strupinski, L. G. Bulusheva, A. V. Okotrub, I. V. Grigorieva, A. N. Grigorenko, K. S. Novoselov, and A. K. Geim. Fluorographene: A two-dimensional counterpart of teflon. *Small*, 6(24):2877–2884, 2010.

[116] S. Oida, F. R. McFeely, J. B. Hannon, R. M. Tromp, M. Copel, Z. Chen, Y. Sun, D. B. Farmer, and J. Yurkas. Decoupling graphene from SiC(0001) *via* oxidation. *Phys. Rev. B*, 82:041411, 2010.

[117] C. Virojanadara, S. Watcharinyanon, A. A. Zakharov, and L. I. Johansson. Epitaxial graphene on 6H-SiC and Li intercalation. *Phys. Rev. B*, 82:205402, 2010.

[118] I. Deretzis and A. La Magna. Role of covalent and metallic intercalation on the electronic properties of epitaxial graphene on SiC(0001). *Phys. Rev. B*, 84:235426, 2011.

[119] B. Premlal, M. Cranney, F. Vonau, D. Aubel, D. Casterman, M. M. De Souza, and L. Simon. Surface intercalation of gold underneath a graphene monolayer on SiC(0001) studied by scanning tunneling microscopy and spectroscopy. *Appl. Phys. Lett*, 94(26), 2009.

[120] I. Gierz, T. Suzuki, R. Thomas Weitz, D. S. Lee, B. Krauss, C. Riedl, U. Starke, H. Höchst, J. H. Smet, C. R. Ast, and K. Kern. Electronic decoupling of an epitaxial graphene monolayer by gold intercalation. *Phys. Rev. B*, 81:235408, 2010.

[121] A. L. Walter, K.-J. Jeon, A. Bostwick, F. Speck, M. Ostler, T. Seyller, L. Moreschini, Y. Su Kim, Y. J. Chang, K. Horn, and E. Rotenberg. Highly p-doped epitaxial graphene obtained by fluorine intercalation. *Appl. Phys. Lett*, 98(18), 2011.

[122] S. L. Wong, H. Huang, Y. Wang, L. Cao, D. Qi, I. Santoso, W. Chen, and A. T. S. Wee. Quasi-free-standing epitaxial graphene on SiC(0001) by

fluorine intercalation from a molecular source. *ACS Nano*, 5(9):7662–7668, 2011.

[123] K. V. Emtsev, A. A. Zakharov, C. Coletti, S. Forti, and U. Starke. Ambipolar doping in quasifree epitaxial graphene on SiC(0001) controlled by Ge intercalation. *Phys. Rev. B*, 84:125423, 2011.

[124] I. Gierz, C. Riedl, U. Starke, C. R. Ast, and K. Kern. Atomic hole doping of graphene. *Nano Lett.*, 8(12):4603–4607, 2008.

[125] A. Tadich, M. T. Edmonds, L. Ley, F. Fromm, Y. Smets, Z. Mazej, J. Riley, C. I. Pakes, Th. Seyller, and M. Wanke. Tuning the charge carriers in epitaxial graphene on SiC(0001) from electron to hole *via* molecular doping with C60F48. *Appl. Phys. Lett*, 102(24), 2013.

[126] C. Coletti, C. Riedl, D. S. Lee, B. Krauss, L. Patthey, K. von Klitzing, J. H. Smet, and U. Starke. Charge neutrality and band-gap tuning of epitaxial graphene on SiC by molecular doping. *Phys. Rev. B*, 81:235401, 2010.

[127] T. Eelbo, M. Waśniowska, P. Thakur, M. Gyamfi, B. Sachs, T. O. Wehling, S. Forti, U. Starke, C. Tieg, A. I. Lichtenstein, and R. Wiesendanger. Adatoms and clusters of 3*d* transition metals on graphene: Electronic and magnetic configurations. *Phys. Rev. Lett.*, 110:136804, 2013.

[128] T. Eelbo, M. Waśniowska, M. Gyamfi, S. Forti, U. Starke, and R. Wiesendanger. Influence of the degree of decoupling of graphene on the properties of transition metal adatoms. *Phys. Rev. B*, 87:205443, 2013.

[129] S. J. Sung, J. W. Yang, P. R. Lee, J. G. Kim, M. T. Ryu, H. M. Park, G. Lee, C. C. Hwang, Kwang. S. Kim, J. S. Kim, and J. W. Chung. Spin-induced band modifications of graphene through intercalation of magnetic iron atoms. *Nanoscale*, 6:3824–3829, 2014.

[130] R. Decker, J. Brede, N. Atodiresei, V. Caciuc, S. Blügel, and R. Wiesendanger. Atomic-scale magnetism of cobalt-intercalated graphene. *Phys. Rev. B*, 87:041403, 2013.

[131] B. M. Ludbrook, G. Levy, P. Nigge, M. Zonno, M. Schneider, D. J. Dvorak, C. N. Veenstra, S. Zhdanovich, D. Wong, P. Dosanjh, C. Straßer, A. Stöhr, S. Forti, C. R. Ast, U. Starke, and A. Damascelli. Evidence for superconductivity in Li-decorated monolayer graphene. *Proceedings of the National Academy of Sciences*, 112(38):11795–11799, 2015.

[132] G. Profeta, M. Calandra, and F. Mauri. Phonon-mediated superconductivity in graphene by lithium deposition. *Nat. Phys.*, 8:131–134, 2012.

[133] Y.-F. Lu, S.-T. Lo, J.-C. Lin, W. Zhang, J.-Y. Lu, F.-H. Liu, C.-M. Tseng, Y.-H. Lee, C.-T. Liang, and L.-J. Li. Nitrogen-doped graphene sheets grown by chemical vapor deposition: Synthesis and influence of nitrogen impurities on carrier transport. *ACS Nano*, 7(8):6522–6532, 2013.

[134] D. Wei, Y. Liu, Y. Wang, H. Zhang, L. Huang, and G. Yu. Synthesis of n-doped graphene by chemical vapor deposition and its electrical properties. *Nano Lett.*, 9(5):1752–1758, 2009.

[135] L. Zhao, R. He, K. T. Rim, T. Schiros, K. S. Kim, H. Zhou, C. Gutiérrez, S. P. Chockalingam, C. J. Arguello, L. Pálová, D. Nordlund, M. S. Hybertsen, D. R. Reichman, T. F. Heinz, P. Kim, A. Pinczuk, G. W. Flynn, and A. N. Pasupathy. Visualizing individual nitrogen dopants in monolayer graphene. *Science*, 333:999–1003, 2011.

[136] L. Zhao, M. Levendorf, S. Goncher, T. Schiros, L. Pálová, A. Zabet-Khosousi, K. T. Rim, C. Gutiérrez, D. Nordlund, C. Jaye, M. Hybertsen, D. Reichman, G. W. Flynn, J. Park, and A. N. Pasupathy. Local atomic and electronic structure of boron chemical doping in monolayer graphene. *Nano Lett.*, 13(10):4659–4665, 2013.

[137] J. Gebhardt, R. J. Koch, W. Zhao, O. Höfert, K. Gotterbarm, S. Mammadov, C. Papp, A. Görling, H.-P. Steinrück, and Th. Seyller. Growth and electronic structure of boron-doped graphene. *Phys. Rev. B*, 87:155437, 2013.

[138] G. Bepete, D. Voiry, M. Chhowalla, Z. Chiguvare, and N. J. Coville. Incorporation of small BN domains in graphene during CVD using methane, boric acid and nitrogen gas. *Nanoscale*, 5:6552–6557, 2013.

[139] E. Velez-Fort, C. Mathieu, E. Pallecchi, M. Pigneur, M. G. Silly, R. Belkhou, M. Marangolo, A. Shukla, F. Sirotti, and A. Ouerghi. Epitaxial graphene on 4H-SiC(0001) grown under nitrogen flux: Evidence of low nitrogen doping and high charge transfer. *ACS Nano*, 6(12):10893–10900, 2012.

[140] F. Joucken, Y. Tison, J. Lagoute, J. Dumont, D. Cabosart, B. Zheng, V. Repain, C. Chacon, Y. Girard, A. R. Botello-Méndez, S. Rousset, R. Sporken, J.-C. Charlier, and L. Henrard. Localized state and charge transfer in nitrogen-doped graphene. *Phys. Rev. B*, 85:161408, 2012.

[141] U. Bangert, W. Pierce, D. M. Kepaptsoglou, Q. Ramasse, R. Zan, M. H. Gass, J. A. Van den Berg, C. B. Boothroyd, J. Amani, and H. Hofsäss.

Ion implantation of graphene – Toward IC compatible technologies. *Nano Lett.*, 13(10):4902–4907, 2013.

[142] Y. Tison, J. Lagoute, V. Repain, C. Chacon, Y. Girard, S. Rousset, F. Joucken, D. Sharma, L. Henrard, H. Amara, A. Ghedjatti, and F. Ducastelle. Electronic interaction between nitrogen atoms in doped graphene. *ACS Nano*, 9(1):670–678, 2015.

[143] K. Kim, S. Yang, Y. Park, M. Lee, B. Kim, and H. Lee. Annealing effects after nitrogen ion casting on monolayer and multilayer graphene. *J. Phys. Chem. C*, 117(5):2129–2134, 2013.

[144] P. Willke, J. A. Amani, S. Thakur, S. Weikert, T. Druga, K. Maiti, H. Hofsäss, and M. Wenderoth. Short-range ordering of ion-implanted nitrogen atoms in SiC-graphene. *Appl. Phys. Lett.*, 105(11), 2014.

[145] P. Willke, J. A. Amani, A. Sinterhauf, S. Thakur, T. Kotzott, T. Druga, S. Weikert, K. Maiti, H. Hofsäss, and M. Wenderoth. Doping of graphene by low-energy ion beam implantation: Structural, electronic, and transport properties. *Nano Lett.*, 15(8):5110–5115, 2015.

[146] J. Sforzini, P. Hapala, M. Franke, G. van Straaten, A. Stöhr, S. Link, S. Soubatch, P. Jelínek, T.-L. Lee, U. Starke, M. Švec, F. C. Bocquet, and F. S. Tautz. Structural and electronic properties of nitrogen-doped graphene. *Phys. Rev. Lett.*, 116:126805, 2016.

[147] A. Zabet-Khosousi, L. Zhao, L. Pálová, M. S. Hybertsen, D. R. Reichman, A. N. Pasupathy, and G. W. Flynn. Segregation of sublattice domains in nitrogen-doped graphene. *J. Am. Chem. Soc.*, 136(4):1391–1397, 2014.

[148] F. Joucken, Y. Tison, P. Le Fèvre, A. Tejeda, A. Taleb-Ibrahimi, E. Conrad, V. Repain, C. Chacon, A. Bellec, Y. Girard, S. Rousset, J. Ghijsen, R. Sporken, H. Amara, F. Ducastelle, and J. Lagoute. Charge transfer and electronic doping in nitrogen-doped graphene. *Scientific Reports*, 5:14564, 2015.

[149] T. Schiros, D. Nordlund, L. Pálová, D. Prezzi, L. Zhao, K. S. Kim, U. Wurstbauer, C. Gutiérrez, D. Delongchamp, C. Jaye, D. Fischer, H. Ogasawara, L. G. M. Pettersson, D. R. Reichman, P. Kim, M. S. Hybertsen, and A. N. Pasupathy. Connecting dopant bond type with electronic structure in N-doped graphene. *Nano Lett.*, 12(8):4025–4031, 2012.

[150] D. Usachov, O. Vilkov, A. Grüneis, D. Haberer, A. Fedorov, V. K. Adamchuk, A. B. Preobrajenski, P. Dudin, A. Barinov, M. Oehzelt, C. Laubschat,

and D. V. Vyalikh. Nitrogen-doped graphene: Efficient growth, structure, and electronic properties. *Nano Lett.*, 11(12):5401–5407, 2011.

[151] Y.-C. Lin, P.-Y. Teng, C.-H. Yeh, M. Koshino, P.-W. Chiu, and K. Suenaga. Structural and chemical dynamics of pyridinic-nitrogen defects in graphene. *Nano Lett.*, 15(11):7408–7413, 2015.

[152] W. Zhao, O. Höfert, K. Gotterbarm, J.F. Zhu, C. Papp, and H.-P. Steinrück. Production of nitrogen-doped graphene by low-energy nitrogen implantation. *J. Phys. Chem. C*, 116(8):5062–5066, 2012.

[153] W. E. Moddeman, A. R. Burke, W. C. Bowling, and D. S. Foose. Surface oxides of boron and $B_{12}O_2$ as determined by XPS. *Surface and Interface Analysis*, 14(5):224–232, 1989.

[154] L. Chen, T. Goto, T. Hirai, and T. Amano. State of boron in chemical vapour-deposited SiC-B composite powders. *Journal of Materials Science Letters*, 9(9):997–999, 1990.

[155] S. Goler, C. Coletti, V. Piazza, P. Pingue, F. Colangelo, V. Pellegrini, K. V. Emtsev, S. Forti, U. Starke, F. Beltram, and S. Heun. Revealing the atomic structure of the buffer layer between SiC(0001) and epitaxial graphene. *Carbon*, 51:249 – 254, 2013.

[156] W. Wan, Li H, H. Huang, S. L. Wong, L. L., Y. Gao, and A. T. S. Wee. Incorporating isolated molybdenum (Mo) atoms into bilayer epitaxial graphene on 4H-SiC(0001). *ACS Nano*, 8(1):970–976, 2014.

[157] S. M. Binz, M. Hupalo, Xiaojie Liu, C. Z. Wang, Wen-Cai Lu, P. A. Thiel, K. M. Ho, E. H. Conrad, and M. C. Tringides. High island densities and long range repulsive interactions: Fe on epitaxial graphene. *Phys. Rev. Lett.*, 109:026103, 2012.

[158] M. Hupalo, X. Liu, C.-Z. Wang, W.-C. Lu, Y.-X. Yao, K.-M. Ho, and M. C. Tringides. Metal nanostructure formation on graphene: Weak versus strong bonding. *Advanced Materials*, 23(18):2082–2087, 2011.

[159] X. Liu, C. Z. Wang, M. Hupalo, Y. X. Yao, M. C. Tringides, W. C. Lu, and K. M. Ho. Adsorption and growth morphology of rare-earth metals on graphene studied by *ab initio* calculations and scanning tunneling microscopy. *Phys. Rev. B*, 82:245408, 2010.

[160] A. Yurtsever, Y. Sugimoto, H. Tanaka, M. Abe, S. Morita, M. Ondracek, P. Pou, R. Perez, and P. Jelínek. Force mapping on a partially H-covered

Si(111)-(7x7) surface: Influence of tip and surface reactivity. *Phys. Rev. B*, 87(15):155403, 2013.

[161] Y. Sugimoto, P. Pou, M. Abe, P. Jelinek, R. Perez, S. Morita, and O. Custance. Chemical identification of individual surface atoms by atomic force microscopy. *Nature*, 446(7131):64–67, 2007.

[162] L. Kong, A. Enders, T. S. Rahman, and Peter A. Dowben. Molecular adsorption on graphene. *J. Phys.: Condens. Matter*, 26(44):443001, 2014.

[163] J. Cho, J. Smerdon, L. Gao, Ö. Süzer, J. R. Guest, and N. P. Guisinger. Structural and electronic decoupling of C60 from epitaxial graphene on SiC. *Nano Lett.*, 12(6):3018–3024, 2012.

[164] V. Georgakilas, M. Otyepka, A. B Bourlinos, V. Chandra, N. Kim, K. C. Kemp, P. Hobza, R. Zboril, and K. S. Kim. Functionalization of graphene: Covalent and non-covalent approaches, derivatives and applications. *Chem. Rev.*, 112(11):6156–6214, 2012.

List of Abbreviations

- STM: Scanning Tunneling Microscopy
- AFM: Atomic Force Microscopy
- nc-AFM: Non-contact Atomic Force Microscopy
- STS: Scanning Tunneling Spectroscopy
- LDOS: Local Density of Electronic States
- XPS: X-Ray Photoelectron Spectroscopy
- NEXAFS: Near Edge X-ray Adsorption Spectroscopy
- DFT: Density Functional Theory
- ARPES: Angle Resolved Photoelectron Spectroscopy
- LEED: Low Energy Electron Diffraction
- SiC: Silicon Carbide
- BL: Buffer Layer
- SLG: Single Layer Graphene
- BLG: Bilayer Graphene
- QFMLG: Quasi-Free-Standing Monolayer Graphene
- UHV: Ultra-High Vacuum
- q-$6\sqrt{3}$: quasi-periodic $6\sqrt{3} \times 6\sqrt{3}R30°$ reconstruction
- q-6×6: quasi-periodic 6×6 reconstruction
- q-$5\sqrt{3}$: quasi-periodic $5\sqrt{3} \times \sqrt{3}R30°$ reconstruction

About author

List of publications

1. M. Telychko, P. Mutombo, P. Merino, P. Hapala, M. Ondráček, F. C. Bocquet, J. Sforzini, O. Stetsovych, M. Vondráček, P. Jelínek, and M. Švec. *Electronic and chemical properties of donor, acceptor centers in graphene.* ACS Nano, 9(9):9180–9187, 2015.

2. M. Telychko, J. Berger, Z. Majzik, P. Jelínek, and M. Švec. *Graphene on SiC(0001) inspected by dynamic atomic force microscopy at room temperature.* Beilstein Journal of Nanotechnology, 6:901–906, 2015.

3. M. Telyhko, P. Mutombo, M. Ondráček, P. Hapala, F. C. Bocquet, J. Kolorenč, M. Vondráček, P. Jelínek, and M. Švec. *Achieving high-quality single-atom nitrogen doping of graphene/SiC(0001) by ion implantation and subsequent thermal stabilization.* ACS Nano, 8(7):7318–7324, 2014.

4. J. Sforzini, M. Telychko, O. Krejčí, M. Vondráček, M. Švec, F. C. Bocquet, and F. S. Tautz. *Transformation of metallic boron into substitutional dopants in graphene on 6H-SiC(0001).* Physical Review B. 93: 041302, 2016.

5. E. J. Spadafora, J. Berger, P. Mutombo, M. Telychko, M. Švec, Z. Majzik, A. B. McLean, and P. Jelínek. *Identification of surface defects and subsurface dopants in a delta-doped system using simultaneous nc-AFM/STM and DFT.* Journal of Physical Chemistry C, 118 (29): 15744–15753, 2014.

Conference participation

1. ECOSS-2015, 30.08-07.09 2015, Barcelona (Spain).
   Destructive interference towards chemical discrimination of N and B dopant in the B,N co-doped graphene/SiC(0001) (oral presentation).

2. DPG, Berlin (Germany), 15.03-21.03 2015.
   Quantum interference on the doped graphene/SiC systems (oral presentation).

3. INS Summer School "New Frontiers in Scanning Force Microscopy", Madrid (Spain), 14.06-18.06 2014.
   Achieving high quality single atom N-doping of graphene/SiC(0001) by ion implantation and subsequent thermal stabilization (poster presentation).

4. ECOSS-2014, Antalya (Turkey), 31.08-05.09 2014. *Single atom B and N co-doping of graphene/SiC(0001)* (oral presentation).

5. DPG, Dresden (Germany), 30.03-04.04 2014.
   High-quality single atom N-doping of graphene/SiC(0001) by ion implantation (oral presentation).

6. WE-Heraeus-Seminar "Interactions with the Nanoworld: Local Probes with Time, Energy and Force Resolution", Bad Honnef (Germany) 11.11-13.11 2013.
   nc-AFM/STM and DFT study of the B:Si(111)$\sqrt{3} \times \sqrt{3}$ *surface* (poster presentation).